A Novel Electrochemical Technique to Measure Hydrogen Permeability in Polymers

Aerospace Structures and Materials
Tommaso Mazzanti

Delft University of Technology

TU Delft

A Novel Electrochemical Technique to Measure Hydrogen Permeability in Polymers

by

Tommaso Mazzanti

Student Name	Student Number
Tommaso Mazzanti	5849462

Supervising Professor:	Santiago Garcia Espallargas
Daily Supervisor:	Lakshmi Satish Nair
Project Duration:	February, 2024 - November, 2024
Faculty:	Faculty of Aerospace Engineering, Delft

Cover: Airplane and hydrogen tank trailer on the background of airport. Courtesy of H2 View

TU Delft

Acknowledgements

First, I would like to express my gratitude to my promotor, Santiago, for his continuous support and insightful remarks throughout this research. I am also profoundly grateful to my daily supervisor, Lakshmi, whose patience, mentorship, and advice have immensely enriched my experience during this project.
I would also like to acknowledge the entire research group for their willingness to help whenever needed.

Finally, I would like to express my heartfelt appreciation to my family: my mother, Daniela, my father, Alessandro,my uncle, Roberto, and my girlfriend, Letizia, for their constant love and encouragement, not just during these two years, but throughout my life.
To my grandmother, Iolanda, I will forever hold your memory and love in my heart.

Tommaso Mazzanti
Delft, November 2024

Abstract

With increasing research into hydrogen-fueled commercial aviation, polymer-based materials are being explored for use in lightweight liquid hydrogen storage tanks. This thesis investigates the adaptation of the Devanathan-Stachurski (DS) cell, traditionally used for studying hydrogen permeation in metals, as a testing method for polymeric materials. Unlike conventional high-pressure techniques, the DS cell offers a compact, efficient, and safer approach by using electrochemistry to evolve hydrogen in minute quantities. This adaptation has the potential to assess permeability, diffusivity, and solubility of polymer-based materials while avoiding the complications associated with high-pressure hydrogen techniques.

The study begins with an analysis of the traditional DS cell's components and features, in order to identify modifications necessary for testing polymers. Key adaptations include the selection of a palladium coating as a catalyst for hydrogen evolution, oxidation and absorption, and the tuning for current and potential in both detection and charging cells. By refining these parameters, the study establishes a protocol suitable for polymer samples, with emphasis on consistency and reproducibility in permeation measurements.

Hydrogen permeation characteristics were measured across three polymers: polyether ether ketone (PEEK), high-density polyethylene (HDPE), and polypropylene (PP). The results exhibited plausible trends consistent with expected diffusion behaviors reported in the literature. Discrepancies in numerical values between this setup and traditional methods are attributed to the differing driving forces for diffusion.

Two calculation methods were employed to interpret the diffusivity data: the time-lag method, which measures diffusion at steady-state conditions, and the breakthrough time method, which evaluates initial diffusion in unsteady state. While the time-lag method was found to yield more comparable results across samples by mitigating individual sample variability, the breakthrough time method offered valuable insight into the initial material response to hydrogen. An additional approach based on Sethuraman's diffusion model was applied; however, it could not be fitted to all data due to its reliance on ideal boundary condition assumptions. This limitation emphasizes the need for more consistent experimental conditions to fully leverage this method.

The results of hydrogen diffusion and sorption in the three polymers highlighted crystallinity and glass transition temperature (T_g) as the primary factors influencing these processes. These findings point to the critical role of each polymer's molecular structure in defining hydrogen's sorption and diffusion behavior.

Overall, the Devanathan Stachurski cell adaptation for polymers presents a promising, versatile alternative for assessing hydrogen permeation. Future work is recommended to refine the setup and allow for even more consistent and reliable results. This setup's simplicity and adaptability hold significant potential for the pre-screening of polymer candidates for hydrogen storage applications.

Contents

List of Figures

List of Tables

Nomenclature

Abbreviations

Abbreviation	Definition
CE	Counter Electrode
CFRP	Carbon Fiber Reinforced Polymer
CV	Cyclic Voltammetry
DS	Devanathan-Stachurski (cell for electrochemical permeation technique)
DSC	Differential Scanning Calorimetry
EMT	Electrochemical Monitoring Technique
EU	European Union
F	Faraday Constant
FVE	Free Volume Element
FCC	Face-Centered Cubic
FTIR	Fourier Transform Infrared Spectroscopy
HDPE	High Density Polyethylene
HER	Hydrogen Evolution Reaction
HPHP	High-Pressure Hydrogen Permeation
HOR	Hydrogen Oxidation Reaction
LH_2	Liquid Hydrogen
LN_2	Liquid Nitrogen
OCP	Open Circuit Potential
OER	Oxygen Evolution Reaction
ORR	Oxygen Reduction Reaction
PDMS	Polydimethylsiloxane
PEEK	Polyether Ether Ketone
PP	Polypropylene
RE	Reference Electrode
SHE	Standard Hydrogen Electrode
TDA	Thermal Desorption Analysis
TR	Thermally Rearranged
WE	Working Electrode

Symbols

Symbol	Definition	Unit
A	Area exposed to the electrolyte (permeation area)	[cm^2]
b	Hole affinity constant	[-]
c	Concentration of gas in the polymer	[mol/cm^3]
c_D	Concentration in equilibrium free volume sites	[mol/cm^3]
c_H	Concentration in non-equilibrium free volume sites	[mol/cm^3]
c'_H	Hole saturation constant	[-]
D	Diffusion coefficient	[cm^2/s]
Δp	Pressure differential	[Pa]

Symbol	Definition	Unit
E_d	Activation energy for diffusion	[J/mol]
E_p	Apparent activation energy of permeation	[J/mol]
E_s	Heat of solution for gas in the polymer	[J/mol]
F	Faraday constant	[C/mol]
J	Diffusion flux	[mol/(cm^2· s)]
k_D	Proportionality coefficient for Henry's law	[-]
ℓ	Thickness of the sample	[mm]
n	Number of electrons liberated during oxidation	[-]
P	Permeability	[mol/(cm·s)]
p	Pressure	[Pa]
Q	Amount of permeated hydrogen	[mol]
Q_t	Total charge	[C]
R	Universal gas constant	[J/(mol·K)]
S	Solubility constant	[mol/cm^3]
T	Temperature	[K]
T_g	Glass transition temperature	[°C]
θ	Time lag	[s]
χ_C	Degree of crystallinity	[-]
ΔH_m	Enthalpy of fusion of the sample	[J/g]
ΔH_{CC}	Enthalpy of cold crystallization	[J/g]
$\Delta H_m^{100\%}$	Enthalpy of fusion of a fully crystalline sample	[J/g]
ρ	Density of the sample	[g/cm^3]
ρ_a	Density of a fully amorphous sample	[g/cm^3]
ρ_C	Density of a fully crystalline sample	[g/cm^3]

1

Introduction

In 2020, the European Green Deal set an ambitious goal for the EU to achieve climate neutrality by 2050 [83]. This initiative has spurred the aviation industry to explore innovative technologies to reduce emissions. Among the most promising solutions is hydrogen fuel, which has attracted substantial investment from major companies such as Airbus, H2Fly, and Air Liquide, all committed to advancing research in this area [92, 80]. However, while hydrogen propulsion offers considerable potential, several technical challenges must be addressed before the first zero-emission commercial aircraft can be brought to the market.

Hydrogen as a fuel has the potential to become completely climate-neutral. Its specific energy is much higher than that of conventional jet fuels [17]. However, its low density at ambient room temperature necessitates high-pressure storage in the confined spaces of an aircraft. This requirement results in exceptionally heavy tanks and raises safety considerations. An alternative approach is to store hydrogen in its denser liquid phase at cryogenic temperatures and lower pressure [75]. Storing hydrogen at cryogenic temperatures significantly boosts its volumetric energy density—from 2.9 MJ/L at 350 bar and ambient temperature for gaseous hydrogen to 8.5 MJ/L at 2 bar and 20 K for liquid hydrogen (LH_2) [74], allowing for a considerable reduction of the structural mass. Maintaining hydrogen in a liquid state, however, leads to significant thermal management challenges. Effective insulation, robust structural design, and reliable safety measures are essential to manage the extreme temperature differential between the cryogenic fuel and ambient conditions, which can exceed 318 K during flight. The complexity of cryogenic storage demands additional design considerations, such as heat exchangers, safety valves, and gas extraction lines, to ensure safe and efficient operation [7].

Ideal materials for cryogenic tanks should possess high strength, fracture toughness, stiffness, low density, and minimal permeability to LH_2, ensuring containment and structural integrity at low temperatures. Engineers have sought to balance these properties and have proposed 5 possible tank designs. These range from all-metal Type I tanks to composite-wrapped with metal (type II - III) or polymer (type IV) liners and all-composite designs (type V), as shown in Figure 1.1. Except for Type I, all the designs incorporate polymers or polymer-based materials, and Types III, IV, and V show particular promise for aerospace applications [76, 7]. These three tanks all employ polymers to enhance properties such as strength-to-weight ratio, corrosion resistance, and design flexibility. However, polymers also introduce specific challenges due to their susceptibility to hydrogen permeation. As hydrogen boils off in cryogenic conditions, it can escape either through the bulk polymer or at fiber-polymer interfaces in composite tanks, posing risks of fuel loss and safety hazards due to hydrogen's high flammability.

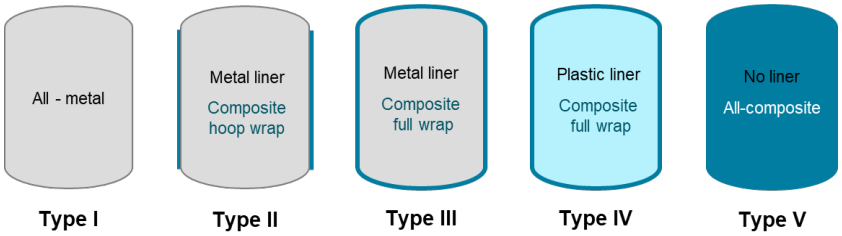

Figure 1.1: Classification of hydrogen pressure vessels [7]

Therefore, understanding hydrogen permeation and interaction in polymers is crucial for the safe and efficient use of polymer-based materials in hydrogen storage, particularly under cryogenic conditions. Unlike metals, which have densely packed atomic structures, polymers consist of long molecular chains in either amorphous or semi-crystalline arrangements, making them inherently more susceptible to gas permeation.

Despite the potential of polymer-based materials in hydrogen storage, very little experimental work has been conducted to understand the physics of hydrogen permeation through these materials. Existing testing methods, such as Thermal Desorption Analysis and High Pressure Hydrogen Permeation Testing, are limited by their complexity and the inherent risks of handling hydrogen gas [28]. Addressing this gap, the aim of this thesis is to explore whether an electrochemical technique, traditionally used for studying hydrogen permeation in metals, could be adapted to test polymer samples.

The main objective of this research was to develop and validate a novel electrochemistry-based permeability testing technique for polymers by adapting the Devanathan-Stachurski (DS) cell, a three-electrode setup widely employed to investigate hydrogen embrittlement in metals [19]. This adapted DS cell uses electrochemistry to monitor the flow of hydrogen through polymer specimens, aiming to provide a compact, rapid, and safe method for assessing hydrogen permeability in polymers. Ultimately, this setup will be used to correlate fundamental physical (e.g., glassy or rubbery state), chemical (structure, crystallinity), and thermodynamic (glass transition temperature, T_g) properties of polymers with their responses to hydrogen permeation. Findings from this work, along with future studies using this method, hold the potential to address key safety and performance considerations for polymer-based materials intended for use in hydrogen-powered aviation.

This chapter will first provide background on the fundamental mechanisms of hydrogen interaction with polymers, including sorption, diffusion, and the factors influencing these processes. Next, the state-of-the-art experimental methods for evaluating hydrogen permeability will be explored. Finally, the proposed adaptation of the Devanathan-Stachurski cell will be discussed, setting the stage for the research scope of this thesis.

1.1. Hydrogen Permeation in Polymers

The permeation mechanism is strongly dependent on the molecular structure of the material. All polymers share a characteristic structure comprising molecular chains and interspersed free volumes [66]. These materials can be categorized into thermoplastics, thermosets, and elastomers based on how their molecular chains are linked. As shown in figure 1.2, thermoplastics are characterized by linear or slightly branched molecular chains bonded together by weaker van der Waals forces or hydrogen bonds. On the other hand, thermosets feature chains that are covalently bonded into a network (cross-linked), creating stronger intermolecular connections than those found in thermoplastics.

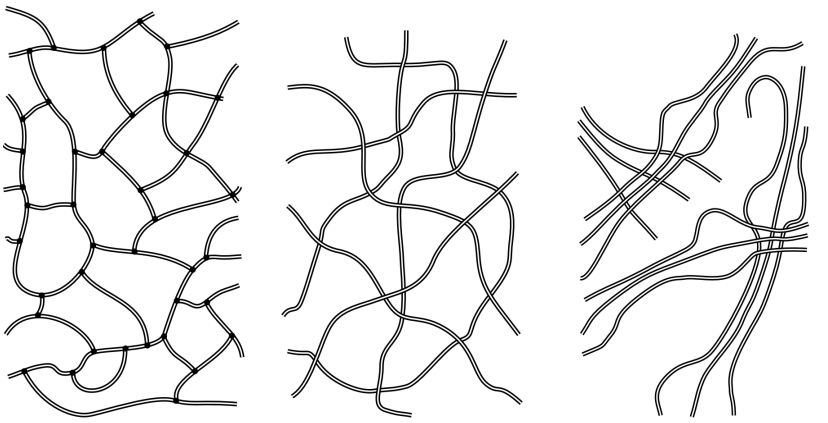

(a) thermoset (b) amorphous thermoplastic (c) semi-crystalline thermoplastic

Figure 1.2: Molecular structures of thermosets and thermoplastics. The space between the entangled chains represent the free volume of the material [71]

Above absolute zero, the polymer chains oscillate, causing free volumes to be constantly created and destroyed. These free volumes can be thought of as pockets in the material through which small permeant molecules can move, driven by the concentration gradient in the bulk material [71, 56].

The driving force for diffusion of the permeant gas through the polymer can be either a pressure (N/m^2), mass concentration (kg/m^3) or molar concentration (mol/m^3) gradient. In all three cases — whether driven by a pressure gradient, mass concentration gradient, or molar concentration gradient — the permeation process remains analogous [85]. The permeant molecules go through the same stages of sorption, diffusion and desorption regardless of the specific gradient driving the permeation . To provide a clearer understanding of the permeation process, in the next paragraphs we will focus on the case where the driving force is a pressure differential. This approach allows for a more intuitive explanation of the permeation mechanism by considering the movement of gas molecules from a region of higher pressure to a region of lower pressure. The mechanism of permeation through a polymer material can be decomposed into five different steps [44],as shown in figure 1.3:

- permeant diffusion to the side corresponding to higher partial pressure (upstream side)
- sorption at the polymer-gas interface on the upstream side (governed by gas solubility)
- diffusion of the gas through the polymer material
- desorption (inverse of the sorption process) of the gas at the polymer surface on the downstream side.
- diffusion of the gas away from the downstream side

The process of gas diffusion through the bulk material is the slowest one, therefore it becomes the rate-determining step in the permeation process.

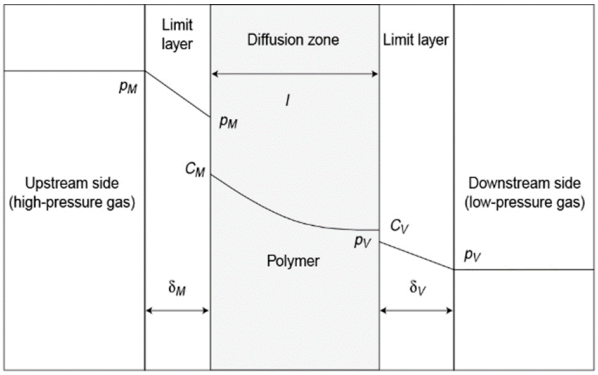

Figure 1.3: The permeation process of a gas through a polymer [79]

1.1.1. Sorption

Various models describe the sorption process. The choice of the suitable model depends on several factors: the type of gas and polymer interacting (including the dimensions of the gas molecules and whether the polymer swells due to gas absorption, as seen in hydrophilic membranes), and the system's temperature (whether it is above or below the critical temperature of the gas and the glass transition temperature of the polymer).

Rubbery Polymers

In rubbery polymers, gas sorption involves the dissolution of gas molecules into the polymer matrix. At a microscopic level, gas molecules penetrate the polymer and occupy the equilibrium free volume present in the polymer matrix. This can be visualized as gas molecules filling the voids between polymer chains, which are relatively mobile and less densely packed compared to glassy polymers. The equilibrium between the molecules in the gas phase and those adsorbed at the polymer surface is established rapidly due to the mobility of the polymer chains [8]. The ideal sorption of gases in rubbery polymers is described by Henry's law. Assuming that the penetrating gas is ideal, and the pressure of the gas is relatively low, the concentration of gas (C) in the polymer is proportional to the pressure (p) of the gas:

$$C = S \cdot p \tag{1.1}$$

The constant S is called solubility. Assuming the gas behaves ideally and is uniformly distributed within the polymer, Henry's law is applicable, especially at lower gas pressures. In this case, solubility is largely independent of temperature and concentration [69], as the polymer–penetrant interactions are minimal, and the gas molecules do not exhibit any significant specific interactions. This ideal sorption behavior is typically observed when "permanent gases" are the penetrants and the pressure is close to atmospheric [85]. Although Henry's law primarily applies to low pressures, linear isotherms for light gases are often observed over a wide range of practical pressures, as shown in figure,1.4.

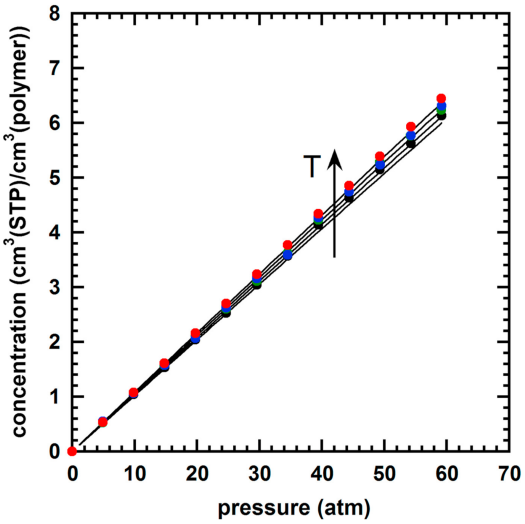

Figure 1.4: H_2 sorption isotherms for PDMS. Filled circles stand for experimental data at different temperatures (all above the T_g of the polymer). [31]

Glassy Polymers

When the temperature of the environment is below the T_g, the polymer chains' mobility is restricted, therefore they cannot all reach their equilibrium state and are frozen in place. Due to the presence of both equilibrium and non-equilibrium (unrelaxed) free volume, the sorption process is more complex and is described by the dual sorption model. According to this model, absorbed gas molecules occupy two sites:

- **Equilibrium free volume sites** where gas molecules dissolve similarly to rubbery polymers. This population of molecules follows Henry's law of sorption. [69]
- **Non-equilibrium free volume sites**, also referred as "holes" where gas molecules are trapped and partially immobilised. When all these sites are completely saturated, a small quantity of molecules may solubilise. This population of molecules follow Langmuir's mode of sorption. [44].

Therefore, the sorption isotherm for glassy polymers is expressed as a combination of Henry's law and the Langmuir isotherm:

$$C = c_D + c_H = k_D p + \frac{c'_H b p}{1 + bp} \tag{1.2}$$

where k_D is the proportionality coefficient for Henry's law (analogous to the solubility constant of rubbery polymers), c'_H is hole saturation constant and b is a hole affinity constant. Figures 1.5 and 1.6 shows an example of theoretical and experimental dual mode sorption curves.rom the curves, it is clear that for hydrogen at low to moderate pressure, the ideal sorption behavior described by Henry's law still provides a very good approximation of the sorption mechanism.

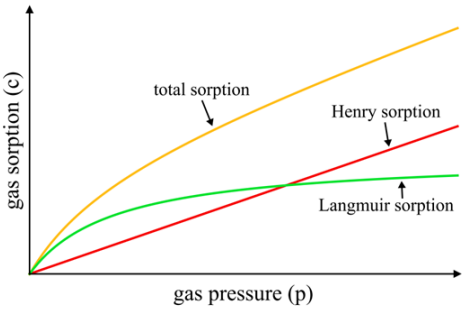

Figure 1.5: An illustration of the two contributions to sorption in glassy polymers. [69]

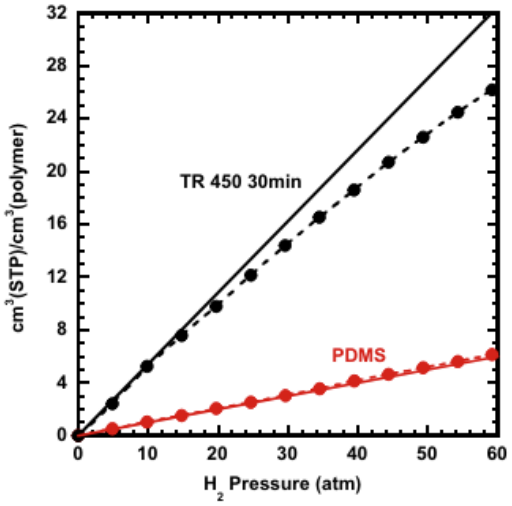

Figure 1.6: Comparison of H2 sorption in a glassy TR 450 30 min (thermally rearranged polyimide sample at 450 °C for 30 minutes) to that of a rubbery PDMS sample at approximately -20 °C. Straight, solid lines are drawn to demonstrate dual-mode curvature for the TR 450 30 min sample and to show the linearity of the H2 sorption isotherm for PDMS. [77]

1.1.2. Diffusion

Diffusion is a fundamental process in the permeation of gases through polymers. It describes the movement of gas molecules from regions of higher concentration to regions of lower concentration within the polymer matrix. This process is critical in determining the overall permeability of the polymer to gases. The diffusion step is often considered the rate-limiting step in the permeation process because it directly impacts the rate at which gas molecules migrate through the polymer.
On a microscopic level, diffusion can be explained using the free volume theory. According to this theory, the movement of molecules within a polymer occurs through jumps between thermally generated nanovoids within the polymer matrix. These diffusing molecules occupy small cavities, known as free volume elements (FVEs) or ”holes,” between polymer chains. Due to the random thermal motions of the polymer chains, these cavities continuously form and disappear. When a sufficiently large nanovoid forms adjacent to a diffusing molecule, the molecule can jump into it, staying there until another suitable thermal motion occurs. The collective free volume in an amorphous polymer, as opposed to the volume occupied by polymer chains, plays a crucial role in determining the diffusivity of gas molecules, which depends on both the size of the gas molecule and the total free volume available for diffusion [21]. This mechanism is shown in figure 1.7 below.

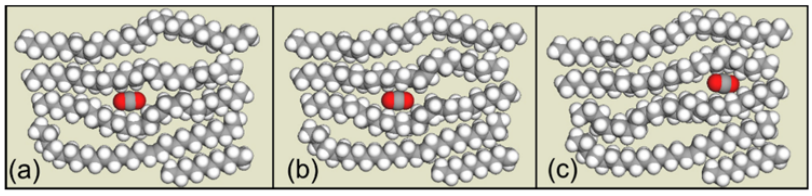

Figure 1.7: Diffusion of gas molecules in amorphous polymers: the molecule occupies a nanocavity (a) until a new one forms adjacent to the diffusing molecule, by means of thermal fluctuations of the polymer matrix (b). When this happens, the molecule can jump to the new nanocavity (c). [69]

Free volume is typically larger in glassy polymers than in rubbery ones due to structural differences above and below the glass transition temperature (T_g). Above T_g , polymers are in a rubbery state with

significant chain mobility and large contributions from hole free volume. Below T_g, polymer chains are "frozen," trapping excess free volume and resulting in a non-equilibrium state (figure 1.8). Over time, glassy polymers undergo densification or aging, gradually reaching equilibrium and reducing excess free volume [21, 32, 39].

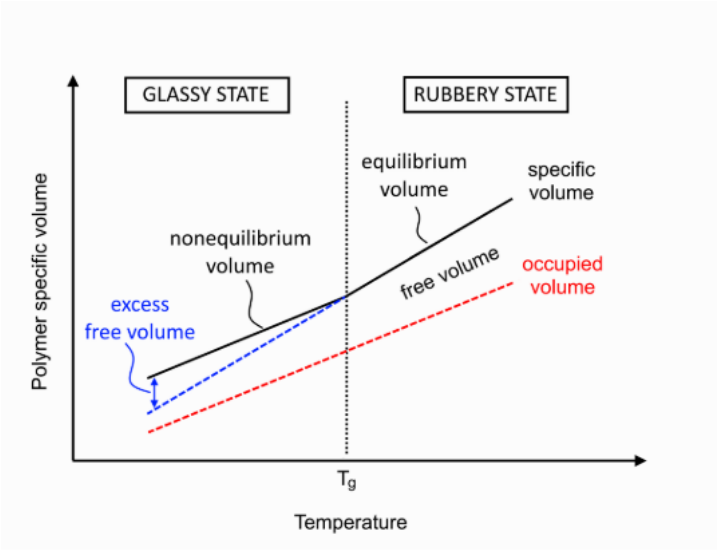

Figure 1.8: The different contributions to a polymer's volume as a function of temperature. [69]

Under the same assumptions described in 1.1.1, the diffusion process in polymers can be described by Fick's laws of diffusion. Fick's first law relates the flux of diffusing species to the concentration gradient:

$$\mathbf{J} = -D\nabla\mathbf{C} \tag{1.3}$$

where **J** is the diffusion flux, D is the diffusivity and $\nabla\mathbf{C}$ is the concentration gradient. According to the first law, the diffusion coefficient is independent of the concentration of the sorbed penetrant [85]. Fick's second law predicts how the concentration of diffusing species changes with time:

$$\frac{\partial C}{\partial t} = D\nabla^2\mathbf{C} \tag{1.4}$$

where $\nabla^2\mathbf{C}$ indicates the concentration distribution in the bulk material. The physical meaning of Fick's laws can be visualized in figure 1.9 below.

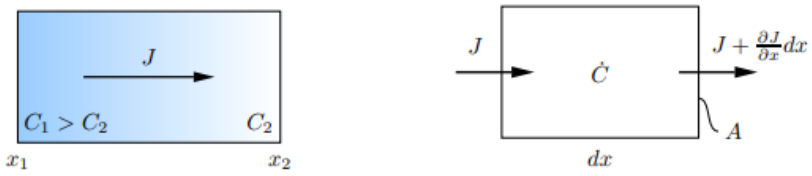

Figure 1.9: Left to right: Fick's first and second law [71].

1.1.3. Permeation

In order to analyze how sorption and diffusion influence permeation, we will apply the previous equations to a case study. During any hydrogen permeability test, H_2 at pressure p_{HPS} is applied on one side of the polymer sample. On the other side, permeated H_2 at pressure $p_{LPS} \ll p_{HPS}$ is detected and then removed. Assuming one-dimensional diffusion through the thickness ℓ of the sample (this happens if $A_{interaction} \gg \ell$), we have the following conditions:

- Initially, the concentration $c(x)$ of H_2 is zero throughout the membrane
- At $t = 0$, the feed side of the sample is exposed to the hydrogen, so that for $t \geq 0$ $c(x = 0) = Sp_{HPS}$ is constant.

These are the boundary conditions:

$$c(x = 0, t < 0) = 0 \qquad c(x = \ell, t < 0) = 0 \tag{1.5}$$

$$c(x = 0, t \geq 0) = Sp_{HPS} \qquad c(x = \ell, t \geq 0) = Sp_{LPS} \simeq 0 \tag{1.6}$$

With these conditions, Fick's laws can be solved for the one-dimensional flux of H_2 through the sample, giving the following equation:

$$J(t) = \frac{DSp_{HPS}}{\ell}\left[1 + 2\sum_{n=1}^{\infty}(-1)^n \exp\left(-\frac{Dn^2\pi^2 t}{\ell^2}\right)\right] \tag{1.7}$$

For $t \to \infty$, stationary transport condition is reached. The concentration gradient becomes linear through the thickness of the polymers, as shown in figure 1.10 and we obtain the following equation for the H_2 flux:

$$J^{stc} = \frac{DS\Delta p}{\ell} \tag{1.8}$$

Permeability is defined as the stationary gas flux normalized by the pressure differential and the thickness of the sample [1]:

$$P = J^{stc}\frac{\ell}{\Delta p} \tag{1.9}$$

therefore:

$$P = S \cdot D \tag{1.10}$$

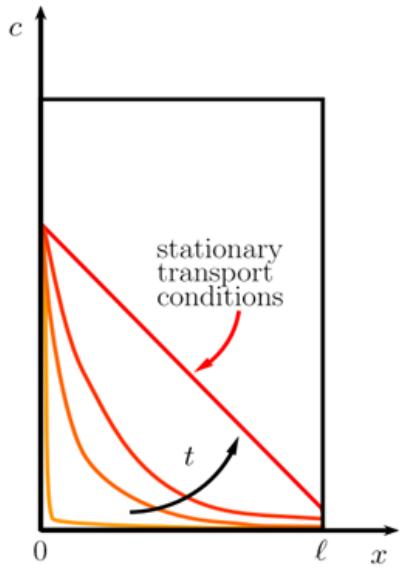

Figure 1.10: A qualitative plot of the permeant concentration throughout the membrane at different times. The color of the curve shifts over increasing time from orange to red.[69]

[1] This definition of permeability is specific to the case where the diffusion is driven by a pressure difference between the two sides of the sample. The expression can be generalized to: $P = J^{stc}\frac{\ell}{\Delta\varphi}$, where $\Delta\varphi$ is the potential difference between the upstream and downstream side. This potential can either be pressure, mass, or molar concentration [85].

Glassy Polymers

The dual sorption model described in 1.1.1 applies to the diffusion and permeation processes as well. Therefore, the flux is now the sum of the two components:

$$J = -D_D \frac{\partial c_D}{\partial x} - D_H \frac{\partial c_H}{\partial x} \tag{1.11}$$

where the letters **D** and **H** refer respectively to the Henry and Langmuir populations of diffusing molecules.

Starting from equation 1.2, it is possible to define two distinct solubility parameters for the two populations:

$$S_D = \frac{c_D}{p_{\text{HPS}}} = k_D \quad \text{and} \quad S_H = \frac{c_H}{p_{\text{HPS}}} = \frac{c'_H b}{1 + b p_{\text{HPS}}} \tag{1.12}$$

and finally, assuming the downstream pressure to be zero, the permeability is defined as follows:

$$P = S_D D_D + S_H D_H = k_D D_D \left(1 + \frac{FK}{1 + b p_{\text{HPS}}}\right) \tag{1.13}$$

where $F = \frac{D_H}{D_D}$ and $K = \frac{c'_H b}{k_D}$ [64].

1.1.4. Influencing Parameters

Temperature

Permeability of hydrogen through both polymers and fiber composites follows an Arrhenius-type relation, where:

$$S = S_0 \exp\left(-\frac{E_s}{RT}\right) \tag{1.14}$$

$$D = D_0 \exp\left(-\frac{E_d}{RT}\right) \tag{1.15}$$

$$P = P_0 \exp\left(-\frac{E_p}{RT}\right) \tag{1.16}$$

S_0, D_0 and P_0 are pre-exponential factors.
E_d is the activation energy of the diffusion process, or the energy that is needed by a permeant molecule to make a diffusional jump between one position and the other in the polymer.
E_s is the heat of solution needed for the dissolution of a permeant mole in the polymer matrix.
E_p is the apparent activation energy of the permeation process and is simply the sum of the two previous terms [27].

Pressure

The relationship between permeability and pressure has been extensively discussed in 1.1.1, 1.1.2 and 1.1.3. To sum up, various studies [44, 66] have shown that up until 20 bars, the permeability remains constant with pressure. Fujiwara et al. [27] have used the high-pressure permeation test setup to evaluate the permeability of H2 until 80 bars. As shown in figures 1.11 and 1.12, the permeability decreases with pressure. This is due to the hydrostatic effect. The polymer chains are compressed, thus the free volume decreases. This means that the diffusion process is hindered, and that is also proven in figure 1.12 which shows the diffusion coefficient decreasing with pressure while the solubility remains constant.

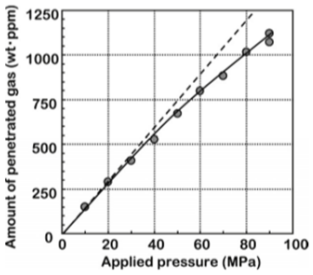

Figure 1.11: Hydrogen permeation per unit mass of HDPE at different pressure values [27]

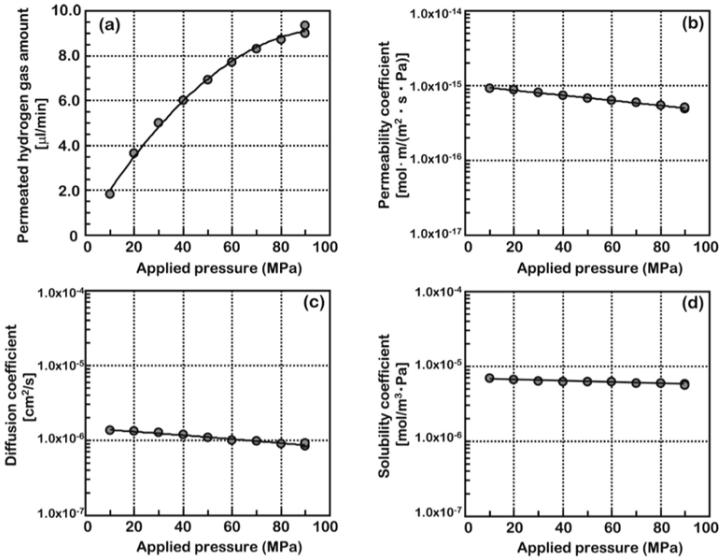

Figure 1.12: Pressure dependence of the permeation coefficients [27]

Cristallinity and Cross-Linking

The effects of these two parameters on the permeation rate of hydrogen are discussed in the same section as they can be explained through the same reasoning, based on the free volume theory. A semicrystalline polymer presents both the closely packed crystalline region and the looser amorphous regions. According to Kloppfer and Flaconnèche [44], the crystalline zones act as impermeable zones to the gas, and their presence does not influence the sorption mode. Therefore, the effect of the crystallites of a semicrystalline polymer on its diffusivity and solubility compared to its theoretical pure amorphous form can be summed up in the following equations:

$$S = S^* \phi_a \tag{1.17}$$

$$D = \frac{D^*}{\beta \tau} \tag{1.18}$$

where D^* is the diffusivity of the amorphous phase while τ is the tortuosity factor, which is due to the presence of the crystallites that increase the effective path length of diffusion (figure 1.13). β is the chain immobilization factor. As the name suggests, it reflects the hindrance of the crystallites on the amorphous chains. S^* is the solubility of the theoretical completely amorphous polymer while ϕ_a is the volume fraction of the amorphous phase.

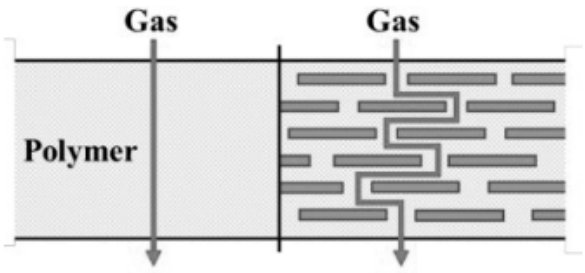

Figure 1.13: The tortuosity effect [79]

1.2. Experimental Evaluation Methods For Hydrogen Permeation

There are two different methods for the evaluation of hydrogen permeation through polymer based materials, as explained by Su et al. [79]

1.2.1. Thermal Desorption Analysis

Figure 1.14 provides an exhaustive step-by-step description of the analysis.
First, a disc-shaped sample is exposed to a high-pressure hydrogen environment (step 1). After some time, the sample is rapidly decompressed and put in a furnace at a set temperature (usually 30 C). The sample, now in a low-pressure environment, becomes supersaturated and the higher temperature increases the kinetic energy of the hydrogen particles, promoting their desorption. As the hydrogen particles start to desorb from the sample, they are purged by inert gas (Ar or He) or drawn by a vacuum through a gas chromatograph, which is equipped with a molecular sieve column (step 2(a)). The column is a material with tiny pores that can separate molecules of different sizes and shapes.
The eliminated hydrogen molecules are let through, then collected and measured. A curve of the eliminated H_2 is extrapolated (step 2(b)). The integral of this curve is the remaining hydrogen that diffuses through and out of the sample (step 3). The following diffusion equation is then fitted to the experimental data, in order to find the two unknowns D and $C_H(0)$ (amount of penetrated hydrogen) :

$$C_H(t) = \frac{32}{\pi^2} \times C_H(0) \times \left[\sum_{n=0}^{\infty} \frac{\exp\left(\frac{-(2n+1)^2\pi^2 Dt}{\ell^2}\right)}{(2n+1)^2} \right] \times \left[\sum_{n=1}^{\infty} \frac{\exp\left(\frac{-D\beta_n^2 t}{\rho^2}\right)}{\beta_n^2} \right] \tag{1.19}$$

Where $C_H(t)$ is the remaining hydrogen content (wt□ppm), D is the diffusion coefficient (mm^2/s), β_n is the root of the zero-order Bessel function, ℓ is the thickness of the sample, and ρ is the radius of the disk [27].

While this type of analysis is relatively simple and quick and works very well at low hydrogen pressures, its results are questionable at higher pressure values. This is because as the sample is decompressed, it becomes supersaturated with hydrogen molecules. The gas molecules therefore accumulate in the microvoids of the polymer causing stress concentrations and even damage to the material. For this reason, the TDA-measured permeability at high pressure is larger than the one measured with the second more accurate method, the High-Pressure Hydrogen Permeation Test (HPHP).

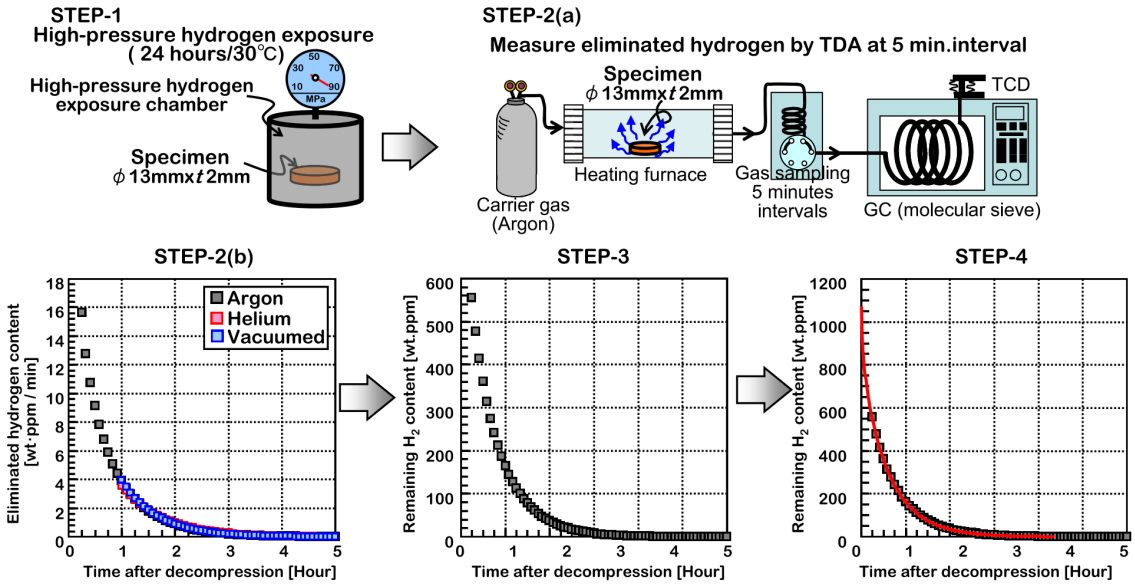

Figure 1.14: A summary of the TDA method [27]

1.2.2. High Pressure Hydrogen Permeation Test

This test is conducted by creating a pressure differential between the two sides of the specimen. On the downstream side, a gas rate measurement device like a mass spectrometer is placed. On the upstream side, hydrogen (or another tracer gas) is fed at high pressure. The mass spectrometer measures the amount of gas permeating and a permeability curve can easily be extrapolated. Figure 1.15 shows the setup that is used at the German Aerospace Center, which allows for the testing of multiple samples at the same time. Due to safety reasons, Helium is used as the tracer gas, due to its similar molecular size and inertness compared to H_2.

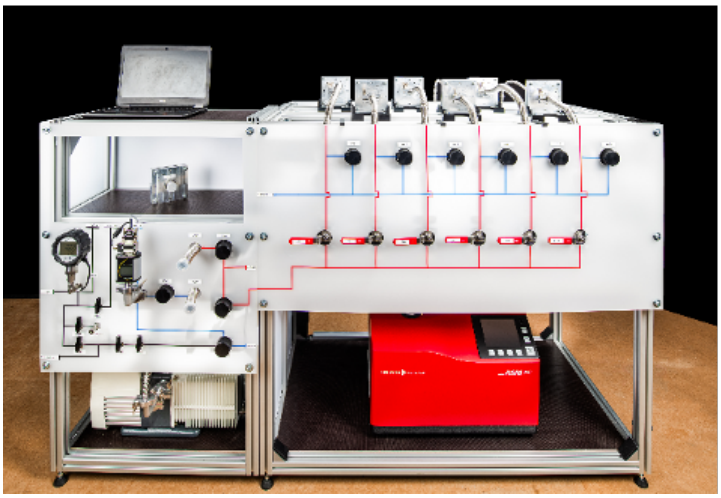

Figure 1.15: High Pressure Hydrogen Permeation Test. Courtesy of the German Aerospace Center (DLR)

According to Flaconnèche et al. [24], the permeability is then measured as

$$Pe = \frac{Q \cdot l}{t \cdot A \cdot \Delta P} \tag{1.20}$$

where Q is the amount of permeated hydrogen, l is the thickness of the specimen, t is the time, A is the area of the specimen, and ΔP pressure differential between the two sides.

During this test, the diffusion coefficient is obtained through the *time lag technique*. The time lag θ is a parameter that is extrapolated from the curve of the total amount of permeated hydrogen against time $Q(t)$. $Q(t)$ is given by the integral of the flux $J(t)$:

$$Q(t) = \int_0^t J(\tau)\, d\tau \tag{1.21}$$

therefore, integrating equation 1.7, we obtain the following equation for $Q(t)$:

$$Q(t) = \frac{DSp_{HPS}}{\ell}\left(t - \frac{\ell^2}{6D}\right) - 2\frac{\ell S\Delta p}{\pi^2}\sum_{n=1}^{\infty}\frac{(-1)^n}{n^2}\exp\left(-\frac{Dn^2\pi^2 t}{\ell^2}\right) \tag{1.22}$$

comparative graphs of $J(t)$ and $Q(t)$ for materials that exhibit Fickian behaviour are shown in figure 1.16.

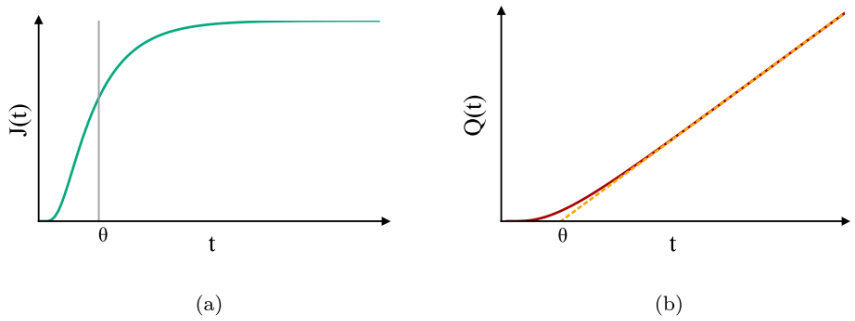

Figure 1.16: Typical curves for gas flux (a) and quantity of permeated gas (b) as functions of time. The dashed line in panel (b) is the fit of the Q(t) curve in stc (i.e. for $t \to \infty$) to a straight line [69]

The time lag technique is based on the observation that the $Q(t)$ curve can be divided into two parts: the transient part and the steady-state part. Initially, for $t \lesssim 5\theta$ the concentration of gas in the membrane varies until it reaches stationary conditions. During this period, the permeation rate is not constant. Once steady-state conditions are reached (for $t \to \infty$), $Q(t)$ becomes a straight line.

The equation for $Q(t)$ under these conditions is readily obtained from 1.22:

$$Q(t) = \frac{DSp_{HPS}}{\ell}\left(t - \frac{\ell^2}{6D}\right) = \frac{P_{HPS}}{\ell}(t - \theta) \tag{1.23}$$

where θ is the time lag. This equation shows that the $Q(t)$ curve intercepts the time axis at $t = \theta$. The time lag can therefore be used to determine the diffusion coefficient using the relationship:

$$D = \frac{\ell^2}{6\theta} \tag{1.24}$$

While the HPHP test requires much more complex equipment to handle the high pressures, it produces more accurate results, thus it is the favorite method for the measurement of hydrogen permeation.

1.3. The Devanathan-Stachurski Cell Adaptation

1.3.1. Fundamental Design and Working Principle

The Devanathan-Stachurski (DS) cell was developed in 1962 as a direct response to the critical need for understanding and addressing hydrogen embrittlement in metals [19]. Hydrogen embrittlement is a phenomenon that occurs when atomic hydrogen, having permeated through a metal, interacts with the metal itself, subsequently reducing its ductility and strength. This process can lead to significant material degradation and potential catastrophic failures, especially in high-stress environments. This problem was particularly severe in industries reliant on high-strength steels, such as aerospace, nuclear, and petrochemical sectors, where hydrogen exposure could result in blistering, cracking, and premature failure of critical components [68]. The DS cell was therefore designed to provide accurate measurements of hydrogen permeation across metallic membranes, allowing researchers to quantify the rate at which hydrogen atoms diffuse through the metal lattice and to study the underlying mechanisms of hydrogen embrittlement.

The fundamental design of the DS cell involves sandwiching a thin metallic membrane between two independent electrochemical compartments: the charging side and the detection side. Hydrogen is evolved at the metal membrane's surface on the charging side, where it dissociates into atomic hydrogen that then diffuses through the metal lattice. On the detection side, these hydrogen atoms are oxidized, generating a measurable current that directly correlates with the rate of hydrogen permeation through the membrane [18]. The driving force of the diffusion process is the concentration gradient, as explained in 1.1.3. A schematic representation of the Devanathan-Stachurski setup is shown in figure 1.17 below.

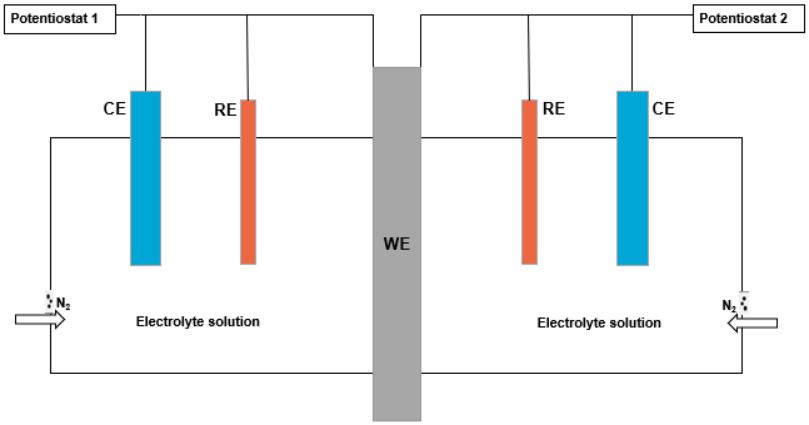

Figure 1.17: Schematic diagram of the Devanathan-Stachurski cell

The sensitivity and accuracy of hydrogen permeation measurements using the DS cell are made possible by the high-resolution potentiostat, which can detect extremely small currents down to the femtoAmpere (fA) range. This precision enables the reliable detection of minute current fluctuations caused by the oxidation of hydrogen atoms (usually in the range of nA to μA), allowing for accurate calculations of diffusivity and permeability coefficients. The side responsible for oxidizing atomic hydrogen must be polarized anodically to the hydrogen equilibrium potential. This requirement can pose significant challenges as metals must become highly passive to ensure that the background corrosion current remains low enough for the hydrogen transport-related current to be accurately resolved. Moreover, the anodic polarization can lead to the formation of a passive oxide layer on the surface of non-noble metals, which has been shown to impede the diffusion of hydrogen atoms. This results in hydrogen accumulation at the metal-oxide interface, where it cannot be oxidized, leading to a loss of signal [55].

1.3.2. Selection of Palladium Coating for Permeation Experiments

Palladium (Pd) was selected as the coating material for the polymer samples in the H_2 electrochemical permeation technique due to its unique ability to absorb large quantities of hydrogen under ambient conditions. Unlike most metals, which require elevated pressures or temperatures to form hydrides, palladium readily forms palladium hydride (PdH_x) at room temperature and atmospheric pressure. This capacity is due to palladium's face-centered cubic lattice structure, which enables hydrogen atoms to occupy interstitial octahedral sites without disrupting the lattice itself. Moreover, Pd is particularly suited for hydrogen diffusion studies due to its unique ability to dissociate hydrogen molecules into atoms without requiring additional activation energy. Unlike other metals, this process occurs naturally on palladium's surface, allowing hydrogen atoms to diffuse into the lattice under ambient conditions [1]. This activation-free pathway ensures that hydrogen is absorbed and desorbed from the palladium surfaces in both cells of the DS setup without the need for high pressures or temperatures. In addition, palladium exhibits a noble character that prevents oxide layer formation, even under the anodic potentials necessary for hydrogen oxidation. This property is particularly advantageous, as oxide layers would otherwise impede the hydrogen absorption and diffusion processes.

However, palladium also has its own set of limitations and drawbacks. As palladium absorbs hydrogen below its critical temperature of 571 K (298°C) and pressure 2 MPa, it undergoes a phase transformation, resulting in the formation of two distinct phases, α and β (figure 1.19). Both phases retain the face-centered cubic (FCC) structure of palladium but differ in lattice parameters—expanding from 0.3890 nm (hydrogen-free palladium) to 0.3895 nm for the α-phase and up to 0.410 nm for the β-phase. The α-phase forms at low hydrogen concentrations and high temperatures, while the β-phase forms at higher hydrogen concentrations and lower temperatures. The coexistence of these phases can cause internal strain and lead to defects like recrystallization, grain boundary issue. Finally, Palladium is also affected by hydrogen embrittlement, which reduces the ductility of the metal and may cause it to fracture [91].

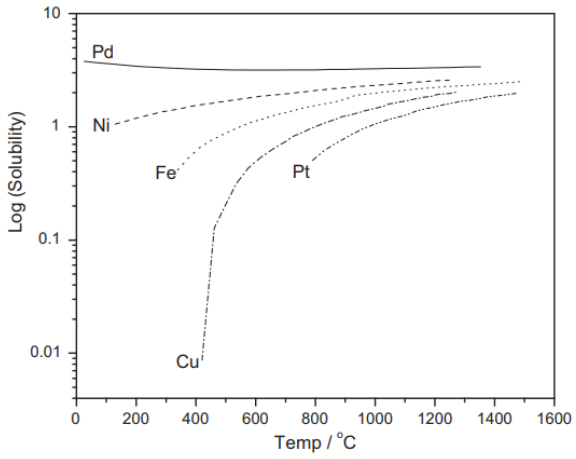

Figure 1.18: Comparison of hydrogen solubility in several metals at a pressure of 1 atm. Solubility is given units of standard cm^3 of H_2 per 100 g of metal [91]

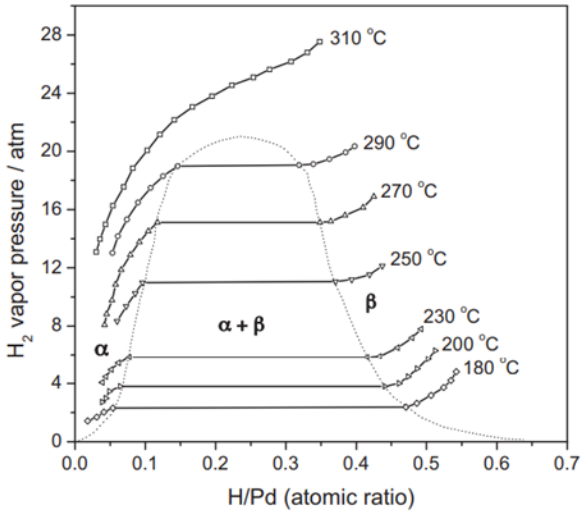

Figure 1.19: PCT phase diagram of the palladium-hydrogen system [91]

As the DS cell continued to be used and adapted for a wider range of metals, researchers found it necessary to coat the detection side of non-palladium membranes with a thin layer of palladium [55, 46, 70, 51, 82]. This approach allowed for the benefits of palladium's properties to be leveraged while studying other metals, ensuring the accuracy and reproducibility of the hydrogen permeation measurements.

1.3.3. Adaptations of the Setup to Polymer Materials

Over the decades, the DS cell setup has been explored as a tool to evaluate the performance of polymer coatings on metal substrates [14, 88]. With the growing interest in hydrogen fuel cells, which rely on polymeric proton exchange membranes, the DS cell has also been used to assess oxygen permeation through these membranes [38].In fuel cells, this is an unwanted phenomenon that leads to loss of potential fuel. Understanding how much oxygen permeates from the anode to the cathode side is crucial for improving the efficiency of these systems. These studies marked an shift from traditional metal-focused research to the investigation of the permeability properties polymeric materials using the electrochemical method and they were instrumental in shaping the approach to this thesis project. These papers provided insights into the reactions occurring in setups similar to the one that was originally envisioned at the start of the project, guiding the design of the following experiments, including the choice of electrolyte, thickness and deposition method of the palladium coating, and the selection of appropriate potentials and currents for the hydrogen entrance and exit sides. In particular, the study [14] by Bucur and Mecea, focused on the diffusion of hydrogen through a PET membrane using a modified DS setup, where the charging side was filled with gaseous H_2. The detection side employed the classical three electrode setup, with the working electrode being a thin (80 nm) Pd layer that had been chemically plated on the polymer surface. The gaseous hydrogen that permeated through the PET membrane was therefore oxidised at the palladium surface. The researchers successfully obtained a reproducible permeation curve. However, the coefficients of diffusion and permeability were not in accordance to those that had been previously found through high pressure permeation tests. Most importantly, the researchers highlighted a critical issue when adapting the DS cell setup to non-conductive polymer materials: the potential detachment and loss of the palladium coating during experiments. This issue was particularly evident on the charging side, where hydrogen was being introduced in significant quantities. The very thin palladium coating, which is essential for enabling hydrogen permeation through the membrane, initially adhered well but began to detach after the first hydrogen charging cycle at atmospheric pressure. This detachment occurred due to the significant lattice expansion caused by the saturation of hydrogen in the β-phase, a situation exacerbated by the large amounts of hydrogen forced into the material on the charging side.

On the detection side, however, this problem did not arise. Here, the permeating hydrogen was rapidly oxidized, preventing the buildup of hydrogen within the palladium coating. The takeaway is that as long

as the overpotential on the detection side is sufficiently high, the hydrogen is quickly oxidized, preventing its concentration from rising to a level that would cause phase changes in the palladium, thereby avoiding any swelling or detachment of the coating. In the study, the detachment of the palladium coating on the charging side was not a significant issue because the researchers modified the charging cell to introduce hydrogen in gaseous form, thus bypassing the need for electrochemical processes on that side. However, this issue becomes particularly critical in the context of the present project, where hydrogen is evolved electrochemically on the charging side. In this setup, a conductive metal surface is required to serve as the cathode in the electrochemical charging cell, making the palladium coating indispensable. Ensuring the integrity of this coating is therefore paramount. The challenge of preventing detachment and delamination of the palladium layer is a central focus of this project, as the stability of the palladium coating is crucial for obtaining accurate and reliable measurements.

The study by Vijayshankar et al. [88] presents an insightful adaptation of the Devanathan-Stachurski (DS) cell, focusing on assessing the performance of an organic PVB coating in preventing corrosion of the underlying metal surface. This study is particularly relevant to the current project due to the similarities in the experimental setup, as both projects employ a polymer-palladium system as the test specimen.

The research provides a thorough description of the experimental setup, particularly justifying the use of an acidic electrolyte on the charging side and an alkaline electrolyte on the exit side. In the charging cell, where hydrogen evolution occurs, the acidic electrolyte supplies protons (H^+) necessary for the reduction reaction at the palladium electrode, promoting the evolution of hydrogen atoms at the metal surface.

Conversely, the detection cell utilizes an alkaline electrolyte to facilitate the oxidation of hydrogen atoms that have permeated through the membrane. The alkaline environment supports the hydrogen oxidation reaction by supplying OH^- ions. In summary, the electrolytes serve as a conductive medium, ensuring the efficient flow of ions and facilitating the overall electron transfer processes across the electrochemical cells. Furthermore, the researchers analyzed the relationships between entry current and entry potential, as well as exit current and exit potential. This analysis offered valuable insights that guided the selection of entry currents and exit potentials to ensure the integrity of the palladium coating and to achieve accurate and reproducible results.

The foundational studies reviewed in this section have been instrumental in shaping the design and execution of the current research, which seeks to quantify hydrogen permeation through polymer-based materials intended for use in hydrogen storage tanks for electric commercial aviation. These studies have highlighted the versatility of the Devanathan-Stachurski (DS) cell and its potential for adaptation to new materials, leading to its application in the study of hydrogen permeation in polymers—a central focus of this thesis.

By applying the DS cell to the study of hydrogen permeation in polymers, this research explores new frontiers in assessing the potential of these materials for the development of sustainable aviation technologies. The upcoming section will detail the specific objectives and methodologies of this research, laying the groundwork for the experimental work that will follow.

1.4. Scope of Master Thesis

The shift towards hydrogen fuel introduces several challenges, with the primary concern being the safe storage of hydrogen needed to sustain the flight range of current commercial airplanes. To avoid the hazards of high-pressure tanks on board, hydrogen would need to be stored in its liquid form at cryogenic temperatures, making the lightweight and high-strength type III, IV, and V tanks potential candidates. However, before fully assessing these storage options, a fundamental understanding of hydrogen permeation through polymers and polymer-based composites is needed.

Existing methods like Thermal Desorption Analysis and High Pressure Hydrogen Permeation Testing present complexities and safety risks in handling hydrogen gas. This thesis aims to explore whether an electrochemical technique used to evaluate hydrogen embrittlement in metals could be adapted to safely and accurately evaluate hydrogen permeation through polymer specimens.

The primary objective of this thesis is to develop and validate a novel adaptation of the DS cell to measure hydrogen permeability through polymers. This will involve:

- **Adaptation of the Devanathan-Stachurski cell to polymer based materials**: Modifying the traditional DS cell setup, which has been primarily used for metals, to accommodate and effectively test polymer-based materials. This includes designing the setup, understanding the chemical reactions occurring at the electrodes in both cells, and determining the optimal combination of entry current, exit potential, electrolyte type, and concentration. These factors are critical for evolving and oxidizing hydrogen at the palladium-coated surfaces without damaging the coating, ensuring accurate and reproducible results. Additionally, the coating process of the polymer must be thoroughly explored to optimize the palladium layer's adhesion and integrity.
- **Experimental validation**: Conducting a series of experiments to compare the hydrogen permeability data obtained from the DS cell setup with existing data from TDA and HPHP methods. This will establish the validity and reliability of the DS cell as a permeability testing tool for polymers. The experiments will be conducted on carefully selected polymeric materials that meet specific criteria, ensuring that the test setup can accurately determine permeability values across a wide range of materials. This will demonstrate the setup's capability to study polymer-based materials with varying properties effectively. The process involved investigating and applying different methods for calculating D and P, with each method offering a distinct interpretation of the underlying physical mechanisms of hydrogen permeation. Although all methods are based on the same experimental data, they produce values that have slightly different physical meanings because they describe different aspects or mechanisms of the permeation process.
- **Obtaining quantifiable information on permeation of Hydrogen through the Electrochemical Monitoring Technique**: A major portion of this thesis was dedicated to identifying the best methods for extrapolating critical parameters from the experimental data—parameters that are essential for understanding hydrogen permeation through polymers and comparing results across different materials. These parameters, namely the diffusion coefficient (D) and permeability (P), are crucial not only for comparing with existing literature but also for evaluating how hydrogen permeates through various polymeric materials tested using the electrochemical monitoring technique.
  The process involved investigating and applying different methods for calculating D and P, with each method offering a distinct reflection of the underlying physical mechanisms of hydrogen permeation. Although all methods are based on the same experimental data, they produce values that have slightly different physical meanings because they depict different aspects or mechanisms of the permeation process.
  A significant effort was made to explain the physical meaning of each method, analyze how it captures and describes the permeation mechanism, and ultimately select the method that provides results best suited for comparison with existing literature. This also ensures that the chosen approach allows for meaningful comparisons of hydrogen permeability across various materials, offering insights into how hydrogen permeates through each specific polymer type.

This thesis will contribute to the field of hydrogen storage materials by providing a new and unexplored approach to evaluating hydrogen permeability in polymers. The adaptation of the DS cell for polymer materials represents a significant advancement in testing methodologies, offering a safer and more accessible alternative to existing high-pressure and destructive techniques. A schematic overview of the different testing methods is shown in figure 1.20 for comparison.

In summary, this thesis seeks to extend the application of the DS cell beyond metals, exploring its potential to become a standard tool for hydrogen permeability testing in polymers. The successful adaptation of this electrochemical setup could pave the way for further innovations in the development of hydrogen storage technologies, contributing to the broader goal of sustainable aviation.

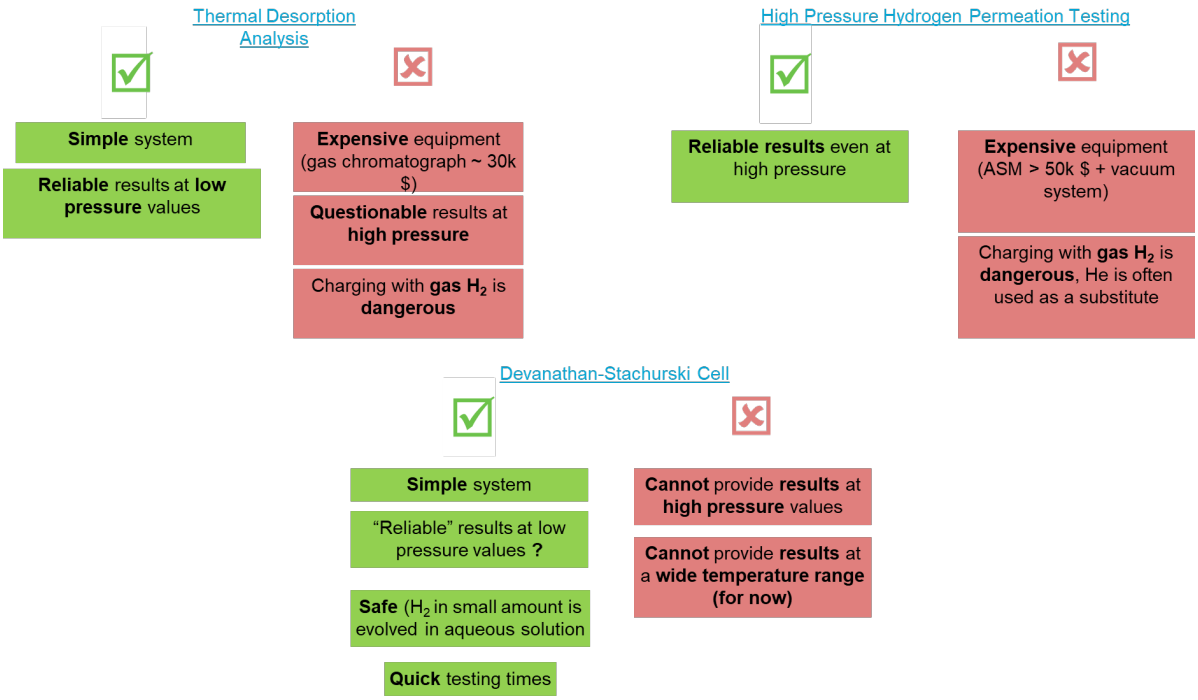

Figure 1.20: Overview of the state-of-the-art testing methods and comparison with the proposed Devanathan Stachurski cell adaptation

2

Methodology

2.1. Materials

2.1.1. Setup

Two glass electrochemical cells with a capacity of 100 ml, equipped with PTFE lids and O-rings, were purchased from Laborxing. Additionally, two Ag/AgCl reference electrodes (0.197 V vs SHE) were obtained from the same supplier. The two Platinum counter electrodes used in the experiments were already available in the laboratory.

2.1.2. Electrolytes

Throughout the project, two different electrolytes were used in the Devanathan Stachurski cell. For the charging cell, various concentrations of H_2SO_4 were employed. Similarly, different concentrations of NaOH were used in the detection cell. Both the 96% concentrated H_2SO_4 and NaOH were sourced from Sigma Aldrich.

2.1.3. Sample Materials

Three different polymer materials were selected for testing based on their permeability. To validate the testing method, it was important to assess whether comparable results could be obtained with respect to existing literature. Therefore, the materials were chosen to represent a broad range of permeability values:

- HDPE (high-density polyethylene): A material with extremely low permeability.
- PEEK (polyetheretherketone): A material with intermediate permeability.
- PP (polypropylene): A material with high permeability.

These materials were also selected because literature data on their diffusivity and permeability values is readily available, enabling a more straightforward comparison. The materials were sourced from the following suppliers:

- HDPE: Acquired from S-Polytec.
- PEEK: Acquired from Goodfellow.
- PP: Acquired from Lasersheets.

Differential Scanning Calorimetry (DSC) was used to determine the degree of crystallinity of the samples. The crystallinity was calculated using the following equation:

$$\chi_C = \frac{\Delta H_m - \Delta H_{CC}}{\Delta H_m^{100\%}} \tag{2.1}$$

where:

- χ_C: Degree of crystallinity,
- ΔH_m: Enthalpy of fusion of the sample,
- ΔH_{CC}: Enthalpy of cold crystallization (if present),
- $\Delta H_m^{100\%}$: Enthalpy of fusion of a fully crystalline sample [20].

The density of the samples was measured using the water displacement method [4]. The density data was then utilized to calculate another value for crystallinity by comparing the measured sample density with the densities of fully crystalline and fully amorphous polymers, as described by the equation:

$$\chi_C = \frac{\rho - \rho_a}{\rho_C - \rho_a} \tag{2.2}$$

where:

- ρ: Density of the sample,
- ρ_C: Density of a fully crystalline sample,
- ρ_a: Density of a fully amorphous sample.

Crystallinity was measured using both DSC and density-based methods, as each technique yields different results. Researchers have reported using either method prior to permeability testing.

Table 2.1 summarizes the results of these tests and provides an overview of the key characteristics of the tested polymers. Further data, including chemical structure, DSC results and crystallinity calculations are presented in Appendix A. A literature survey on diffusivity and permeability values for these polymers is available in Appendix B.

Table 2.1: Properties of HDPE, PEEK, and P

Property	**HDPE**	**PEEK**	**PP**
Density (g/cm^3)	0.946	1.294	0.913
χ_c **(Density method, %)**	79	25	65
χ_c **(DSC method, %)**	53	34	38
T$_g$ (°C)	-115 [9]	147 (DSC)	- 8 [34]
Notes			70 % isotactic

2.1.4. Palladium Coating

To deposit a thin palladium coating onto the polymer surfaces, Physical Vapor Deposition (PVD), specifically sputter coating, was utilized. A palladium sputter target compatible with the Quorum Q300T-D Plus sputtering machine in the laboratory was acquired from Aurion.

2.2. Methods

2.2.1. Sample Surface Preparation

The samples prepared for the experiment were 20 x 20 mm squares with a thickness ranging from 0.5 to 1.5 mm. The thickness was carefully chosen to enable the analysis of one-dimensional permeation through the membrane. According to the literature, to ensure accurate one-dimensional permeation, the ratio of the radius of the area of analysis to the thickness of the membrane should be 5:1 or greater

[5]. In our setup, the exposed area was a circle with a 7.5 mm radius, making the chosen thickness range appropriate for the study.

To prepare the surface of the samples for coating, both sides were sequentially ground using 180, 300, 500, 800, 1200, 2000, and 4000 grit sandpaper. After grinding, the samples were ultrasonically cleaned in isopropanol, followed by distilled water, and then left to air dry in a desiccator overnight.

Given that the adhesion of the palladium coating presented challenges with some materials, particularly HDPE, the samples were also subjected to corona treatment before the coating process. Finally, all samples were placed in the Quorum Q300TD sputtering machine and coated with a 100 nm thick layer of pure palladium. An example of a finished sample is provided in figure 2.1 below.

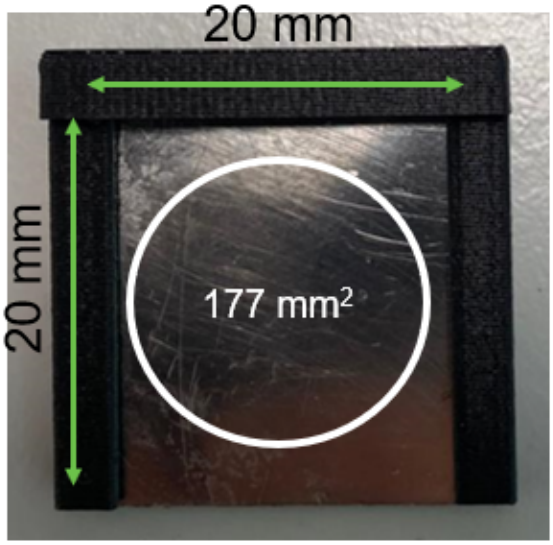

Figure 2.1: Coated sample ready for electrochemical permeation testing. The area exposed to the electrolyte is marked in white.

2.2.2. Devanathan Stachurski Cell

The Devanathan-Stachurski cell setup designed for this experiment is shown in figure 2.2 below. The schematic image provides a detailed view of the different components and their arrangement within the setup, while the second image shows the actual assembled setup used in the laboratory. Labels and arrows on both images indicate the key components. Two potentiostats were used to apply a constant current on the charging side (left in figure 2.2a and a constant potential on the detection side (right in figure 2.2a) respectively. Potentiostat 1 is an Autolab PGSTAT100N [6] and Potentiostat 2 is an Ivium Compactstat Standard [16].
In a classic Devanathan-Stachurski setup, the two independent potentiostats are connected to the same conductive working electrode, which is grounded to provide a stable reference. The potentiostats, however, are used in floating mode, meaning they are not grounded themselves. This configuration ensures that the two potentiostats can independently control the electrochemical processes on each side of the working electrode without creating conflicts, while the grounded working electrode provides a stable electrical reference point for accurate hydrogen permeation measurements. Additionally, grounding the working electrode is important for protecting the equipment from potential electrical damage or interference, ensuring safe and reliable operation.
In the Devanathan-Stachurski setup used in this project, however, the situation is different. Since the sample material is a non-conductive polymer, there is no electrical connection between the two Pd coats, which therefore serve as independent working electrodes for the two electrochemical cells. In this case, the sample is not grounded, while the two potentiostats are. Grounding the potentiostats is crucial as it ensures electrical stability and a common reference point for the measurements. This prevents potential discrepancies between the two cells, avoids interference, and ensures accurate control

over the electrochemical processes, ultimately protecting the integrity of the experiment and the equipment [57].

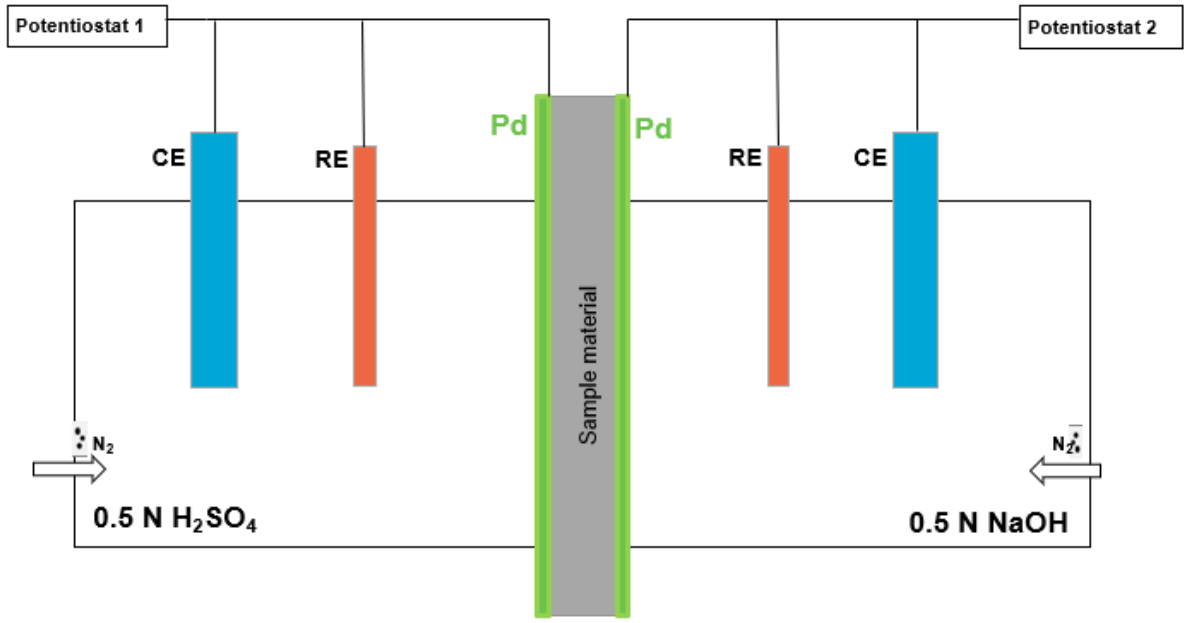

(a) Schematic Diagram

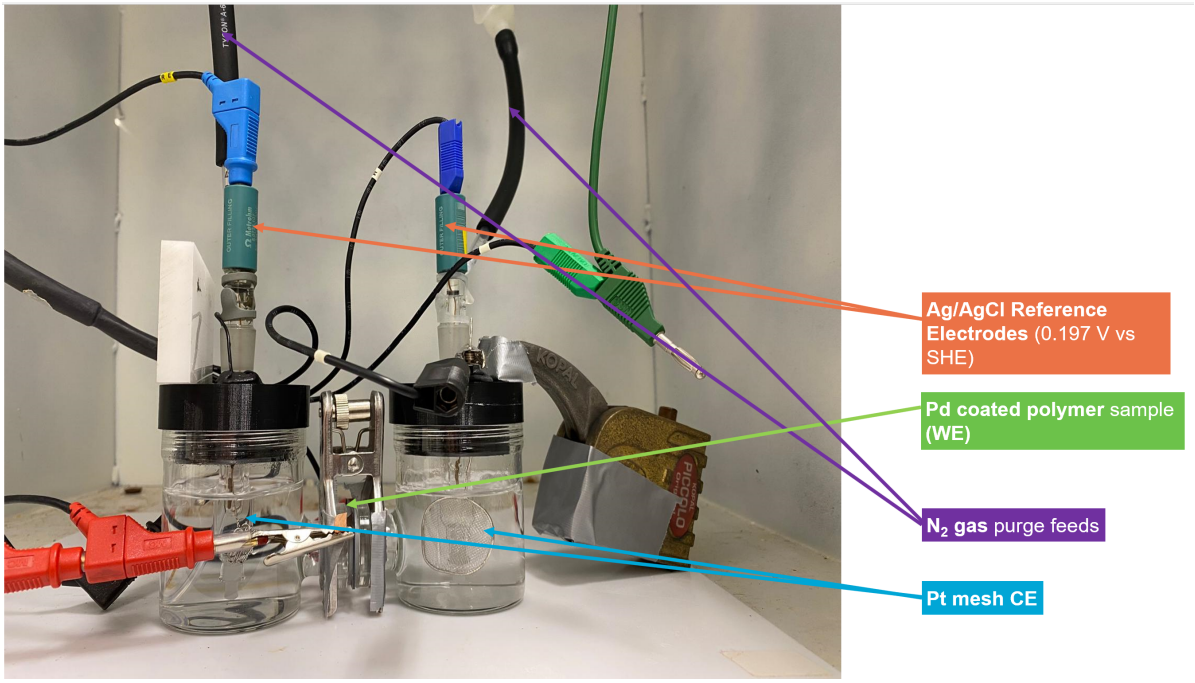

(b) Laboratory Setup

Figure 2.2: The adapted Devanathan-Stachurski cell developed for this project.

Test Procedure

The final test procedure is reported in Figure 2.3b. During the entire test, nitrogen gas (N_2) is bubbled in both cells. The rationale behind this, as well as the selection of the specific detection potential and

charging current values, are detailed in the Results chapter (see Chapter 3). These elements are discussed in the Results section because the setup was developed as part of this thesis. Since the process of determining and validating the setup is a significant part of the experimental findings, its optimization and validation contribute directly to the overall results of the project.

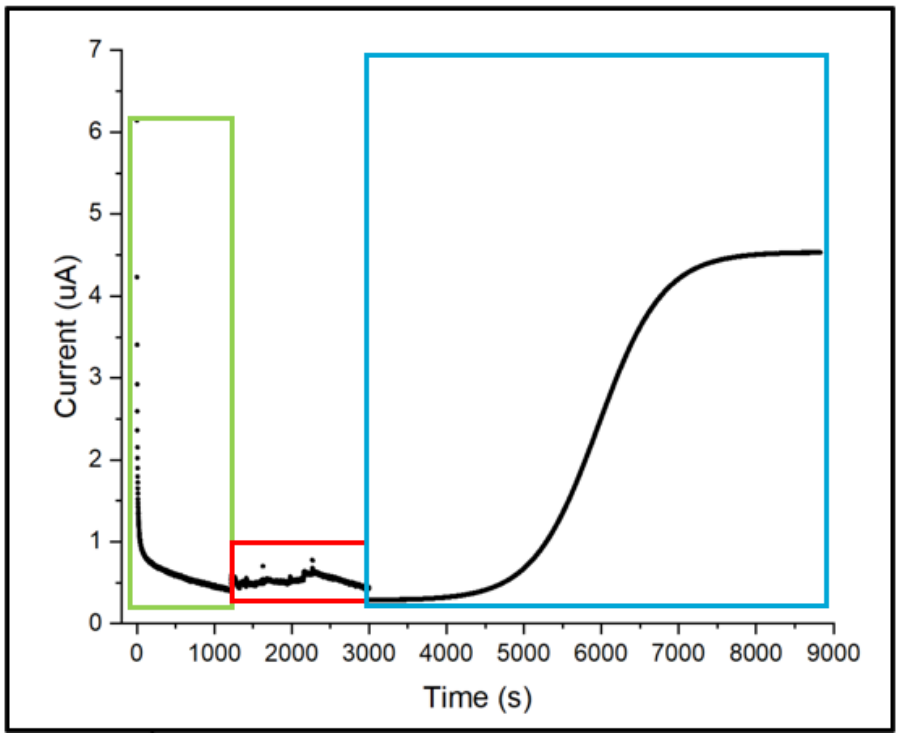

(a) Example of permeation graph obtained through EMT

Stage	Process	Entry Side	Exit Side
Stage 1	Passivation	-	Introduction of alkaline electrolyte Apply: E = 0.2 V vs Ref until current is steady and less than 0.3 µA/cm²
Stage 2		Introduction of acid electrolyte	Maintain E = 0.2 V
Stage 3	Charging	Apply I = - 0.5 mA	Maintain E = 0.2 V

(b) Test Procedure

Figure 2.3: Final test procedure developed for the Electrochemical Monitoring Technique of polymer materials

2.2.3. LN_2 Exposure

All three polymer samples were exposed to liquid nitrogen, undergoing 10 cycles of 2 minutes in LN_2, followed by 6 minutes at room temperature. This procedure was designed to simulate the conditions of liquid hydrogen tanks, where repeated cycles of emptying and refilling can cause sudden temperature shifts of a couple hundred degrees Celsius. The goal was to observe whether these extreme conditions would affect the diffusivity and permeability of the polymers.

3

Results and Discussion

This chapter presents and elaborates on the results obtained during the course of this thesis project, following the chronological progression of the research. The initial objective of this work was to investigate whether an electrochemical method, traditionally used for measuring hydrogen permeation in metals, could be adapted to polymeric samples. The goal was to develop a safer, more accessible, and easily constructed alternative to current hydrogen permeation testing methods.

Following the literature review, the project began by adapting the traditional Devanathan Stachurski setup to polymer samples (3.1). The process started by examining the electrochemical reactions within the proposed setup (3.1.1) and the specific behavior of permeating hydrogen at the Palladium-polymer interfaces (3.1.2). Understanding these reactions was essential to ensuring that the experimental results would accurately reflect the hydrogen permeation mechanisms in polymeric materials. Additionally, this understanding guided the selection of appropriate potentials and currents for the Palladium-coated working electrodes, optimizing the adsorption and oxidation of hydrogen, as described in 3.1.3,3.1.4. Once the setup and protocol had been established and implemented, the key focus became determining how to extract quantifiable and comparable data that accurately captured the complex permeation behavior. This process is discussed in 3.1.5.

The results for the three polymers tested—PEEK, HDPE, and PP—are then presented and analyzed in section 3.2, and respectively in subsections 3.2.1,3.2.2 and 3.2.3. After this, the data obtained for the three polymer is compared to discuss how the architecture and chemistry of each individual polymer impacted the permeation process (3.2.4). Lastly, the effects of cryogenic exposure on the samples are explored in 3.2.5.

3.1. Development of the Devanathan Stachurski Setup

3.1.1. Electrochemical Reactions at the Electrodes

A schematic representation of the test setup is provided in Figure 3.1. The left compartment, containing an acidic electrolyte, functions as the hydrogen charging (input) cell. In this cell, hydrogen is evolved at the surface of the Palladium-coated working electrode by applying a constant cathodic current. A portion of the hydrogen atoms (H) are absorbed into the Palladium lattice. Driven by the concentration gradient, these hydrogen atoms diffuse through the Palladium layer, recombine into H_2 at the Pd-polymer interface, and continue diffusing through the polymer material towards the right side of the setup.

The right compartment, known as the hydrogen detection (output) cell, contains an alkaline electrolyte. In this cell, the hydrogen molecules that permeated through the polymer undergo dissociation into atomic hydrogen at the polymer-Pd interface. The atomic hydrogen reaches the Palladium surface and is oxidized under a constant anodic potential, producing protons (H^+) and electrons (e^-). The protons

react with OH^- from the alkaline electrolyte to form water, while the electrons are recorded as current flowing through the potentiostat. The resulting current vs. time curve is known as the permeation transient, which characterizes the hydrogen permeation behavior through the polymer.

The Palladium coatings in this setup serve as catalysts for the hydrogen evolution and oxidation reactions. Given that the Palladium coating is extremely thin (approximately 100 nm) compared to the polymer sample (0.5–1 mm), and that hydrogen transport through the polymer is much slower than the evolution/oxidation reactions at the Pd surfaces, it can be confidently assumed that the current-time curve accurately represents the hydrogen permeation through the bulk polymer material.

As shown in Figure 3.1, N_2 gas is continuously bubbled through both cells during the experiment. This is done to remove any dissolved O_2 present in the electrolyte solutions. The presence of oxygen can interfere with the experiment by reacting with the adsorbed hydrogen on the Palladium surface, as illustrated by the following reaction:

$$4\,H_{ads} + O_2 \longrightarrow 2\,H_2O \tag{3.1}$$

On the charging side, this reaction reduces the amount of hydrogen available for permeation, as the oxygen consumes hydrogen before it can diffuse through the polymer. On the detection side, oxygen acts similarly to the applied anodic potential by oxidizing the hydrogen atoms, which results in a loss of signal and thus affects the accuracy of the measurement [88].

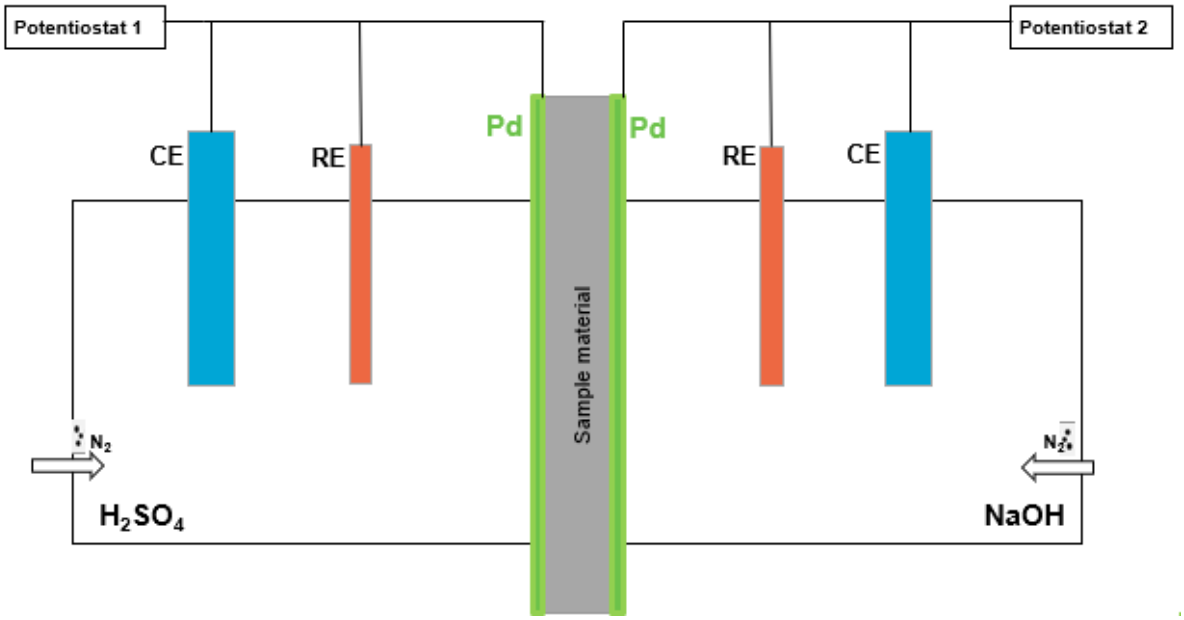

Figure 3.1: Schematic representation of the Devanathan Stachurski setup developed for this project.

Charging Side

A schematic representation of the reactions occurring at the electrodes on the charging side is provided in Figure 3.2 below.

The charging cell consists of a three-electrode setup, featuring an Ag/AgCl reference electrode (0.197 V vs SHE[1]), a Platinum counter electrode (anode), and the Palladium working electrode (cathode). The behavior of the Pt counter electrode and the Pd working electrode is dictated by the applied current. In this case, a cathodic current is applied, which causes electrons to flow toward the working electrode (Pd) and away from the counter electrode (Pt).

[1]The Standard Hydrogen Electrode (SHE) is a reference electrode consisting of a Pt electrode immersed in a 1 M H^+ ion solution, with H_2 gas bubbled over the electrode at 1 atm and 25 °C. The half-reaction occurring at the SHE is: $2\,H^+(aq) + 2\,e^- \longrightarrow H_2(g)$. Under these standard conditions, the electrode potential of the SHE is defined as 0.00 V, serving as a universal reference for measuring the potentials of other half-cell reactions [41].

At the anode (counter electrode), the oxygen evolution reaction occurs in acidic media [72]:

$$\mathrm{H_2O} \longrightarrow \frac{1}{2}\,\mathrm{O_2} + 2\,\mathrm{H^+(aq)} + 2\,\mathrm{e^-} \tag{3.2}$$

At the cathode, the hydrogen evolution reaction (HER) takes place, which proceeds through multiple steps. The initial step is the Volmer adsorption reaction in acidic media:

$$\mathrm{H^+(aq)} + \mathrm{e^-(m)} + \mathrm{M} \longrightarrow \mathrm{MH_{ads}} \quad \text{(Volmer)} \tag{3.3}$$

where M represents a vacant site on the Pd surface. Following the Volmer step, three parallel reactions occur: the Heyrowski, Tafel, and hydrogen absorption reactions:

$$\mathrm{H^+(aq)} + \mathrm{e^-(m)} + \mathrm{MH_{ads}} \longrightarrow \mathrm{H_2(g)} + \mathrm{M} \quad \text{(Heyrowski)} \tag{3.4}$$

$$2\,\mathrm{MH_{ads}} \longrightarrow \mathrm{H_2(g)} + 2\,\mathrm{M} \quad \text{(Tafel)} \tag{3.5}$$

$$\mathrm{MH_{ads}} \longrightarrow \mathrm{MH_{abs}} \quad \text{(Absorption)} \tag{3.6}$$

As shown in the equations, both the Heyrowski and Tafel reactions are desorption processes (the former electrochemical, the latter physical), resulting in the loss of hydrogen that might otherwise permeate through the polymer. In contrast, the absorption reaction in Equation 3.6 is the desired process, where hydrogen is absorbed into the metal lattice. This absorption step is also the rate-determining step, being the slowest of the three parallel reactions. Following this, the Tafel recombination is favored at low overpotentials[2], while the Heyrowski desorption is favored at high overpotentials [33, 30].

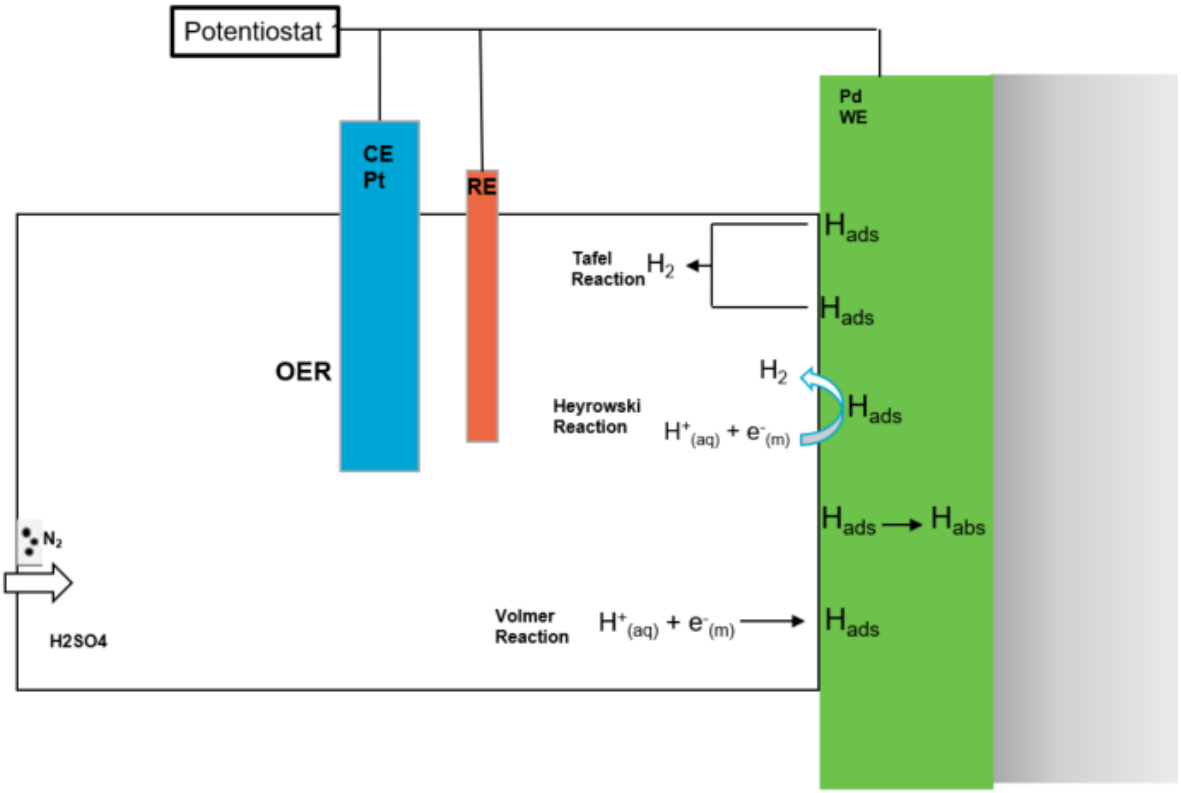

Figure 3.2: Schematic representation of the charging side of the Devanathan Stachurski setup developed for this project.

[2]In electrochemistry, overpotential refers to the additional potential required, beyond the reversible potential, to drive an electrochemical reaction. It accounts for inefficiencies in the system, including resistance in the electrode, electrolyte, and mass transport limitations. Overpotentials are negative for reduction reactions and positive for oxidation reactions [78].

Detection Side

A schematic representation of the reactions occurring at the electrodes on the detection side is provided in Figure 3.3 below.

The detection cell has the same configuration as the charging cell, with the difference being that the working electrode (Palladium) now acts as the anode while the counter electrode (Platinum) is the cathode, due to applied anodic potential.

At the cathode, the hydrogen evolution reaction occurs in alkaline media in the absence of dissolved oxygen in the solution [72]:

$$2\,H_2O + 2\,e^- \longrightarrow H_2(g) + OH^- \tag{3.7}$$

At the anode, the hydrogen oxidation reaction (HOR) takes place. This reaction is the inverse of the Volmer adsorption reaction shown in 3.3 in alkaline media:

$$MH_{ads} + OH^- \longrightarrow H_2O + e^-(m) + M \quad \text{(Inverse Volmer)} \tag{3.8}$$

In alternative to the Volmer step, the Tafel recombination reaction may also occur:

$$2\,MH_{ads} \longrightarrow H_2(g) + 2\,M \quad \text{(Tafel)} \tag{3.9}$$

(3.10)

this reaction is unwanted, as it results in a loss of signal and accumulation of hydrogen bubbles at the exit side. These surface bubbles create noise in the data and also represent hydrogen that is accumulated and cannot be oxidised, therefore raising the concentration of H_2 at the exit side and hindering the permeation process [86]. The Volmer reaction is favoured if enough oxidising overpotential is applied.

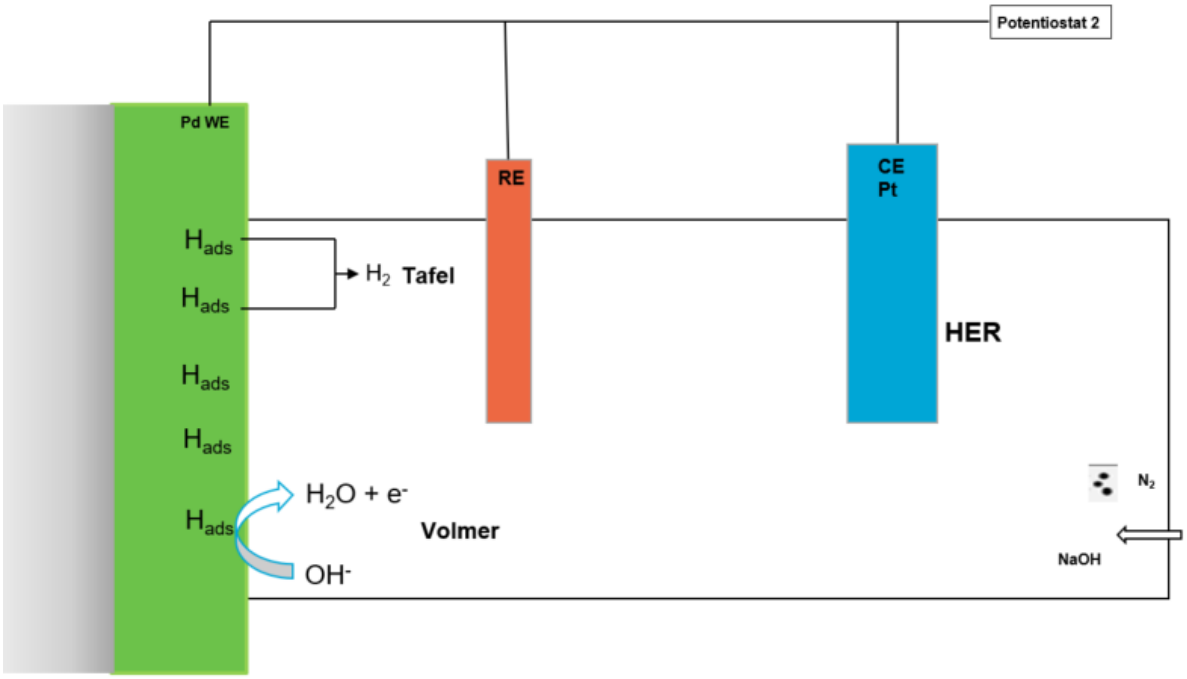

Figure 3.3: Schematic representation of the detection side of the Devanathan Stachurski setup developed for this project.

3.1.2. Absorption and Desorption of Hydrogen at the Pd - Polymer Interface

Figure 3.4 illustrates the recombination and dissociation mechanism of hydrogen atoms as they diffuse through the palladium and into the polymer sample, moving toward the exit (detection) side. This

mechanism has been reported for gaseous hydrogen permeation through polymer-coated steel hydrogen pipes [47]. While gaseous and electrochemical hydrogen permeation processes share all key stages — except for physisorption, which is merely the initial step in gaseous hydrogen permeation and does not affect subsequent processes [49] — it is reasonable to assume that a similar molecular hydrogen dissociation and recombination mechanism occurs in this setup. Furthermore, the recombination process is relatively fast compared to the diffusion of hydrogen through the bulk polymer, which remains the rate-limiting step in the overall permeation process[47].

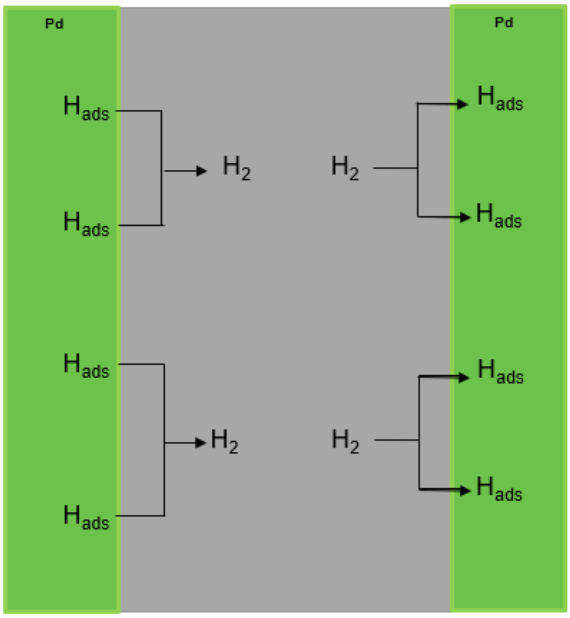

Figure 3.4: Schematic representation of the recombination/dissociation reactions of the H atoms as they diffuse through the Pd-coated polymer sample.

3.1.3. Selection of Detection Side Electrolyte and Potential

The initial selection of the electrolyte and oxidation potential was informed by the literature survey summarized in TableB.2 (Appendix B). Based on these findings, NaOH (alkaline) was identified as the most suitable electrolyte. While hydrogen oxidation could still occur in an acidic solution, an alkaline solution is more favorable for this system due to the presence of OH^- ions that enhance the hydrogen oxidation reaction (see equation 3.8). Furthermore, literature indicates that the concentration of the electrolytes (on both the detection and charging sides) has minimal influence on the kinetics of hydrogen evolution or oxidation, which are predominantly governed by the applied overpotential (specifically, the anodic potential on the detection side) [86]. Consequently, a concentration of 0.1 M NaOH was selected as the electrolyte for the detection side.

Additionally, the literature consistently shows that the applied anodic potential is always chosen to be slightly more positive (more anodic) than the open circuit potential[3], thereby ensuring that the oxidation reaction is favored while minimizing the risk of unwanted side reactions. To further refine the selection of an appropriate anodic potential, first cyclic voltammetry (CV) was employed to explore the potential range at which hydrogen oxidation occurs and to avoid the onset of undesirable side reactions. This allowed for a clear identification of the voltage window within which the system could operate effectively.

[3]The Open Circuit Potential represents the equilibrium state of the working electrode in contact with the electrolyte solution. At this potential, and in the electrochemical cell of interest for this project, the rates of hydrogen adsorption (a reduction process) and desorption or oxidation (an oxidation process) are balanced, meaning that the Palladium surface does not act as either a net anode or a net cathode [61].

Subsequently, the Pourbaix diagram was utilized to determine the upper limit of the overpotential that could be applied without initiating oxygen evolution, ensuring that the applied potential remained within the electrochemical stability region of palladium in the electrolyte solution.

Cyclic Voltammetry

The cyclic voltammetry conducted on the Pd-coated polymer sample in the detection side electrolyte solution is shown in figure 3.5. Cyclic voltammetry (CV) is an electrochemical technique that helps investigate the reduction and oxidation processes of molecular species by applying a cyclic voltage and measuring the resulting current. This technique allows the study of electron transfer reactions and provides insight into the thermodynamic and kinetic properties of the system under investigation. In CV, the applied potential is swept between two limits (forward and reverse) at a certain speed (scan rate, mV/s) while recording the current, creating a characteristic voltammogram that can reveal information about redox potentials and reaction mechanisms [22]. In this system, CV allows to explore the redox processes occurring on the palladium surface, including hydrogen adsorption/desorption and the water oxidation/reduction reactions.

The current peaks observed in a CV arise from electrochemical reactions occurring at the electrode surface. These reactions are governed by the Nernst equation, which relates the electrochemical potential to the concentration of reactants and products at equilibrium. For a general redox reaction:

$$\mathrm{Ox} + \mathrm{ne}^- \rightleftarrows \mathrm{Red} \tag{3.11}$$

the Nernst equation is expressed as [22]:

$$E = E^0 + \frac{RT}{nF} \ln \frac{[\mathrm{Ox}]}{[\mathrm{Red}]} \tag{3.12}$$

where:

- E is the electrode potential
- E^0 is the standard electrode potential
- R is the gas constant
- T is the temperature
- n is the number of electrons involved in the reaction
- F is the Faraday's constant
- Ox and Red are the concentrations of the oxidized and reduced species

Therefore, during the negative sweep (from 0.6 V to -0.8V), two main reduction peaks can be observed [90]:

- (b) Reduction of the Palladium Oxide layer between -0.3 V and -0.6 V:

$$\mathrm{PdO} + \mathrm{H_2O} + 2\,\mathrm{e}^- \longrightarrow \mathrm{Pd} + 2\,\mathrm{OH}^- \tag{3.13}$$

- (c) Reduction of water into ad/absorbed hydrogen from -0.6 to lower limit:

$$\mathrm{H_2O} + \mathrm{e}^- + \mathrm{M} \longrightarrow \mathrm{MH_{ads}} + \mathrm{OH}^- \tag{3.14}$$

On the other hand, during the positive sweep (from -0.8 V to 0.6 V), two oxidation processes can be observed [90]:

- (d) Hydrogen oxidation/desorption from -0.8 V to 0 V:

$$\mathrm{MH_{ads}} + \mathrm{OH}^- \longrightarrow \mathrm{H_2O} + \mathrm{e}^- + \mathrm{M} \tag{3.15}$$

- (a) Palladium Oxide formation starting at 0.2 V:

$$\mathrm{Pd} + 2\,\mathrm{OH}^- \longrightarrow \mathrm{PdO} + \mathrm{H_2O} + 2\,\mathrm{e}^- \tag{3.16}$$

As the applied potential becomes more negative, the Nernst equation predicts that the equilibrium shifts toward the reduction of molecular species in the system (such as water and PdO), resulting in reduction peaks corresponding to hydrogen adsorption and PdO reduction. Conversely, during the positive sweep, the equilibrium shifts toward oxidation, leading to peaks associated with hydrogen desorption and palladium oxidation.

From the cyclic voltammogram, it was determined that the potential range required to induce the oxidation of incoming hydrogen lies between -0.2 V and 0.2 V vs. the Ag/AgCl electrode. Within this range, increasing the potential enhances the kinetics of the hydrogen oxidation reaction, accelerating the rate at which hydrogen is oxidized.

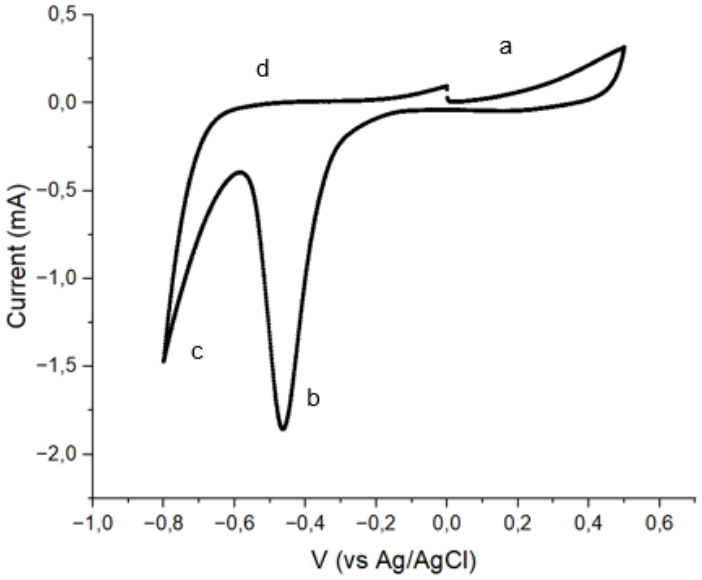

Figure 3.5: Cyclic Voltammetry of Palladium coated polymer sample in 0.1 M NaOH solution. Scan rate = 10 mV/s.

Pourbaix Diagram

The Pourbaix diagram of Palladium is shown in figure 3.6. Figure 3.6b zooms in on the region of interest, which is around the pH of the 0.1 M NaOH solution used on the detection side.
The Pourbaix diagram is a plot of the possible thermodinamically stable phases of an aqueous electrochemical system over a certain pH range. The sloping black lines on the diagram are equilibrium lines between different phases of palladium and its oxides [2]. Therefore it is possible to discern between three main phases:

- Below - 0.4 V vs Ag/AgCl Palladium remains stable in its solid metallic form.
- Between -0.4 V and 0.2 V vs Ag/AgCl, palladium exists in the form of Palladium Oxide. This indicates that under more oxidizing conditions, palladium forms an oxide layer on its surface. While PdO may passivate the surface to some extent, the hydrogen will still permeate through the layer and its oxidation is still possible. Also, it has been shown that the presence of occluded hydrogen may prevent the formation of palladium oxide at the electrode surface due to the following chemical reaction at the PdO interface [90]:

$$2\,\mathrm{H}^{\circ} + \mathrm{PdO} \longrightarrow \mathrm{Pd} + \mathrm{H_2O} \tag{3.17}$$

  where H° represents the occluded hydrogen.

- At potentials higher than 0.2 V vs Ag/AgCl, palladium forms palladium dioxide (PdO_2). This region represents even more oxidizing conditions, where palladium is in a higher oxidation state (+4). The formation of PdO_2 leads to complete surface passivation, and the thick oxide layer prevents

hydrogen permeation and oxidation. When this happens, the hydrogen concentration at the exit side does not stabilize but keeps rising as more and more H atoms accumulate at the oxide layer. Stationary conditions cannot be obtained and the results is a decay of the hydrogen flux at the end of the permeation transient [54].

The dotted lines delimit the water stability region. For applied potentials above the upper dotted line, water is oxidized (Oxygen evolution reaction) at the Palladium surface. In the alkaline environment, the following reaction occurs at the Palladium surface:

$$4\,OH^- \longrightarrow O_2 + H_2O + 4\,e^- \tag{3.18}$$

For applied potentials below the lower dotted line, water is reduced (Hydrogen evolution reaction). In the alkaline environment, the following reactions occurs at the Palladium surface:

$$2\,H_2O + 2\,e^- \longrightarrow H_2(g) + OH^- \tag{3.19}$$

To sum up, the analysis of the Pourbaix diagram confirms what had been already observed with the cyclic voltammogram. In order to avoid any unwanted side reaction (oxygen evolution) and passivation of the Palladium surface (formation of thick impermeable PdO_2 layer) the maximum potential that should be applied to the system is 0.2 V vs Ag/AgCl.

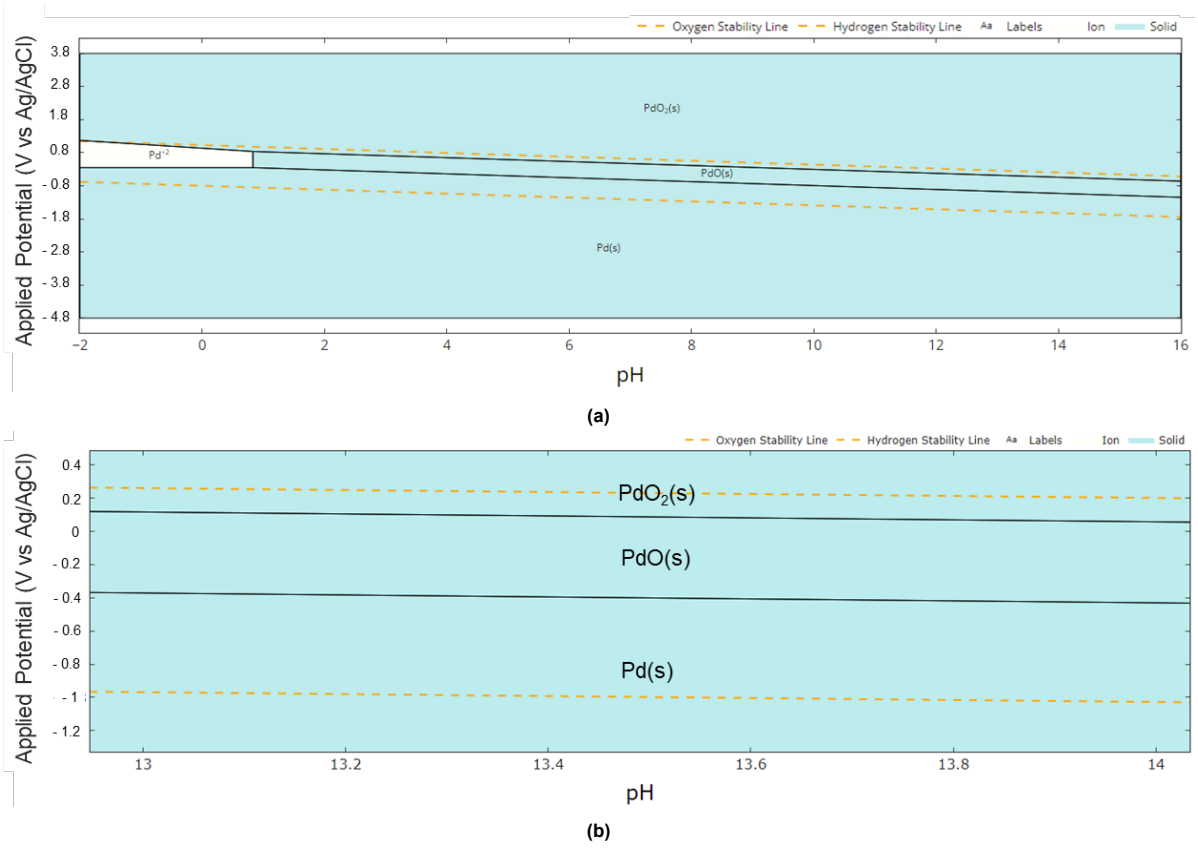

Figure 3.6: (a) Pourbaix Diagram for Palladium and (b) Zoom into the region of interest for the detection side

Effect of Anodic Potential on Permeation Transient

Considering the previous analyses, the effect of the applied anodic potential on the hydrogen permeation behavior of HDPE was investigated to determine the optimal potential for obtaining a representative permeation curve. The goal was to identify the best anodic potential for hydrogen oxidation at the detection side, ensuring a reliable measurement of hydrogen permeation through the polymer.

Based on findings from the literature (Table B.2), the decision was made to begin by applying a slight anodic overpotential relative to the open circuit potential (OCP) of the system. The OCP was measured to be -50 mV vs Ag/AgCl. In Figure 3.7a, the permeation transient is shown for an overpotential of 50 mV above the OCP. It is evident that no significant increase in current occurs, indicating that the applied anodic potential is insufficient to drive the hydrogen oxidation reaction effectively. The observed noise in the data suggests that hydrogen bubbles are forming on the palladium surface at the detection side. This occurs because the Tafel recombination reaction, where hydrogen atoms recombine to form molecular hydrogen (H_2), is predominant at this potential.

The situation improves when an overpotential of 150 mV is applied, as shown in Figure 3.7b. Here, the increase in current indicates that hydrogen oxidation is starting to occur. However, Tafel recombination remains the predominant reaction, leading to an accumulation of hydrogen on the exit side. This results in an initial rise in the transient, followed by a decay due to the hydrogen concentration build-up on the exit side.

Finally, with an applied potential of 0.2 V vs Ag/AgCl (an overpotential of 250 mV), a stable permeation transient is observed (Figure 3.7c). The current remains steady throughout the experiment, indicating that the hydrogen oxidation reaction is consistently favored. While some hydrogen bubbles due to Tafel recombination are still present, further increasing the potential is not feasible. Any higher potential would lead to the formation of a thick, impermeable PdO_2 layer, which would block hydrogen transport. Also, oxygen evolution on the palladium surface would eventually be initiated, as demonstrated by the cyclic voltammetry (CV) and Pourbaix diagram studies.

For these reasons, an anodic potential of 0.2 V vs Ag/AgCl was selected as the optimal condition for the electrochemical hydrogen permeation experiments on all polymer samples.

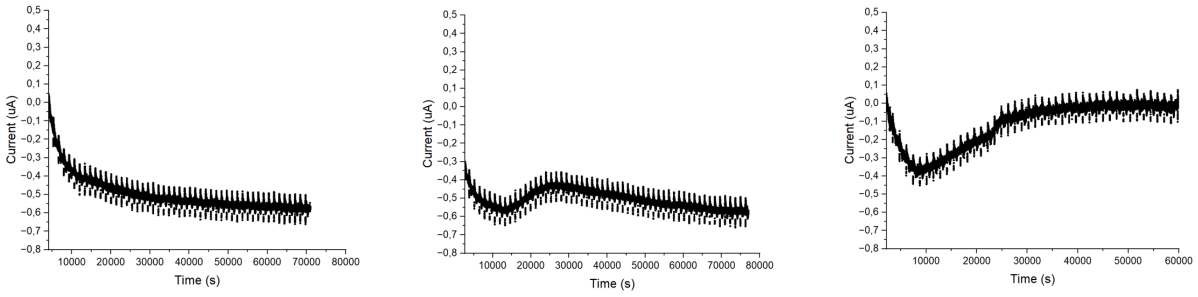

(a) Applied Potential E = 0 V vs Ag/AgCl **(b)** Applied Potential E = 0.1 V vs Ag/AgCl **(c)** Applied Potential E = 0.2 V vs Ag/AgCl

Figure 3.7: Hydrogen permeation transient for HDPE at different applied potentials

3.1.4. Selection of Charging Side Electrolyte and Current

The initial selection of the applied cathodic current and electrolyte on the charging side was informed by a review of relevant literature (see Table B.3 in Appendix B). A key challenge, however, was that unlike the detection side, in typical Devanathan-Stachurski experiments with metals, the charging side is not coated with palladium. Hydrogen is evolved directly on the bare metal surface. This introduced an additional consideration, as the choice of charging conditions and electrolyte is affected by the presence of different metal species at the charging electrode.

Most Devanathan-Stachurski experiments are performed on iron or steel, where NaOH is often selected as the electrolyte to avoid the corrosive effects of H_2SO_4 on iron. However, it has been reported that using H_2SO_4 on the charging side can lead to higher hydrogen permeation at the input surface, resulting in a stronger signal at the exit side. The reason for this is that the presence of H^+ ions in the acidic solution enhances the kinetics of the hydrogen evolution reaction (HER) [30]. A comparison of permeation transients using acid versus alkaline electrolytes on the charging side is shown in Figure 3.8.

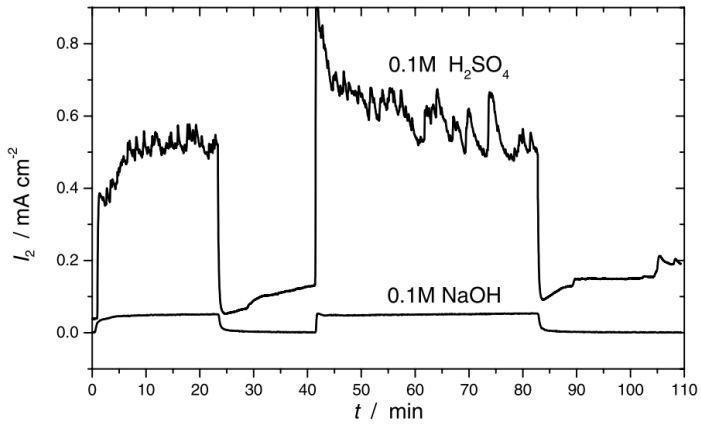

Figure 3.8: Permeation transient obtained with either a 0.1 M H_2SO_4 or a 0.1 M NaOH solution on the input cell. Membrane material: Iron. Charging current: 10 mA/cm^2. The noise in the acid electrolyte permeation transient is due to the corrosive effect of H_2SO_4 on the bare metal surface

Given that the working electrode in the Devanathan-Stachurski setup for this project is palladium, a much more noble metal that is resistant to acid corrosion, a 0.05 M H_2SO_4 solution was chosen for the charging side. Unfortunately, there is no comprehensive study in the literature investigating the effect of different acid concentrations on the permeation transient in the Devanathan-Stachurski setup. It was therefore assumed that, similar to the detection side, the electrolyte concentration would have a negligible effect compared to the applied cathodic current, which drives the hydrogen evolution reaction.

Initially, a cathodic current of -5 mA/cm^2 was selected based on the literature review. While this current was sufficient to produce permeation transients for the PEEK samples, it was later reduced to -0.5 mA/cm^2 after the failure of tests on the HDPE samples. The reasoning behind this adjustment and the steps taken are detailed in the following paragraphs.

The extent of the damage caused by the initial charging current is shown in Figure 3.9. While the coating on PEEK exhibited minimal damage (Figure 3.9a), the palladium coating on the HDPE surface completely peeled off (Figure 3.9b). This discrepancy is attributed to the differences in surface adhesion between the two polymers. Untreated PEEK has a higher surface energy compared to HDPE, which allows the palladium coating to adhere much more easily to the PEEK surface before any treatment is applied.

(a) PEEK, area exposed to electrolyte is circled in white **(b)** HDPE

Figure 3.9: Extend of damage to the entry side Palladium coating on PEEK and HDPE samples

The peeling or damage of the palladium coating is primarily caused by hydrogen absorption in palladium. As discussed in Section 1.3.2 of Chapter 1, when palladium absorbs hydrogen, it undergoes a phase transition to the β-phase, characterized by an increased lattice parameter. This swelling creates internal stress in the coating. This swelling creates internal stress in the coating. Additionally, as palladium absorbs hydrogen, hydrogen embrittlement occurs, which further degrades the metal, causing it to crack and peel off the surface.

The first solution explored to mitigate this issue was to enhance the surface adhesion of the coating through corona arc treatment. This surface treatment involves applying a high voltage (typically in the range of 10-20 kV) between an electrode and a grounded surface (or another electrode). The high voltage creates an electric field that ionizes the surrounding air or gas, forming a corona discharge. The corona discharge breaks down the molecules in the surrounding air, creating reactive species such as ozone (O_3), atomic oxygen (O), nitrogen oxides (NOx), and various free radicals. These reactive species are highly energetic and can interact with the polymer chains at the surface, breaking them up and introducing polar oxygen- or nitrogen-containing groups [63].

Following the treatment, the increase in surface energy of the polymers was confirmed by measuring the change in water contact angles. In both PEEK and HDPE, the water contact angle was nearly halved, indicating a significant improvement in surface wettability. The results are shown in Figures A.6 and A.7 in Appendix A. While this treatment improved the palladium coating's resistance to peeling during hydrogen charging, some issues still persisted.

Figure 3.10 shows the permeation transient of a PEEK sample treated with corona arc discharge, using a charging current of -5 mA/cm^2. As indicated by the blue rectangle, the permeation transient exhibits a decay after initially stabilizing. A study on hydrogen absorption in pure palladium membranes suggests that at cathodic charging currents above 2 mA/cm^2, the Tafel and Heyrovsky recombination reactions become so fast that they significantly reduce the amount of hydrogen absorbed into the palladium [29]. Another study [54] recommends applying a lower cathodic current (around 0.05 mA/cm^2) to prevent saturation of the palladium membrane. Based on this study, the following explanation for the decay in the transient curve was proposed: when the charging current is too high, not all of the permeating hydrogen can be oxidized at the exit side, due to the limited overpotential applied at the detection side (as discussed in the previous section). As a result, hydrogen accumulates at the exit side, causing the palladium coating to become saturated. This leads to a buildup of hydrogen at the exit side and a subsequent decrease in the concentration gradient, which is the primary driving force behind the permeation process. The reduction in concentration gradient is what causes the observed decay in the rising transient, as illustrated in Figure 3.11.

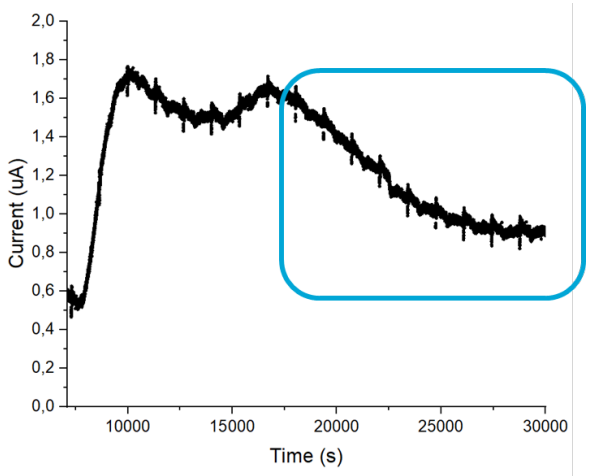

Figure 3.10: Permeation transient on PEEK sample after corona arc surface treatment - decay of the permeation curve. Charging current: - 5 mA/cm^2

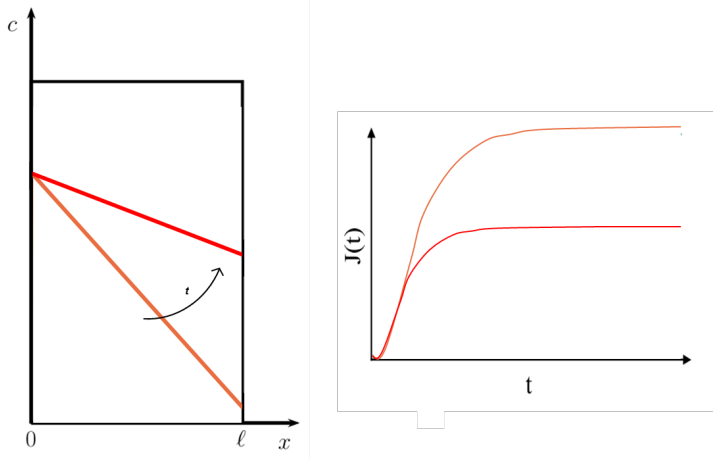

Figure 3.11: Effect of hydrogen accumulation on the exit side: Left - concentration gradient decreases over time (orange to red). Right - Effect of a lower concentration gradient on the permeation transient.

To address this, permeation tests were conducted with cathodic currents starting from 0.1 mA, increasing by 0.1 mA increments. A stable and reproducible hydrogen permeation signal was not achieved until a current of 0.5 mA was applied. This current was considered optimal, as it allowed sufficient hydrogen evolution at the surface of the palladium coating while also enabling the absorbed hydrogen to diffuse away from the input side and be oxidized, thus avoiding saturation of the palladium coating.

As a result, a cathodic current of 0.5 mA was selected as the optimal value for the charging side. However, it is possible that higher currents (up to approximately 3.5 mA, according to [29]) could also yield reproducible results across all polymer samples.

3.1.5. Obtaining Quantifiable Data from Experiments: Calculations for P and D

Once the testing protocol is established, the next step is to extract the necessary information from the resulting permeation curves. As outlined in chapter 1, diffusion through polymers is characterized by three primary parameters: solubility (S), diffusivity (D), and permeability (P). According to equation 1.10, these parameters are interdependent, and thus this study focuses on evaluating diffusivity (D) and permeability (P) for each polymer sample; the third parameter (S) can then be derived.

Diffusivity (D), expressed in $\frac{cm^2}{s}$, indicates the speed at which hydrogen molecules move through the polymer in response to a concentration (or pressure) gradient. Permeability (P), expressed in $\frac{mol}{cm \cdot s}$, reflects the overall transport rate of H_2 through the polymer, representing the polymer's total hydrogen uptake.

To illustrate the practical implications of diffusivity and permeability, consider a metal hydrogen storage tank with an internal polymer liner. This liner is intended to prevent (or at least delay) embrittlement caused by permeating hydrogen, as well as reduce the amount of hydrogen that will be lost to the environment. A polymer with high diffusivity will result in faster mechanical failure of the tank because hydrogen molecules permeate the liner and reach the metal walls sooner. This accelerates embrittlement within the metal lattice. Meanwhile, permeability represents the total quantity of H_2 that will leak from the liner and reaching the metal walls under operating conditions.

To extrapolate D and P values from the experimental curves for each polymer sample, it is essential first to set up the boundary conditions and equations describing the diffusion process. In our setup, the hydrogen gas pressure is 1 atm, and the temperature is well above hydrogen's liquefaction point (-252.86 °C at standard pressure). Under these conditions, we can assume (1) no specific interactions among hydrogen molecules and (2) no strong interactions between hydrogen molecules and polymer chains, therefore sorption is governed by Henry's law (uniform dispersion of sorbed penetrant molcules within the polymer), and diffusion is governed by Fick's laws (D is independent of the sorbed penetrant's

concentration) [85].

Under these assumptions, the diffusion of hydrogen through the polymer sample during electrochemical permeation testing is governed by the following equations and boundary conditions:

$$\frac{\partial c(x,t)}{\partial t} = D\frac{\partial^2 c(x,t)}{\partial x^2} \quad \text{Fick's Second Law} \tag{3.20}$$

$$c(x,t) = 0 \quad \text{for} \quad 0 \leq x \leq L \quad \text{for} \quad t < 0 \tag{3.21}$$

$$c(x,t) = c \quad \text{for} \quad x = 0 \quad \text{for} \quad t \geq 0 \tag{3.22}$$

$$c(x,t) = 0 \quad \text{for} \quad x = L \quad \text{for} \quad t \geq 0 \tag{3.23}$$

Here, $c(x,t)$ represents the concentration of H_2 at position x along the sample thickness at time t. A visual representation of these boundary conditions is provided in figure 3.12/

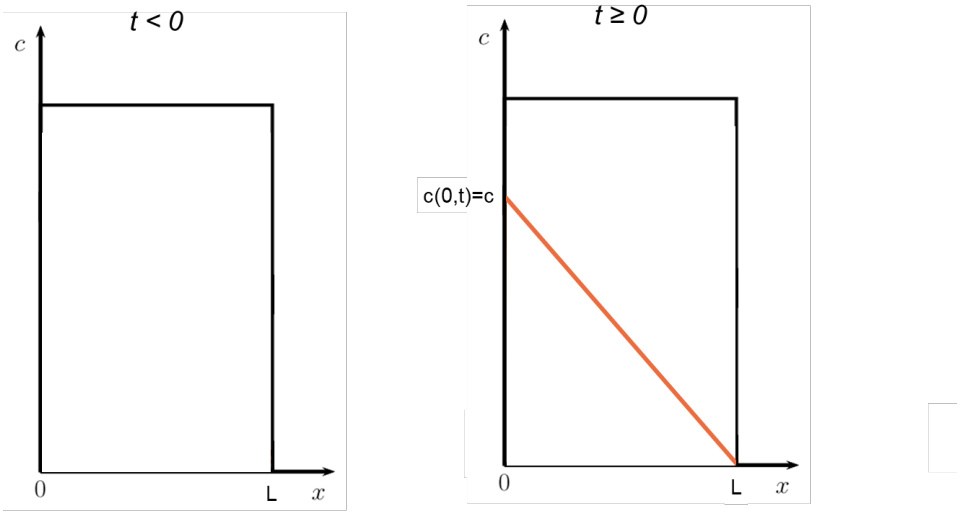

Figure 3.12: Visual representation of boundary conditions

In 1961, Bockris and Devanathan [12] introduced two graphical methods to determine diffusivity (D) from a current-vs-time curve based on Fick's law. The first method estimates D from the breakthrough time t_b, yielding a diffusivity value, D_{t_b}. The second method uses time lag t_L extrapolation to provide a diffusivity value, D_{t_L}. This D_{t_L} approach is widely used in techniques like TDA and HPHP to calculate D (see 1.2.1 and 1.2.2).

While Bockris and Devanathan's approach provided a method for calculating diffusivity, it did not include a way to determine hydrogen permeability (P) in electrochemical testing. This gap was addressed by Fan et al. [23] and later by Sethuraman et al. [73]. They introduced a solution for boundary conditions and Fick's laws specific to electrochemical testing, providing an equation for $i(t)$ containing both diffusivity D and solubility c (referred to from here on as D_s and c_s). By fitting this equation to their experimental data, they obtained all necessary parameters..
Moreover, they included an equation for permeability based on the steady-state current, that is demonstrated in section C.1.3 of Appendix C).

To evaluate the validity and significance of these methods, we applied all of them to calculate P and D for each polymer sample:

- For diffusivity, three values were calculated: D_{t_b}, D_{t_L}, and the diffusivity from Sethuraman's equation, D_s.
- For permeability, two values were obtained: one by extrapolating i_∞ and applying equation C.20, and the other by multiplying D_s and c_s from Sethuraman's equation.

The next section presents examples to demonstrate the calculation of these three diffusivity and two permeability values.

For details on the derivations of D_{t_b}, D_{t_L}, P, and Sethuraman's solution, refer to Appendix C.

Breakthrough Time Method

As the name suggests, the breakthrough time is defined as the time it takes a detectable amount of hydrogen to diffuse through the thickness of the polymer sample, as can be visualized in figure 3.13.

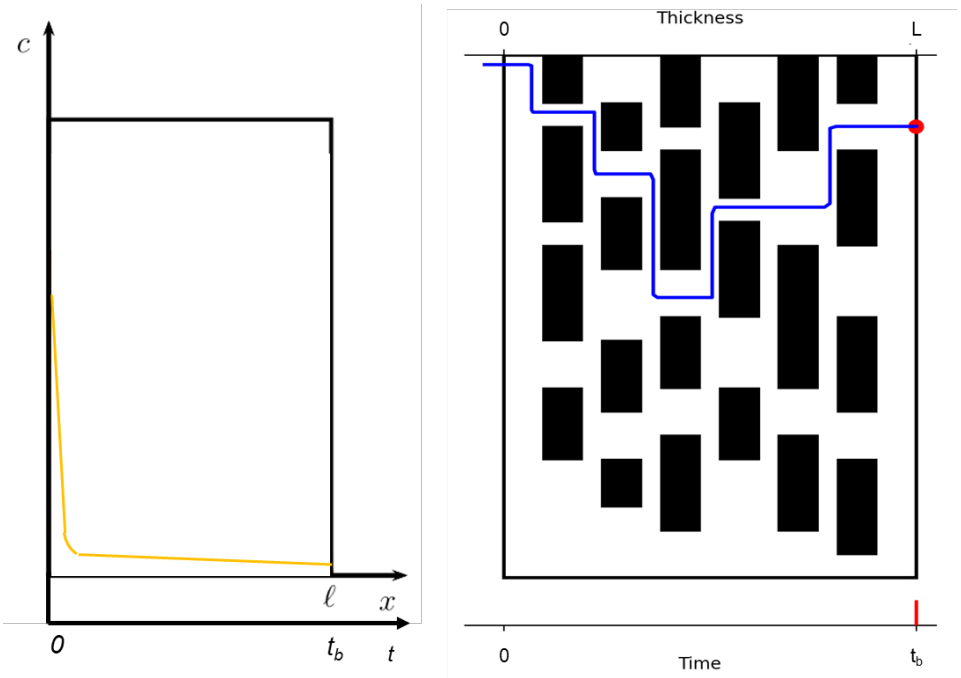

Figure 3.13: Left: Concentration gradient established at the start of the test.
Right: Visualization of the breakthrough time. The black patches represent the crystalline regions through which the hydrogen molecule (red) cannot diffuse

According to Boes et al. [13], the breakthrough time is determined by extending the tangent at the inflection point of the permeation curve until it intersects the time axis. Once the value of t_b has been established, the diffusivity D_{t_b} can be calculated as reported by Bockris and Devanathan [12]:

$$D_{t_b} = \frac{L^2}{15.3 \cdot t_b} \tag{3.24}$$

Figure 3.14 illustrates an example of breakthrough time calculation from a permeation transient obtained using the setup in this project. A sigmoid curve was fitted to the experimental data, allowing for the identification of the inflection point and, consequently, the breakthrough time.

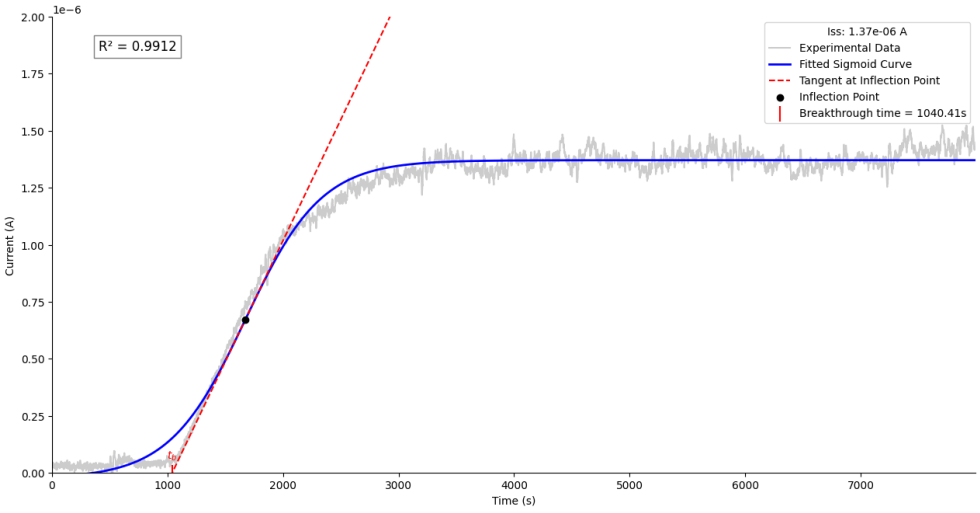

Figure 3.14: Example of the evaluation of t_b from experimental data

Time Lag Method

The time lag method, widely used in literature to determine diffusivity, has been previously discussed in the context of high-pressure permeation test methods and TDA (see section 1.2.2). The time lag represents the period required to establish a steady-state concentration gradient across the sample following a sudden change in boundary conditions at the input side [13]. To help the understanding of the time lag, the evolution of the concentration gradient over time, from 0 to t_b and up to t_L, is illustrated in Figure 3.15.

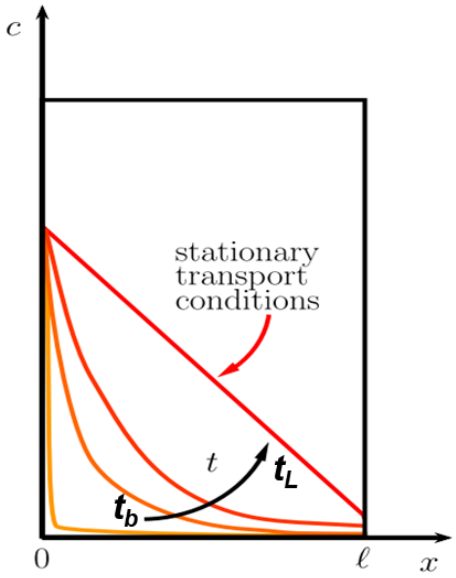

Figure 3.15: Establishment of the steady state concentration gradient throughout the sample's thickness in the Devanathan Stachurski experiment

The establishment of a steady-state concentration gradient implies that the concentration at every point

throughout the sample thickness remains constant over time (illustrated by the red line in Figure 3.15). At this stage, the quantity of oxidized hydrogen will increase linearly with time.

When examining the permeation transient (hydrogen flux vs. time), the area under the curve represents the total oxidized hydrogen. Once the steady-state concentration gradient is achieved, the slope of the integral of the permeation transient becomes constant. The time lag, t_L, can then be determined as the intercept of the linear portion of the integral with the time axis (see Figure 3.16).

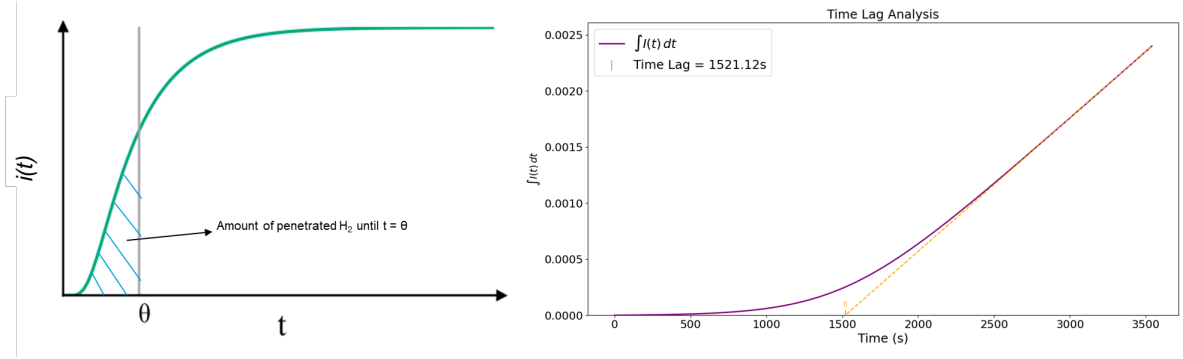

Figure 3.16: Left: evaluation of total amount of oxidated H_2 from the flux (current) vs time curve. Right: calculation of the time lag from the integral of the flux (current) vs time curve.

The diffusivity D_{t_L} can be calculated as follows, in accordance with [12]:

$$D_{t_L} = \frac{L^2}{6 \cdot t_L} \tag{3.25}$$

Permeability: Calculation from i_∞

As demonstrated in section C.1.3 of appendix C, the permeability can be evaluated from the steady state current i_∞. The current is obtained by determining the plateau value of the sigmoid curve fit to the experimental data, as shown below in figure 3.17.

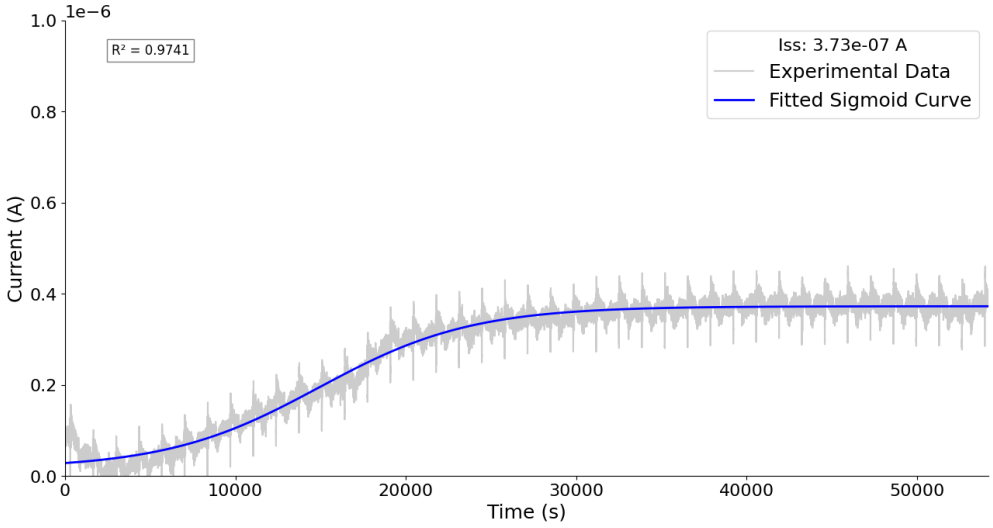

Figure 3.17: Evaluation of the steady state current i_∞ from the experimental data

From i_∞ the permeability can be evaluated from equation C.20:

$$P = \frac{i_\infty L}{2FA} \tag{3.26}$$

where:

- L is the thickness of the sample
- A is the area exposed to the electrolyte (permeation area)

Diffusivity and Permeability: Fitting Sethuraman's Solution to the Data

The solution of Fick's laws and boundary condition from Fan and Sethuraman [23, 73] is reported in appendix C. The equation, which includes the terms of solubility and diffusivity (c_s and D_s), was fitted to the experimental data, so that the unknown parameters c_s and D_s could be found. From these, the permeability follows in accordance with equation 1.10. An example of the fitting process is shown in figure 3.18 below.

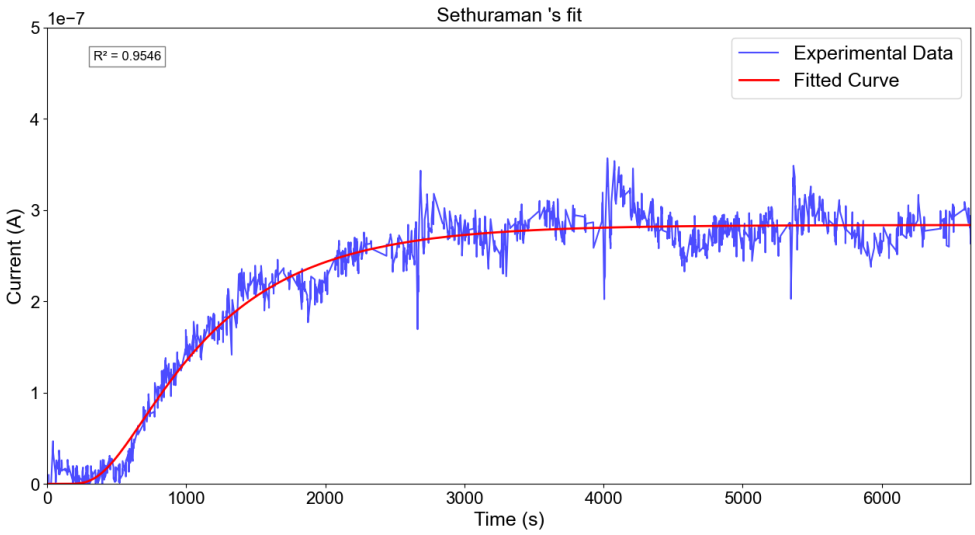

Figure 3.18: Experimental data and fit of Sethuraman's equation for $i(t)$

3.2. Experimental Data

The next three sections will be structured in the following way: for each material, two representative figures will be shown. The first will contain the experimental data, the fitted sigmoid curve, the integral of the sigmoid and the graphical extrapolation of the t_b and t_L. The second one will display the experimental data and the fitted curve acccording to Sethuraman's solution. Then, a table that summarizes all relevant data will be displayed. Finally, bar graphs comparing the three different diffusivity values with literature as well as the two different permeability values with literature will be displayed. All the permeation curves that are reported in the tables below are displayes in appendix D.

3.2.1. Polyether Ether Ketone

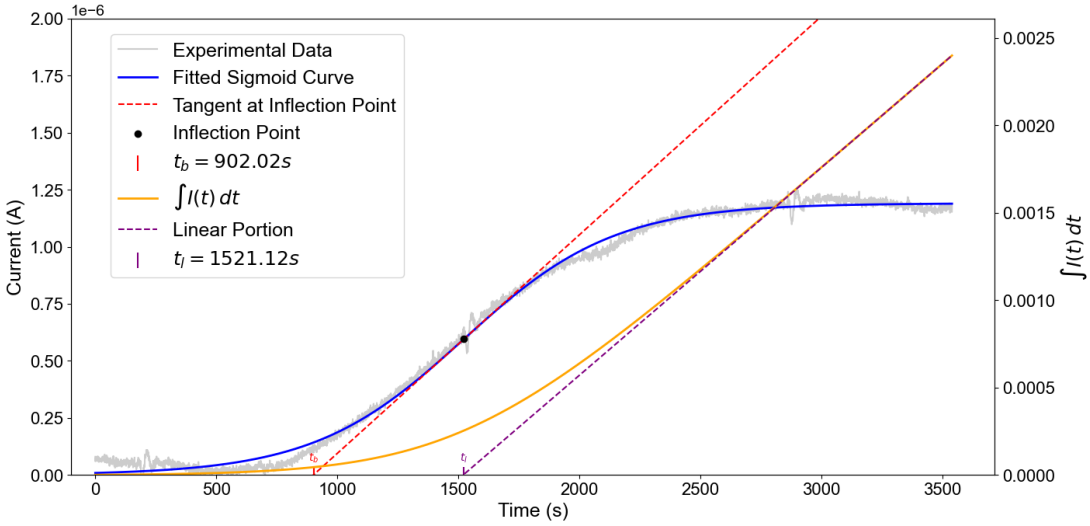

(a) Breakthrough time and time lag

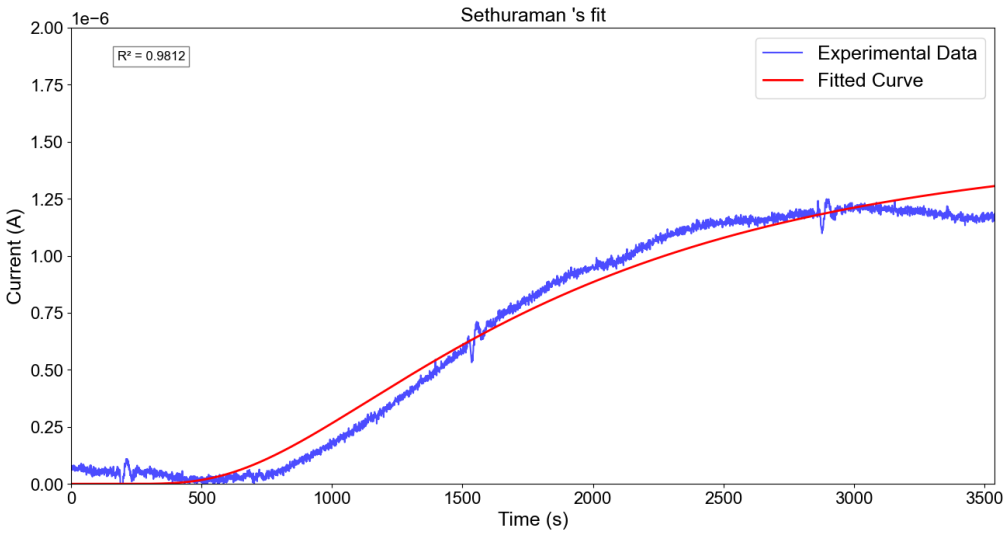

(b) Sethuraman's curve fit

Figure 3.19: Example experimental data for PEEK

Table 3.1: Diffusivity values for PEEK from tests and literature.

Test	Cristallinity of tested samples: 34 % (DSC measurement)			
	D_{t_b} **(**cm^2/s**)**	D_{t_L} **(**cm^2/s**)**	D_s **(**cm^2/s**)**	
#1	6.82E-08	1.25E-07	-	
#2	1.70E-07	2.57E-07	1.89E-07	
#3	8.91E-08	1.98E-07	1.23E-07	
#4	4.18E-08	9.12E-08	-	
#5	1.21E-07	2.43E-07	1.55E-07	
#6-1	1.09E-07	2.20E-07	-	
#6-2	4.63E-07	4.20E-07	3.48E-07	
#7-1	2.89E-07	1.34E-07	1.19E-07	
#7-2	3.93E-07	3.58E-07	3.37E-07	
Literature	**HPHP Test -** $D_{t_L}(cm^2/s)$			**Reference**
15% C (DSC)	5.32E-07			[59]
30% C #1 (DSC)	2.96E-07			[59]
30% C #2 (DSC)	5.16E-07			[59]
38% C (DSC)	2.42E-07			[59]

Table 3.2: Permeability values for PEEK from tests and literature

Test	Cristallinity of tested samples: 34 % (DSC measurement)		
	P (mol/(cm s))		
	Sigmoid fit	**Sethuraman's fit**	
#1	1.18E-12	-	
#2	3.38E-13	4.20E-13	
#3	1.19E-13	1.63E-13	
#4	1.03E-12	-	
#5	2.06E-13	2.98E-13	
#6-1	5.42E-14	-	
#6-2	9.40E-14	1.02E-13	
#7-1	6.24E-14	6.38E-14	
#7-2	1.04E-13	1.05E-13	
Literature	**HPHP Test - P (mol/(cm s))**		**Reference**
15% C (DSC)	1.22E-12		[59]
30% C #1 (DSC)	6.14E-13		[59]
30% C #2 (DSC)	6.82E-13		[59]
38% C (DSC)	3.94E-13		[59]

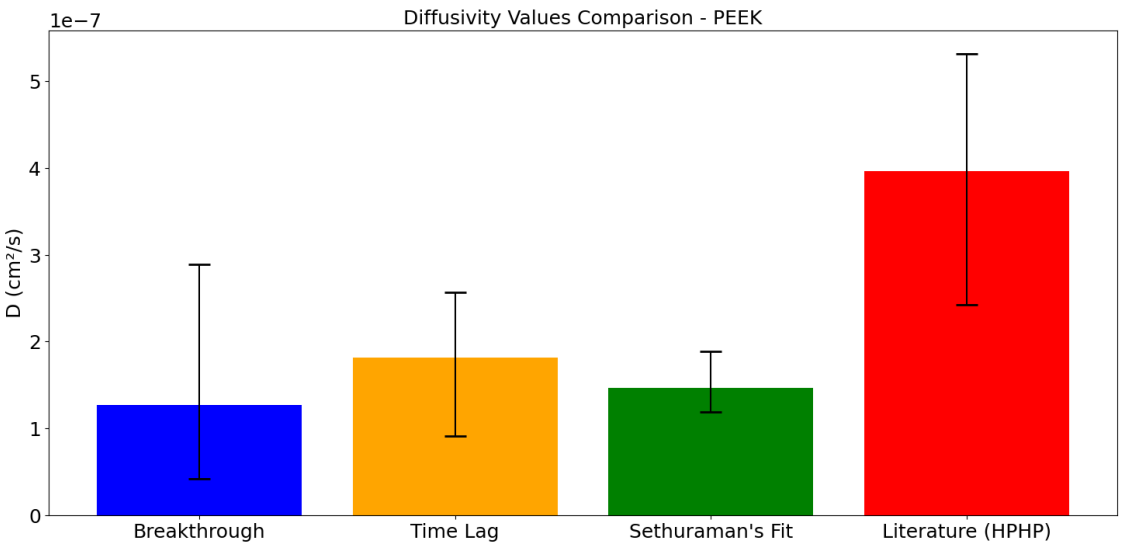

(a) Diffusivity values

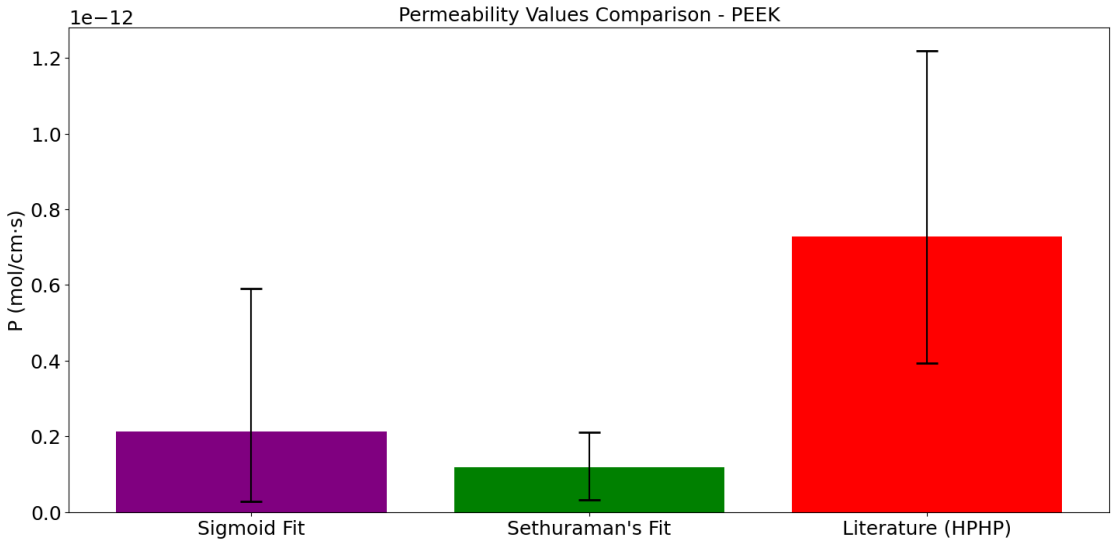

(b) Permeability values

Figure 3.20: Comparison between Diffusivity and Permeability values obtained through different methods

3.2.2. High Density Polyethylene

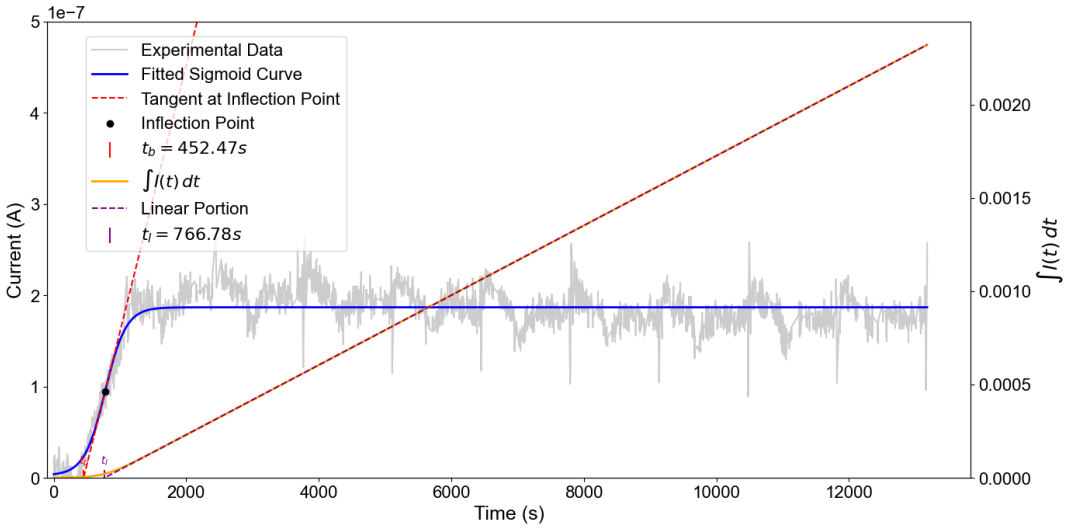

(a) Breakthrough time and time lag

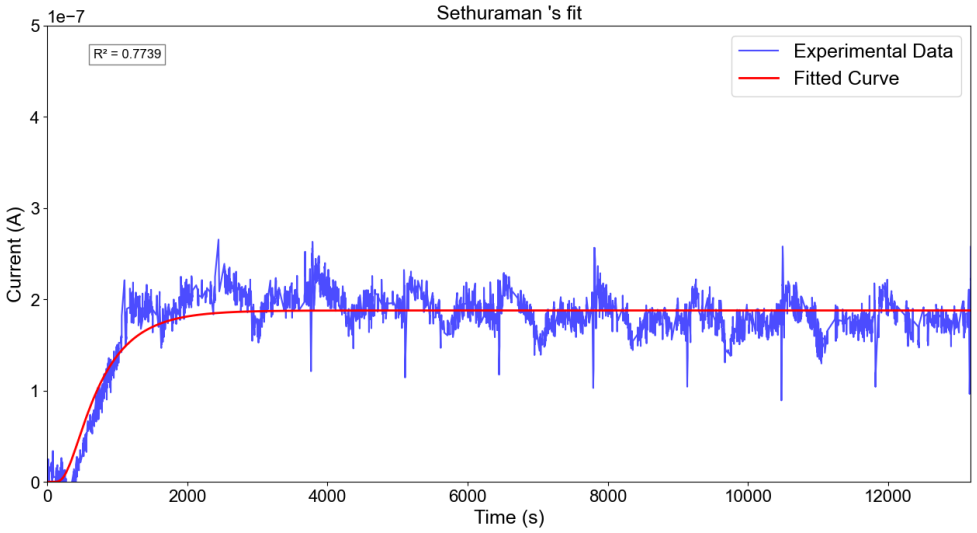

(b) Sethuraman's curve fit

Figure 3.21: Example experimental data for HDPE

Table 3.3: Diffusivity values for HDPE from tests and literature

Test	Cristallinity: 54 % (DSC measurement) or 78 % (density measurement)			
	D_{t_b} **(**cm^2/s**)**	D_{t_L} **(**cm^2/s**)**	D_s **(**cm^2/s**)**	
#1	1.88E-07	1.92E-07	1.50E-07	
#2-1	9.95E-07	1.50E-06	1.41E-06	
#2-2	1.78E-06	9.54E-07	9.19E-07	
#2-3	2.04E-06	8.90E-07	8.49E-07	
Literature	**HPHP Test -** D_{t_L} **(**cm^2/s**)**			**Reference**
92% C (density)	3.30E-08			[35]
78% C (density)	1.35E-06			[27]
80% C (density)	-			[27]
58% C (DSC)	2.20E-06			[93]
54% C (DSC)	1.96E-06			[93]
57% C (DSC)	1.54E-06			[93]
61% C (DSC)	1.30E-06			[93]
-	1.90E-06			[93]
Literature	**TDA - fitting to diffusion equation**			
78% C (density)	2.09E-06			[28]
80% C (density)	2.11E-06			[28]

Table 3.4: Permeability values for HDPE from tests and literature

Test	Cristallinity: 54 % (DSC measurement) or 78 % (density measurement)		
	P (mol/(cm s))		
	Sigmoid fit	**Sethuraman's fit**	
#1	2.66E-13	2.78E-13	
#2-1	1.11E-13	9.14E-14	
#2-2	1.36E-13	1.38E-13	
#2-3	1.61E-13	1.61E-13	
Literature	**HPHP Test - P (mol/(cm s))**		**Reference**
92% C (density)	-		[35]
78% C (density)	9.25E-11		[27]
80% C (density)	-		[27]
58% C (DSC)	6.85E-13		[93]
54% C (DSC)	7.89E-13		[93]
57% C (DSC)	6.85E-13		[93]
61% C (DSC)	5.95E-13		[93]
-	8.93E-13		[40]

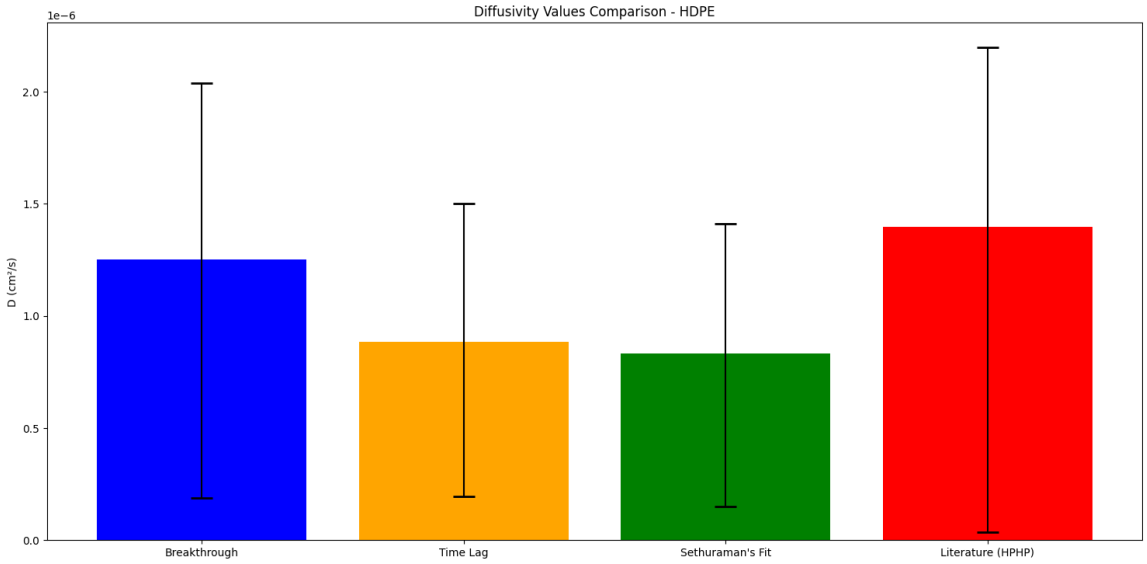

(a) Diffusivity values

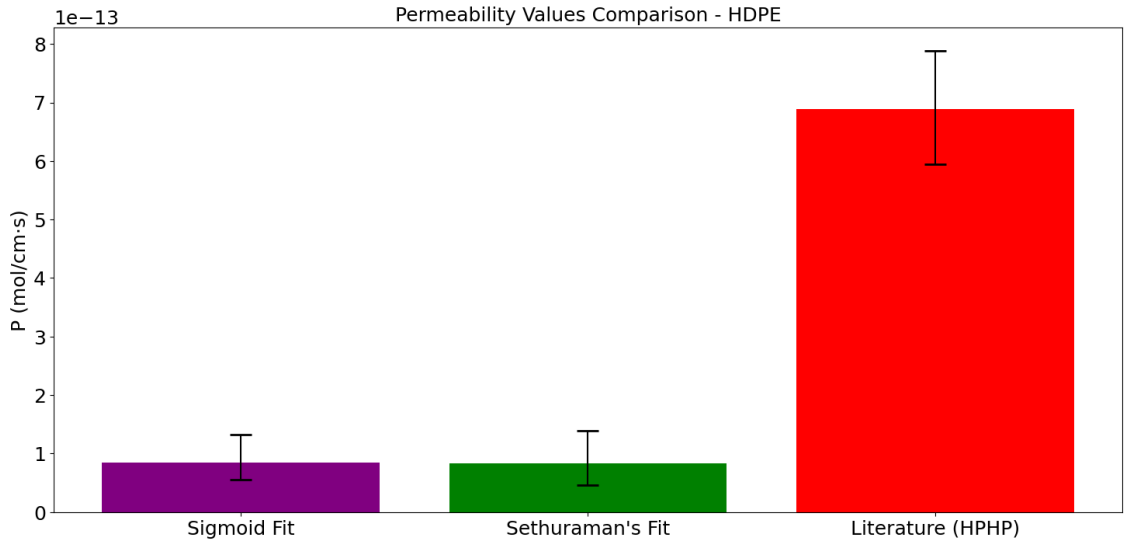

(b) Permeability values

Figure 3.22: Comparison between Diffusivity and Permeability values obtained through different methods

3.2.3. Polypropylene

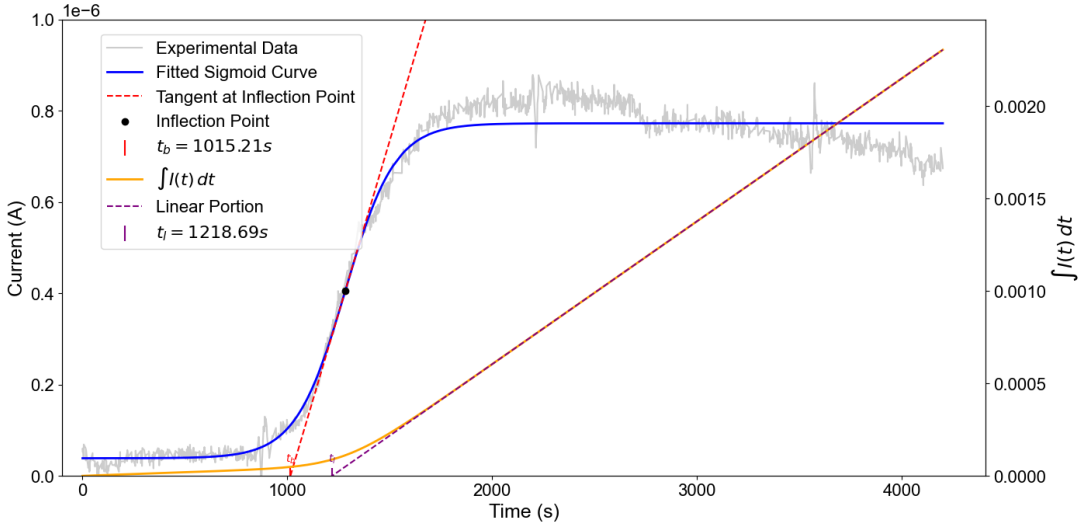

(a) Breakthrough time and time lag

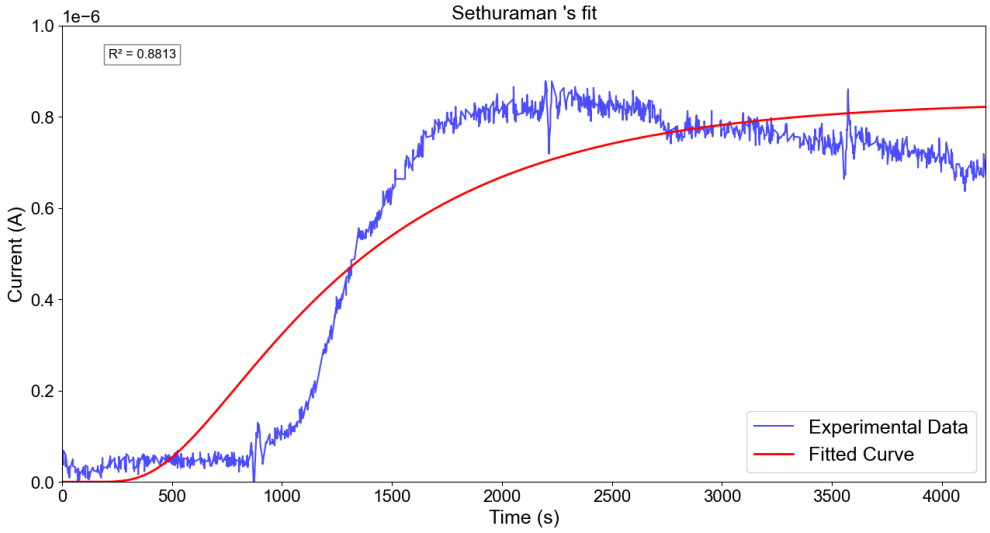

(b) Sethuraman's curve fit

Figure 3.23: Example experimental data for PP

Table 3.5: Diffusivity values for PP from tests and literature

Test	Sample Cristallinity: 39 % (DSC) or 65 % (density)			
	D_{t_b} **(**cm^2/s**)**	D_{t_L} **(**cm^2/s**)**	**Sethuraman's fit (**cm^2/s**)**	
#1	3.72E-07	5.81E-07	-	
#2-1	3.19E-07	7.49E-07	6.42E-07	
#2-2	2.70E-06	2.45E-06	2.30E-06	
#3-1	3.72E-07	7.90E-07	6.74E-07	
#3-2	4.59E-06	1.72E-06	-	
#4-1	3.36E-07	6.05E-07	-	
#4-2	4.82E-06	2.10E-06	2.00E-06	
#4-3	2.22E-06	3.47E-06	-	
Literature	**HPHP Test -** D_{t_L} **(**cm^2/s**)**			**Reference**
Amorphous	6.60E-06			[42]
Crystalline	3.00E-06			[42]
60% C (DSC)	3.70E-07			[60]
50% C (DSC)	-			[50]

Table 3.6: Permeability values for PP from tests and literature

Test	Sample Cristallinity: 39 % (DSC) or 65 % (density)		
	P (mol/(cm s))		
	Sigmoid fit	**Sethuraman's fit**	
#1	6.20E-13	-	
#2-1	4.20E-13	4.60E-13	
#2-2	2.38E-13	2.44E-13	
#3-1	3.44E-13	3.72E-13	
#3-2	3.18E-13	-	
#4-1	1.65E-13	-	
#4-2	1.57E-13	1.57E-13	
#4-3	7.94E-14	-	
Literature	**HPHP Test - P (mol/(cm s))**		**Reference**
Amorphous	1.83E-12		[42]
Crystalline	6.25E-13		[42]
60% C (DSC)	2.86E-12		[60]
50% C (DSC)	2.03E-12		[50]

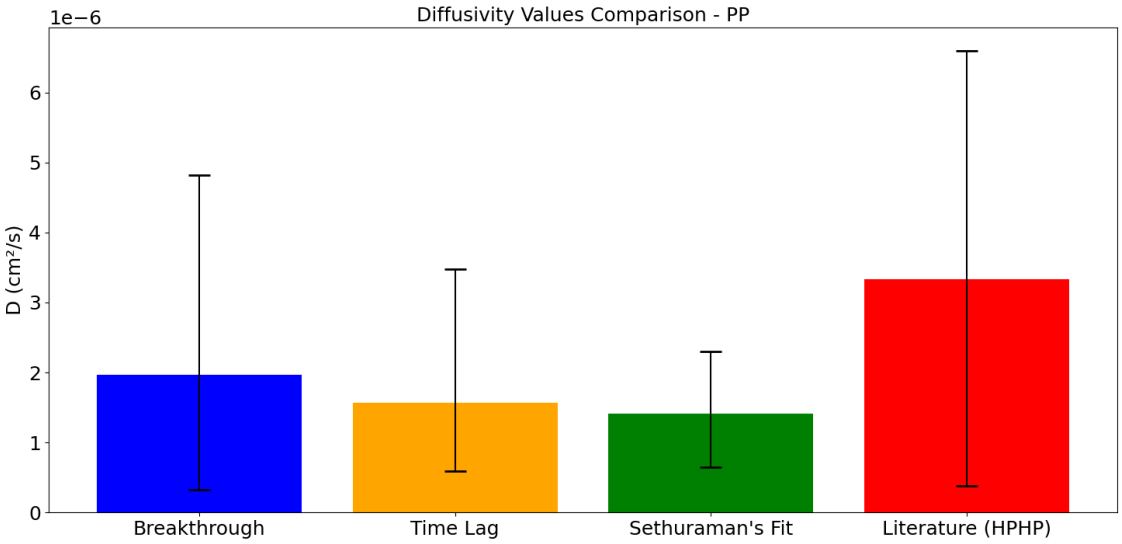

(a) Diffusivity values

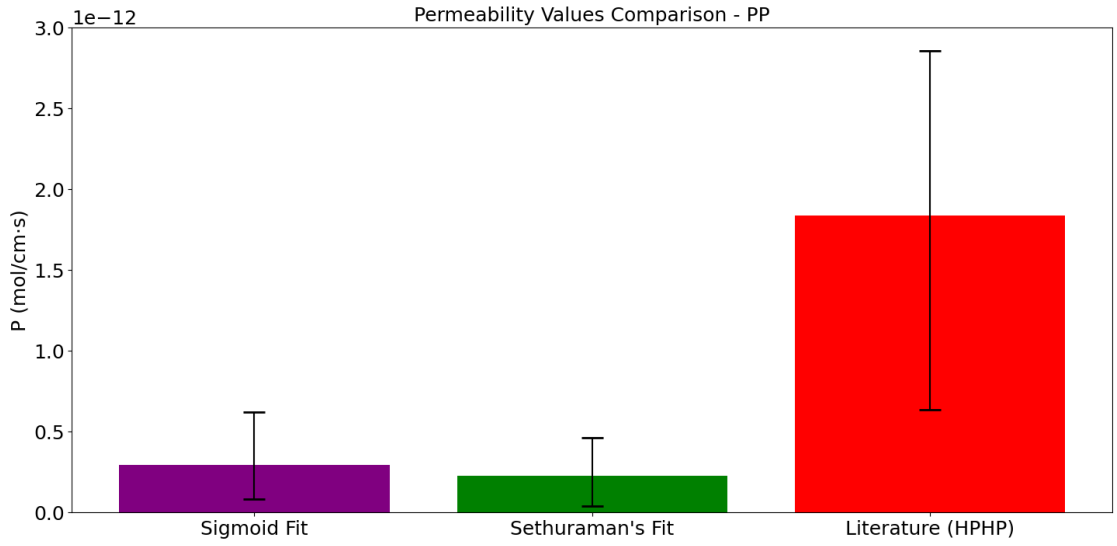

(b) Permeability values

Figure 3.24: Comparison between Diffusivity and Permeability values obtained through different methods

3.2.4. Comparison Between Samples

This section aims to compare the permeation parameters (diffusivity, solubility, and permeability) for the three polymer samples based on their material properties. The parameters calculated through the three different methods are illustrated in figures 3.25, 3.26 and 3.27. Further details on the definitions and interpretations of the various diffusivity and permeability values are available in Section 3.1.5. The three solubility values (denoted as C) are calculated using Equation 1.10 and defined as follows:

- C_{t_b} (Breakthrough): Calculated by dividing the permeability value obtained from the sigmoid curve fit by D_{t_b}.
- C_{t_L} (Time Lag): Derived by dividing the permeability value from the sigmoid fit by D_{t_L}.
- C_S (Sethuraman's Fit): Determined by fitting Sethuraman's solution to the experimental data, which allows extraction of diffusion parameters.

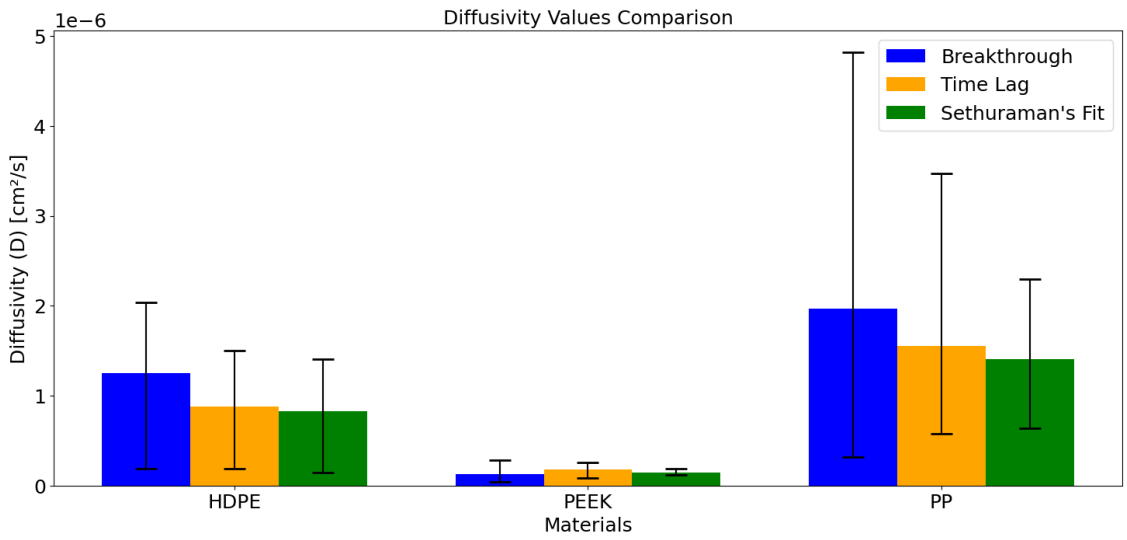

Figure 3.25: Comparison between Diffusivity values calculated with the three methods for the tested polymer samples

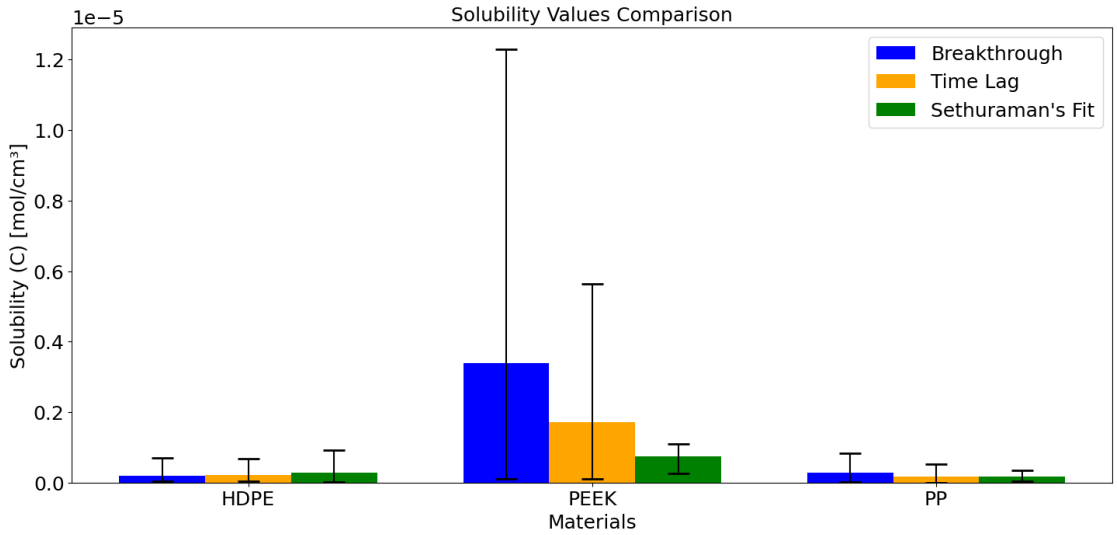

Figure 3.26: Comparison between Solubility values calculated with the three methods for the tested polymer samples

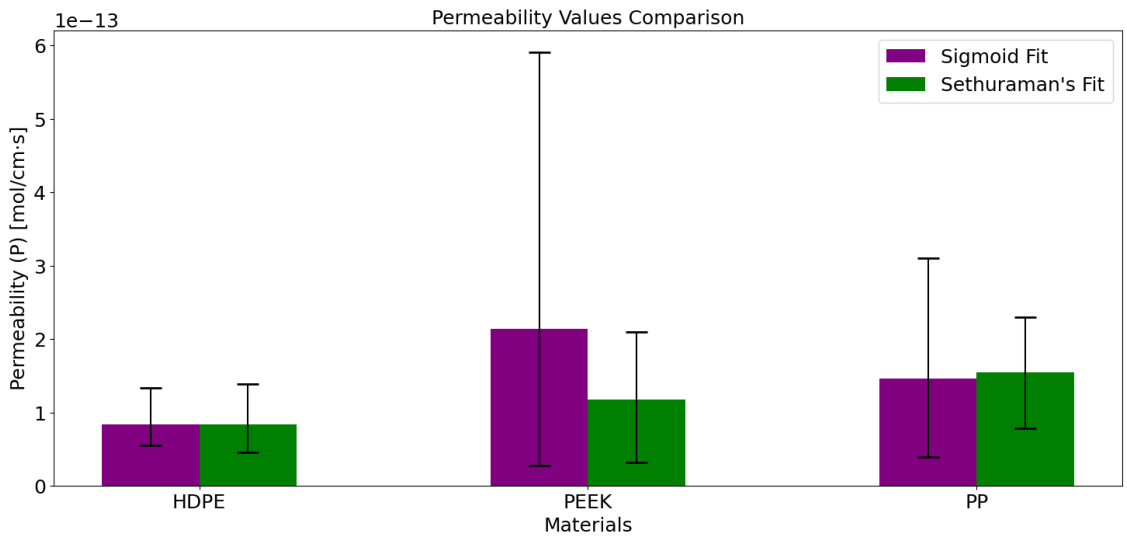

Figure 3.27: Comparison between Permeability values calculated with the two methods for the tested polymer samples

Comparison of Diffusivity and Solubility Values for the Three Methods

The breakthrough time method yields results with significant scatter, especially for polypropylene (PP). This may be because breakthrough time reflects the initial, non-steady state diffusion of gas molecules through the polymer, which is likely to happen through the fastest path for the molecules, Therefore, this diffusivity value may be influenced by the presence small voids or manufacturing defects within the polymer. Additionally, the samples, which were manually ground to achieve the desired thickness, may exhibit non-uniform thickness, causing faster permeation in thinner areas. This explains why the time lag method is more consistent and widely preferred in literature.

The time lag method and Sethuraman's fit generally show better agreement, suggesting that these methods more accurately capture steady-state diffusion. The comparison across methods shows that Sethuraman's solution provides a reliable fit for both diffusivity and permeability, as it aligns well with time lag results.

Comparison of Permeability value results for the two methods

Sethuraman's solution better captures the permeability trends across the polymer samples than the sigmoid fit. Although the permeability values derived from Sethuraman's solution do not match those found in literature—possibly due to the difference in the driving force for diffusion (a concentration gradient in the electrochemical test versus a pressure gradient in high-pressure hydrogen permeation tests)—the expected trend is still observed. Specifically, HDPE shows the lowest permeability, followed by PEEK, with PP exhibiting the highest permeability. In contrast, the permeability values obtained from the sigmoid fit do not consistently reflect this expected trend. A key difference here is that Sethuraman's solution could not be fitted to all the permeation curves, so certain "outlier" curves were excluded from the calculations for Sethuraman's permeability values. The sigmoid fit, however, was applied to all experiments, potentially including samples that exhibit behavior not fully aligned with Sethuraman's model assumptions. The discrepancy between the two methods may thus arise from these outlier cases. This also suggests that Sethuraman's solution's might be effective in filtering out non-representative data and capture a trend that aligns better with the material properties and expected behavior. Overall, all the solubility and diffusivity values calculated with the three methods capture the same trend. These results will be justified below by evaluating the chemical structure and cristallinity of the three polymers, which are reported in appendix A, as well as the T_g which from literature is reportedly - 125 °C for HDPE [26], - 20 °C for PP [36] and was evaluated at 147 °C for PEEK from DSC (appendix A).

Solubility

According to the literature, solubility in polymers is primarily influenced by two factors: crystallinity and glass transition temperature (T_g), rather than the chemical composition of the polymer itself. The most pronounced difference in solubility behavior is observed between glassy and rubbery polymers [67, 85, 84].

In glassy polymers, solubility is often higher due to the dual-sorption model. This model suggests two distinct contributions to gas sorption: (1) Langmuir-type sorption in unrelaxed free volumes, which act as ”traps” for gas molecules, increasing solubility, and (2) Henry’s mode of sorption, representing the uniform dissolution of gas molecules in the polymer matrix. As explained in sections 1.1.1 and 1.1.1. The unrelaxed free volume in glassy polymers creates frozen ”voids” that preferentially capture gas molecules, thus increasing solubility by effectively trapping them within these sites. As a result, glassy polymers like PEEK, with rigid molecular structures below T_g exhibit significantly higher solubility than their rubbery counterparts under standard conditions [67, 85].

Crystallinity also impacts solubility, as crystalline regions in polymers are essentially impermeable to gas molecules. This makes crystallinity inversely proportional to solubility: higher crystallinity reduces the polymer’s capacity to absorb gas, as crystallites act as impermeable barriers. Therefore, polymers with high crystallinity, such as HDPE and PP, exhibit low solubility due to the limited available amorphous regions where gas molecules can dissolve [84].

The results in figure 3.26 align with these theoretical expectations. PEEK shows the highest solubility among the tested polymers, primarily due to its glassy nature, even though it has the lowest crystallinity of the three. In contrast, HDPE and PP, both rubbery and highly crystalline, display solubility values close to zero.

Regarding chemical composition, studies indicate that non-polar gases like hydrogen are more easily absorbed by non-polar polymers. In this case, all three polymers are classified as non-polar. HDPE and PP are the least polar, while PEEK has slightly higher polarity due to the presence of polar oxygen bonds. However, PEEK remains largely non-polar due to its symmetrical structure, and the solubility differences observed seem to be much more influenced by T_g and crystallinity than by polarity distinctions.

Diffusivity

In contrast to solubility, diffusivity is influenced by the nature of the polymer itself. As detailed in section 1.1.2, diffusivity is a thermally activated process governed by the activation energy (E_D), which represents the energy needed for a gas molecule to make a ”jump” from one free volume element to an adjacent one. For this jump to occur, a neighboring free volume element must be available, allowing the gas molecule to move through the polymer matrix. These nanovoids or free volume elements are dynamically created and destroyed within the amorphous regions of the polymer due to thermal fluctuations, which result from the motion of polymer chains [69, 85, 67].

Due to the restricted mobility of molecular chains in glassy polymers, such as PEEK, these polymers are expected to have the lowest diffusivity values. This is consistent with my results, as shown in Figure 3.25, where PEEK exhibits the lowest diffusivity (D) across all three calculation methods. The chemical structure of PEEK—with longer, bulkier chains due to the presence of aromatic groups—contributes to its high T_g relative to HDPE and PP. This structural rigidity significantly limits the mobility of PEEK’s amorphous chains at room temperature, which in turn restricts gas diffusion.

Crystallinity also plays a critical role in determining diffusivity. Similar to solubility, diffusivity (D) is inversely proportional to crystallinity. Crystalline regions within polymers act as impermeable barriers to gas molecules, which cannot penetrate these densely packed areas. Therefore, as crystallinity increases, the available pathways for diffusion decrease, reducing the overall diffusivity. This explains why HDPE has a lower diffusivity than PP, despite both being rubbery at room temperature. HDPE’s higher crystallinity presents more barriers to diffusion, limiting the effective diffusivity compared to the less crystalline PP.

In conclusion, while both crystallinity and T_g play essential roles in defining diffusivity, the transition from glassy to rubbery behavior (dictated by T_g) is the most impactful. Although PEEK is the least crystalline

of the three polymers, it still exhibits the lowest diffusivity because it remains in a glassy state at room temperature, severely limiting molecular chain mobility and thus reducing diffusion rates.

Permeability

Finally, permeability arises from the combined effects of solubility and diffusivity, as shown in Figure 3.27. Among the three polymers, HDPE exhibits the lowest permeability. This result aligns with both the Sethuraman's equation findings and literature values. Although HDPE has a higher diffusivity than PEEK, its overall permeability is much lower due to its extremely low solubility. HDPE's low solubility can be attributed to its rubbery nature, which follows Henry's sorption behavior, and its high crystallinity, which reduces available sites for hydrogen absorption.

PEEK shows a permeability value close to that of HDPE, but for different reasons. PEEK's solubility is relatively high due to its glassy state, which causes the presence of unrelaxed free volumes that trap gas molecules. However, PEEK's diffusivity is significantly lower than HDPE's due to its rigid, glassy molecular structure and high T_g, which restrict molecular chain mobility. This low diffusivity balances out its high solubility, resulting in a permeability comparable to that of HDPE.

As expected, polypropylene (PP) has the highest permeability among the three polymers. PP's molecular structure and general properties are quite similar to those of HDPE, but with one key difference: PP has lower crystallinity, which reduces impermeable regions and increases the availability of diffusion pathways. As a result, PP has the highest diffusivity among the three materials. Its solubility is also intermediate between the low values for HDPE and the higher values for glassy PEEK, further enhancing its permeability relative to HDPE and PEEK.

3.2.5. Exposure to LN_2

In this section, the permeation parameters of the three samples before and after exposure to a cryogenic environment are analyzed. The LN2 cycling procedure was adapted from Flanagan's study [25] and was conducted by immersing the specimens in liquid nitrogen (LN2) for 6 minutes, followed by a 2-minute exposure to room temperature outside the tank. This cycle was repeated a total of 10 times.

The LN2 cycling was applied to the polymer samples to simulate the temperature fluctuations these materials would experience in liquid hydrogen tanks during repeated filling and emptying cycles. Although actual temperature gradients in service are likely to be less severe, this test offers a conservative approach to assess the durability of candidate materials under extreme conditions, helping to determine their suitability for operational use and identify any potential safety risks. Thermal cycling can cause microstructural changes in polymers, which may alter their diffusivity and permeability to hydrogen gas, impacting overall performance and integrity [25] This test also could serve to evaluate the sensitivity of the electrochemical cell setup in detecting subtle changes in diffusion and permeation behavior that might result from cryogenic exposure.

The parameters analyzed include are D_{t_L}, C_{t_L} and the permeability value derived using Sethuraman's solution. As discussed in the previous section, these parameters have proven to be the most reliable for capturing the diffusion characteristics of hydrogen in these samples.

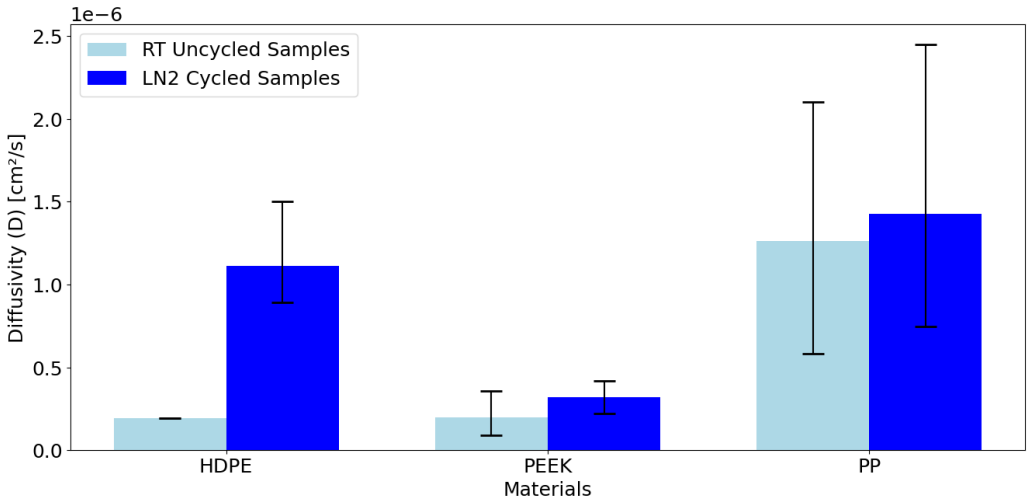

Figure 3.28: Comparison between Diffusivity values for uncycled and cycled specimens calculated with the time lag method.

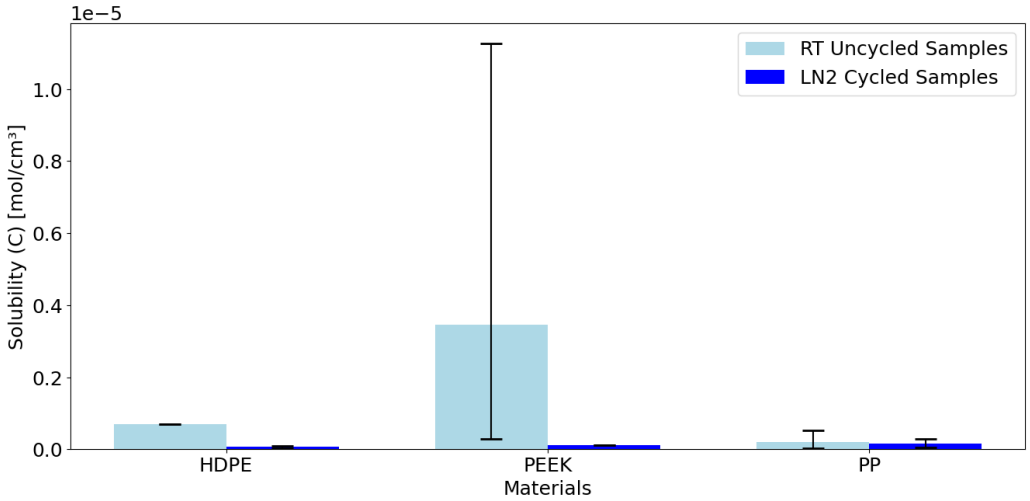

Figure 3.29: Comparison between Solubility values for uncycled and cycled specimens calculated with the time lag method.

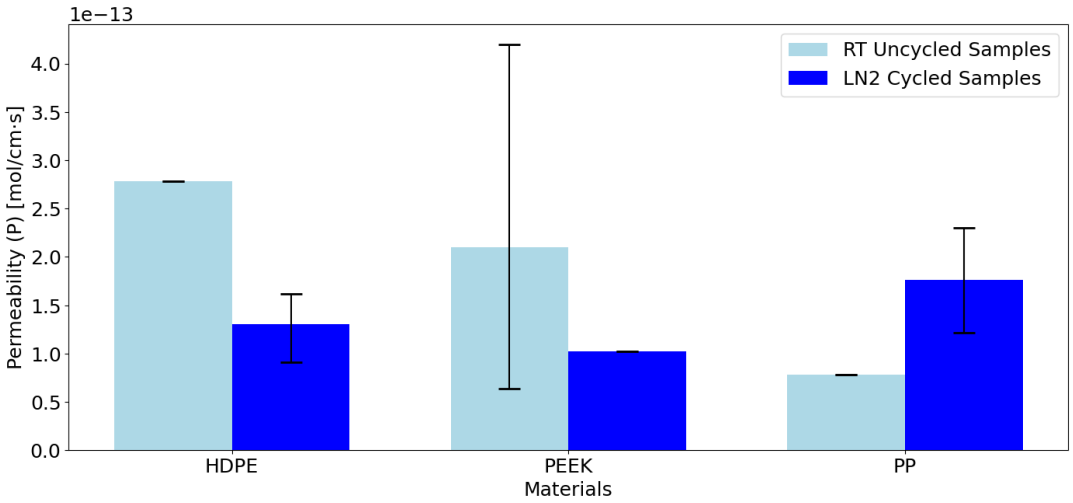

Figure 3.30: Comparison between Permeability values for uncycled and cycled specimens calculated with the Sethuraman's fit.

Overall, as shown in Figures 3.28, 3.29 and 3.30 the measured values for permeability, diffusivity, and solubility remain somewhat unchanged before and after cryogenic cycling. This could indicate that thermal cycling does not significantly impact the polymer samples. These findings align with Flanagan's study [25] on the effects of same thermal cycling on PEEK-CF composites. However, the results display considerable skewness, likely due to the limited number of tests conducted because of time constraints. To reach more definitive conclusions, additional testing of this type is recommended.

4

Conclusions

This thesis project set out to explore whether an electrochemical technique, typically used to study hydrogen permeation in metals, could be adapted for testing on polymer samples. The primary objective was to create a reliable setup for evaluating the diffusion mechanism of hydrogen gas through polymers, with the ultimate goal of relating fundamental physical (glassy or rubbery state), chemical (structure and cristallinity) and thermodynamical (T_g) properties of polymers to their response to hydrogen permeation. The findings from this study, along with future research using this testing method hold the potential to address significant safety and performance challenges for polymer-based materials intended for liquid hydrogen-powered commercial aviation applications.

The project began by examining the conventional Devanathan-Stachurski (DS) setup, identifying the essential components and features required for measuring hydrogen permeation in metals. Through this analysis, key equipment and modifications were identified to render the DS setup suitable for polymers. This adaptation process included selecting appropriate permeation cells, identifying a suitable metallic coating to promote hydrogen evolution, absorption, and oxidation, configuring the two potentiostats accurately, and incorporating a nitrogen purge to establish controlled conditions.

Understanding the electrochemistry involved was essential to establishing optimal parameters for current and potential on both the charging and detection sides. Once configured, the setup was validated and yielded measurements that captured expected material trends. While specific numerical values differed from those reported in the literature, this discrepancy is attributed to the testing conditions, as this setup enforces permeation through a concentration gradient rather than a pressure gradient. Overall, the results confirmed the setup's capacity to reliably measure hydrogen permeation in polymer samples, providing a comparative basis for evaluating their performance and response to hydrogen permeation.

To interpret these measurements, different methods for calculating diffusivity and permeability were examined. Diffusivity values were extrapolated from experimental data curves using either the breakthrough time method or the time lag method. Although the breakthrough time method captures the permeation of the first hydrogen molecules, providing information on the material's initial response to hydrogen exposure, it is highly sensitive to individual sample characteristics and defects. This sensitivity arises because the first gas molecules follow the fastest paths through the polymer, which can vary greatly among samples, resulting in scattered and less comparable results. In contrast, the time lag method evaluates diffusion under steady-state conditions, offering a more comprehensive view of the overall diffusion process and minimizing the impact of sample-specific defects.

Additionally, observation of the permeation curves showed that steady-state conditions are reached quickly due to the small size of hydrogen molecules, which are readily absorbed and rapidly diffuse through all available paths. This rapid transition to steady-state suggests that the time lag method can closely approximate diffusion behavior under operational conditions, as transient conditions are likely to persist for a much shorter duration than steady-state conditions. Therefore, the time lag method

is deemed more suitable for assessing diffusion properties reliably and comparably across different polymer types.

Another approach employed was fitting the equation proposed by Sethuraman [73], which is derived as a solution of Fick's law and the boundary conditions of the setup under ideal conditions. This method yielded highly consistent results for diffusivity and permeability in cases where ideal boundary conditions were respected. However, the equation could not be applied successfully to all data sets, likely because the ideal boundary conditions were not maintained across all experiments. With further refinements to the process of sample preparation, boundary conditions would be more consistently and closely represented, this method could prove to be the most accurate approach for characterizing diffusion properties.

Additionally, based on the same boundary conditions, an alternative equation was identified to estimate permeability from steady-state current values. This steady-state approach was applied across all data sets, including those where Sethuraman's solution could not be fit, offering an approximate permeability value even when ideal conditions were not fully realized.

The diffusivity, solubility, and permeability values for the three polymer samples were compared, yielding plausible results that could be explained by the differing properties of each polymer. Analysis of these results demonstrated that the glass transition temperature (T_g) and crystallinity are the primary polymer properties influencing hydrogen permeation. Specifically, an increase in crystallinity showed an approximately linear inverse relationship with both diffusivity and permeability. However, the most pronounced effect was observed with the transition of polymers between glassy and rubbery states. Glassy polymers exhibited distinct behavior from rubbery polymers; while their solubility tends to be higher and diffusivity lower compared to rubbery polymers, the extent of these differences remains challenging to quantify precisely, complicating the prediction of their overall impact on permeability.

Finally, cryogenic cycling was applied to simulate the temperature variations typical of real-world hydrogen storage conditions. The setup did not capture significant changes in the parameters, in accordance with literature. However, the results were deemed inconclusive due to the low number of tests that were performed.

Overall, the adaptation of the Devanathan-Stachurski (DS) cell for polymers presents a promising, compact alternative for permeation testing. The primary advantages of this setup lie in its simplicity, ease of construction, and faster results, all while avoiding the need for hydrogen gas compared to other methods such as Thermal Desorption Analysis (TDA) and High-Pressure Hydrogen Permeation (HPHP) testing. TDA, for example, requires multiple steps, including the use of an oven and high-pressure hydrogen gas, while HPHP testing demands complex, costly tubing to prevent upstream leakage and maintain a vacuum on the detection side.

With further adjustments and additional studies (detailed in Chapter 5), there is potential to apply the findings at temperatures near standard, to obtain data on the material behavior in cryogenic conditions. This approach would bring the analysis closer to the actual operational environment of liquid hydrogen (LH2) storage tanks.

However, the primary limitation of the DS setup is its inability to assess the effects of varying pressure on diffusion parameters. Despite this limitation, DS testing under standard conditions can serve as a conservative method for pre-screening polymers for hydrogen storage applications, providing quick, comparable results across a range of materials. The best-performing polymers identified through DS testing could then be subjected to more rigorous HPHP testing, including assessments at cryogenic temperatures, to further discern the most suitable candidates for liquid hydrogen storage tank applications.

5

Recommendations for Future Work

This thesis has demonstrated the potential of the Devanathan-Stachurski cell as a method to study hydrogen diffusion in polymer-based materials, yet several refinements and further investigations are recommended.

One significant limitation currently is that, as the Devanathan-Stachurski setup relies on aqueous solutions, it cannot be used for studies at temperatures below the freezing point or above the boiling point of water. Nevertheless, permeability, diffusivity, and solubility of polymers have been widely shown to depend on temperature in accordance with an Arrhenius relationship (Equations 1.14, 1.15, and 1.16), , where the constants are the gas constant R, a value for the activation energy, and a pre-exponential factor for each of the three parameters, respectively. Therefore, experiments across a controlled temperature range (5°C to 40°C) could provide valuable data. The feasibility of such temperature-controlled experiments has already been succesfully demonstrated in a Devanathan-Stachruski setup for pipeline steel samples within a similar temperature range [89]. By conducting experiments to determine diffusivity (D), permeability (P), and solubility (S) over this temperature range for each polymer, the Arrhenius relationship could be fit to the data, yielding the constants that would allow for estimation of these parameters at any temperature. Although the Arrhenius model does not account for phase transitions between rubbery and glassy states—which, as this study has shown, greatly impact permeation behavior—it is generally expected that permeation will slow at extremely low temperatures. This approach would therefore provide an initial basis for predicting permeation rates in cryogenic conditions.

Optimization of the grinding, polishing (potentially experimenting with very fine grits), and cleaning processes for sample surfaces is recommended to enhance coating quality. Given the limited documentation available, consulting with a representative of the manufacturer of the sputtering machine in current use at the laboratory could be highly beneficial for determining optimal parameters for sputtering palladium onto polymer samples. Improving surface quality and, particularly, the adherence of the palladium coating to the polymer substrate would help achieve conditions closer to the ideal boundary conditions required for accurate DS measurements.

Testing on Composite Materials: The DS setup should be extended to study composite materials. Non-conductive composites, such as glass or flax fiber-reinforced polymers, are straightforward to test in the same way polymer samples are currently tested. For conductive composites like CFRPs, minor modifications are required, like earthing the sample and using potentiostats in floating mode to prevent interference, as explained in detail in [6].

This study did not include thermoset polymers, and further research is recommended to explore the effects of cross-linking in thermosets on permeation behavior, especially to observe whether cross-linking exhibits a similar relationship with permeation as crystallinity does in thermoplastics. Additional studies on thermoplastics, particularly those in their glassy phases, are also advised. Literature suggests that the unfrozen free volumes in glassy polymers could act as ”traps” for hydrogen, allowing it to accumulate until these microscopic voids are saturated [85, 69, 24].
At standard temperature and pressure conditions, this mechanism of hydrogen sorption does not pose

significant issues; however, under the operating conditions of hydrogen storage tanks—where temperatures are extremely low—trapped hydrogen could potentially condense into a liquid state, causing polymer swelling and structural degradation. Additionally, operational pressure increases could result in the bursting of these hydrogen pockets, leading to sudden material failure. Understanding the trap density across various glassy polymers would be valuable, as it could provide insight into the material's vulnerability to these effects.

Trap density estimation is already conducted in DS setups for metal materials by analyzing the current signal after charging is halted. All the accumulated hydrogen into the bulk material is then allowed diffuse to the detection side where it is oxidized, until the current returns to baseline. Charging is then restarted and a second transient is developed. These two transients can then be fitted to mathematical models that account for both trap density and the average amount of dissolved hydrogen in the traps [70]. Adapting this approach for polymer analysis should be straightforward, providing an effective means of determining the existence of traps in glassy polymers.

References

[1] B. D. Adams and A. Chen. *The role of palladium in a hydrogen economy*. 2011. DOI: 10.1016/S1369-7021(11)70143-2.

[2] Z. Ahmad. “Chapter 2: Basic Concepts in Corrosion”. In: *Principles of Corrosion Engineering and Corrosion Control*. 2006.

[3] E. Akiyama and S. Li. “Electrochemical hydrogen permeation tests under galvanostatic hydrogen charging conditions conventionally used for hydrogen embrittlement study”. In: *Corrosion Reviews* 34.1-2 (Mar. 2016), pp. 103–112. ISSN: 03346005. DOI: 10.1515/CORREV-2015-0049/MACHINEREADABLECITATION/RIS. URL: https://www.degruyter.com/document/doi/10.1515/corrrev-2015-0049/html.

[4] ASTM. *ASTM -D792 Standard Test Methods for Density and Specific Gravity (Relative Density) of Plastics by Displacement1*. Tech. rep.

[5] ASTM. *G148 Standard Practice for Evaluation of Hydrogen Uptake, Permeation, and Transport in Metals by an Electrochemical Technique*. Tech. rep. 2018. DOI: 10.1520/G0148-97R11. URL: www.astm.org,.

[6] *Autolab PGSTAT100N | Metrohm*. URL: https://www.metrohm.com/en_nl/products/p/gsta/pgstat100n.html.

[7] S. Bagarello, D. Campagna, and I. Benedetti. “A survey on hydrogen tanks for sustainable aviation”. In: *Green Energy and Intelligent Transportation* (Sept. 2024), p. 100224. ISSN: 2773-1537. DOI: 10.1016/J.GEITS.2024.100224.

[8] R. Baker and B. Low. “Gas Separation Membrane Materials – A Perspective”. In: *Macromolecules* 47 (June 2014), pp. 6999–7013. DOI: 10.1021/ma501488s.

[9] E. Barboza et al. “Processing of a LLDPE/HDPE pressure vessel liner by rotomolding”. In: *Materials Research* 17 (Oct. 2014), pp. 236–241. DOI: 10.1590/S1516-14392013005000168.

[10] D. C. Bassett, R. H. Olley, and I. A. Al Raheil. “On crystallization phenomena in PEEK”. In: *Polymer* 29.10 (Oct. 1988), pp. 1745–1754. ISSN: 0032-3861. DOI: 10.1016/0032-3861(88)90386-2.

[11] N. P. Bessonova et al. “Thermal behavior of crystalline and amorphous HDPE phase in the process of necking at creep deformation”. In: *Polymer Testing* 97 (May 2021), p. 107127. ISSN: 0142-9418. DOI: 10.1016/J.POLYMERTESTING.2021.107127.

[12] J. Bockris and M. Devanathan. *The Determination of the Coverage on Nickel and Steel During Electrolytic Hydrogen Evolution*. Tech. rep. Philadelphia: University of Pennsylvania, Feb. 1961.

[13] N. Boes and H. Züchner. “Electrochemical methods for studying diffusion, permeation and solubility of hydrogen in metals”. In: *Journal of the Less Common Metals* 49.C (Sept. 1976), pp. 223–240. ISSN: 0022-5088. DOI: 10.1016/0022-5088(76)90037-0.

[14] R. V. Bucur. “Measurements of diffusion coefficients of hydrogen in palladium by a galvanostatic permeation method”. In: *International Journal of Hydrogen Energy* 10.6 (Jan. 1985), pp. 399–405. ISSN: 0360-3199. DOI: 10.1016/0360-3199(85)90066-7.

[15] R. V. Bucur and V. Mecea. “Permeation of hydrogen through metallized polyethyleneterephtalate membranes measured by the stripping potentiostatic method”. In: *Electrochimica Acta* 31.10 (Oct. 1986), pp. 1343–1346. ISSN: 0013-4686. DOI: 10.1016/0013-4686(86)80159-1.

[16] *CompactStat.h standard*. URL: https://www.ivium.com/product/compactstat-h-standard/.

[17] A. Contreras et al. “Hydrogen as aviation fuel: A comparison with hydrocarbon fuels”. In: *International Journal of Hydrogen Energy* 22.10-11 (Oct. 1997), pp. 1053–1060. ISSN: 0360-3199. DOI: 10.1016/S0360-3199(97)00008-6.

[18] M. J. Danielson. “Use of the Devanathan–Stachurski cell to measure hydrogen permeation in aluminum alloys”. In: *Corrosion Science* 44.4 (Apr. 2002), pp. 829–840. ISSN: 0010-938X. DOI: 10.1016/S0010-938X(01)00103-2.

[19] M. Devanathan and Z. Stachurski. “The adsorption and diffusion of electrolytic hydrogen in palladium”. In: *Proceedings of the Royal Society of London. Series A. Mathematical and Physical Sciences* 270.1340 (Oct. 1962), pp. 90–102. ISSN: 0080-4630. DOI: 10.1098/RSPA.1962.0205. URL: https://royalsocietypublishing.org/doi/10.1098/rspa.1962.0205.

[20] M. Doumeng et al. “A comparative study of the crystallinity of polyetheretherketone by using density, DSC, XRD, and Raman spectroscopy techniques”. In: *Polymer Testing* 93 (Jan. 2021), p. 106878. ISSN: 0142-9418. DOI: 10.1016/J.POLYMERTESTING.2020.106878.

[21] J. L. Duda and J. Zielinski. “FreeVolume Theory, in Diffusion in Polymers”. In: *Free Volume Theory in Diffusion in Polymers* (June 1996).

[22] N. Elgrishi et al. “A Practical Beginner’s Guide to Cyclic Voltammetry”. In: *Journal of Chemical Education* 95.2 (2018). ISSN: 19381328. DOI: 10.1021/acs.jchemed.7b00361.

[23] D. Fan, R. E. White, and N. Gruberger. “Diffusion of a gas through a membrane”. In: *Journal of Applied Electrochemistry* 22.8 (1992). ISSN: 0021891X. DOI: 10.1007/BF01027508.

[24] B. Flaconnèche, J. Martin, and M. H. Klopffer. “Méthodes de mesure des coefficients de transport de gaz dans les polymèrez”. In: *Oil and Gas Science and Technology* 56.3 (2001), pp. 245–259. ISSN: 12944475. DOI: 10.2516/OGST:2001022. URL: https://www.researchgate.net/publication/239385609_Transport_Properties_of_Gases_in_Polymers_Experimental_Methods.

[25] M. Flanagan et al. “Permeability of carbon fibre PEEK composites for cryogenic storage tanks of future space launchers”. In: *Composites Part A: Applied Science and Manufacturing* 101 (Oct. 2017), pp. 173–184. ISSN: 1359-835X. DOI: 10.1016/J.COMPOSITESA.2017.06.013.

[26] O. H. Fred-Ahmadu et al. *Interaction of chemical contaminants with microplastics: Principles and perspectives*. 2020. DOI: 10.1016/j.scitotenv.2019.135978.

[27] H. Fujiwara et al. “High-pressure gaseous hydrogen permeation test method: property of polymeric materials for high-pressure hydrogen devices (1)”. In: *International Journal of Hydrogen Energy* 45.53 (Oct. 2020), pp. 29082–29094. ISSN: 0360-3199. DOI: 10.1016/J.IJHYDENE.2020.07.215.

[28] H. Fujiwara et al. “Hydrogen permeation under high pressure conditions and the destruction of exposed polyethylene-property of polymeric materials for high-pressure hydrogen devices (2)”. In: *International Journal of Hydrogen Energy* 46.21 (Mar. 2021), pp. 11832–11848. ISSN: 0360-3199. DOI: 10.1016/J.IJHYDENE.2020.12.223.

[29] C. Gabrielli et al. “Investigation of hydrogen insertion in palladium using permeation transfer function techniques”. In: *Journal of Electroanalytical Chemistry* 532.1-2 (2002). ISSN: 00220728. DOI: 10.1016/S0022-0728(02)00949-X.

[30] C. Gabrielli et al. “Transfer function analysis of hydrogen permeation through a metallic membrane in a Devanathan cell: Part II: Experimental investigation on iron membrane”. In: *Journal of Electroanalytical Chemistry* 590.1 (May 2006), pp. 15–25. ISSN: 1572-6657. DOI: 10.1016/J.JELECHEM.2006.01.030.

[31] M. Galizia et al. “Predictive calculation of hydrogen and helium solubility in glassy and rubbery polymers”. In: *Journal of Membrane Science* 475 (Feb. 2015), pp. 110–121. ISSN: 0376-7388. DOI: 10.1016/J.MEMSCI.2014.10.009.

[32] K. Ganesh, R. Nagarajan, and J. L. Duda. “Rate of gas transport in glassy polymers: a free volume based predictive model”. In: *Industrial & Engineering Chemistry Research* 31.3 (Mar. 1992), pp. 746–755. ISSN: 0888-5885. DOI: 10.1021/ie00003a016. URL: https://doi.org/10.1021/ie00003a016.

[33] L. Gao and B. E. Conway. “Absorption and adsorption of H in the H2 evolution reaction and the effects of co-adsorbed poisons”. In: *Electrochimica Acta* 39.11-12 (Aug. 1994), pp. 1681–1693. ISSN: 0013-4686. DOI: 10.1016/0013-4686(94)85154-9.

[34] U. Gaur and B. Wunderlich. “Heat capacity and other thermodynamic properties of linear macromolecules. IV. Polypropylene”. In: *Journal of Physical and Chemical Reference Data* 10.4 (Oct. 1981), pp. 1051–1064. ISSN: 0047-2689. DOI: 10.1063/1.555650. URL: https://doi.org/10.1063/1.555650.

[35] N. Gay et al. “Hydrogen diffusion through polymer membranes”. In: *MATEC Web of Conferences* 322 (2020), p. 01044. ISSN: 2261-236X. DOI: 10.1051/MATECCONF/202032201044. URL: https://www.matec-conferences.org/articles/matecconf/abs/2020/18/matecconf_matbud2020_01044/matecconf_matbud2020_01044.html.

[36] R. M. Grigorescu et al. *Waste electrical and electronic equipment: A review on the identification methods for polymeric materials*. 2019. DOI: 10.3390/recycling4030032.

[37] S. Grimnes and Ø. G. Martinsen. “Electrodes”. In: *Bioimpedance and Bioelectricity Basics* (Jan. 2015), pp. 179–254. DOI: 10.1016/B978-0-12-411470-8.00007-6. URL: https://linkinghub.elsevier.com/retrieve/pii/B9780124114708000076.

[38] A. T. Haug and R. E. White. “Oxygen Diffusion Coefficient and Solubility in a New Proton Exchange Membrane”. In: *Journal of The Electrochemical Society* 147.3 (Mar. 2000), p. 980. DOI: 10.1149/1.1393300. URL: https://dx.doi.org/10.1149/1.1393300.

[39] Y. Huang and D. Paul. “Effect of Film Thickness on the Gas-Permeation Characteristics of Glassy Polymer Membranes”. In: *Industrial & Engineering Chemistry Research - IND ENG CHEM RES* 46 (June 2007). DOI: 10.1021/ie0610804.

[40] J. Humpenöder. “Gas permeation of fibre reinforced plastics”. In: *Cryogenics* 38.1 (Jan. 1998), pp. 143–147. ISSN: 0011-2275. DOI: 10.1016/S0011-2275(97)00125-2.

[41] D. J. G. Ives, G. J. Janz, and C. V. King. “Reference Electrodes: Theory and Practice”. In: *Journal of The Electrochemical Society* 108.11 (Nov. 1961), 246Ca. ISSN: 1945-7111. DOI: 10.1149/1.2427957. URL: https://iopscience.iop.org/article/10.1149/1.2427957%20https://iopscience.iop.org/article/10.1149/1.2427957/meta.

[42] D. Jeschke and H. A. Stuart. “Diffusion und Permeation von Gasea in Hochpolymeren in Abhängigkeit vom Kritallisationsgrad und von der Temperatur”. In: *Zeitschrift fur Naturforschung - Section A Journal of Physical Sciences* 16.1 (Jan. 1961), pp. 37–50. ISSN: 18657109. DOI: 10.1515/ZNA-1961-0109/MACHINEREADABLECITATION/RIS. URL: https://www.degruyter.com/document/doi/10.1515/zna-1961-0109/html.

[43] D. P. Jones, D. C. Leach, and D. R. Moore. “Mechanical properties of poly(ether-ether-ketone) for engineering applications”. In: *Polymer* 26.9 (Aug. 1985), pp. 1385–1393. ISSN: 0032-3861. DOI: 10.1016/0032-3861(85)90316-7.

[44] M. Kloppfer and B. Flaconneche. “Transport properties of gases in polymers: Bibliographic review”. In: *Oil & Gas Science and Technology - Revue d’IFP Energies nouvelles* 56.3 (2001), pp. 223–244.

[45] F. J. Lanyi et al. “On the Determination of the Enthalpy of Fusion of α-Crystalline Isotactic Polypropylene Using Differential Scanning Calorimetry, X-Ray Diffraction, and Fourier-Transform Infrared Spectroscopy: An Old Story Revisited”. In: *Advanced Engineering Materials* 22.9 (2020). ISSN: 15272648. DOI: 10.1002/adem.201900796.

[46] R. Latypova et al. “The effect of Pd and Ni coatings on hydrogen permeation experiments of as-quenched martensitic steel”. In: *Corrosion Reviews* 41.5 (Oct. 2023), pp. 537–544. ISSN: 21910316. DOI: 10.1515/CORRREV-2022-0118. URL: https://www.researchgate.net/publication/370779863_The_effect_of_Pd_and_Ni_coatings_on_hydrogen_permeation_experiments_of_as-quenched_martensitic_steel.

[47] Y. Lei et al. “Internal polymeric coating materials for preventing pipeline hydrogen embrittlement and a theoretical model of hydrogen diffusion through coated steel”. In: *International Journal of Hydrogen Energy* 47.73 (Aug. 2022), pp. 31409–31419. ISSN: 0360-3199. DOI: 10.1016/J.IJHYDENE.2022.07.034.

[48] J. X. Li, W. L. Cheung, and D. Jia. “A study on the heat of fusion of β-polypropylene”. In: *Polymer* 40.5 (1999). ISSN: 00323861. DOI: 10.1016/S0032-3861(98)00345-0.

[49] Q. Li et al. “Hydrogen Impact: A Review on Diffusibility, Embrittlement Mechanisms, and Characterization”. In: *Materials* 17.4 (2024). ISSN: 1996-1944. DOI: 10.3390/ma17040965. URL: https://www.mdpi.com/1996-1944/17/4/965.

[50] M. Liu et al. “Mechanism of gas barrier improvement of graphene/polypropylene nanocomposites for new-generation light-weight hydrogen storage”. In: *Composites Science and Technology* 249 (Apr. 2024), p. 110483. ISSN: 0266-3538. DOI: 10.1016/J.COMPSCITECH.2024.110483.

[51] M. I. Luppo and J. Ovejero-Garcia. “THE INFLUENCE OF MICROSTRUCTURE ON THE TRAPPING AND DIFFUSION OF HYDROGEN IN A LOW CARBON STEEL”. In: *Corrosion Science* 32.10 (1991), pp. 1125–1136.

[52] W. C. Luu, H. S. Kuo, and J. K. Wu. “Hydrogen permeation through nickel-plated steels”. In: *Corrosion Science* 39.6 (June 1997), pp. 1051–1059. ISSN: 0010-938X. DOI: 10.1016/S0010-938X(97)00006-1.

[53] H. C. Ma et al. “Influence of iron oxides and calcareous deposits on the hydrogen permeation rate in X65 steel in a simulated groundwater”. In: *International Journal of Hydrogen Energy* 46.9 (Feb. 2021), pp. 6669–6679. ISSN: 0360-3199. DOI: 10.1016/J.IJHYDENE.2020.11.129.

[54] P. Manolatos et al. “Use of Pure Metals to Analyse Hydrogen Electrochemical Permeation in Steels”. In: *Journal de Physique IV Proceedings* 5.C7 (1995), pp. 7–409. DOI: 10.1051/jp4:1995750{\"{i}}.

[55] P. Manolatos, M. Jerome, and J. Galland. “Necessity of a palladium coating to ensure hydrogen oxidation during electrochemical permeation measurements on iron”. In: *Electrochimica Acta* 40.7 (May 1995), pp. 867–871. ISSN: 0013-4686. DOI: 10.1016/0013-4686(94)00343-Y.

[56] L. Mckeen. “Introduction to Permeation of Plastics and Elastomers”. In: Mar. 2012, pp. 1–20. ISBN: 9781437734690. DOI: 10.1016/B978-1-4377-3469-0.10001-3.

[57] Metrohm Autolab. “(Un)Grounded: Grounded an floating measurements and their application in electrochemical research”. URL: https://www.metrohm.com/en_nl/applications/whitepaper/wp-069.html.

[58] N. Mills. “Foamed thermoplastics: microstructure and processing”. In: *Polymer Foams Handbook* (Jan. 2007), pp. 39–67. DOI: 10.1016/B978-075068069-1/50004-0.

[59] L. Monson, S. I. Moon, and C. W. Extrand. “Permeation resistance of poly(ether ether ketone) to hydrogen, nitrogen, and oxygen gases”. In: *Journal of Applied Polymer Science* 127.3 (Feb. 2013), pp. 1637–1642. ISSN: 1097-4628. DOI: 10.1002/APP.37517. URL: https://onlinelibrary.wiley.com/doi/full/10.1002/app.37517%20https://onlinelibrary.wiley.com/doi/abs/10.1002/app.37517%20https://onlinelibrary.wiley.com/doi/10.1002/app.37517.

[60] Y. Naito et al. “The effect of pressure on gas permeation through semicrystalline polymers above the glass transition temperature”. In: *Journal of Polymer Science Part B: Polymer Physics* 29.4 (Mar. 1991), pp. 457–462. ISSN: 1099-0488. DOI: 10.1002/POLB.1991.090290408. URL: https://onlinelibrary.wiley.com/doi/full/10.1002/polb.1991.090290408%20https://onlinelibrary.wiley.com/doi/abs/10.1002/polb.1991.090290408%20https://onlinelibrary.wiley.com/doi/10.1002/polb.1991.090290408.

[61] S. Panero. “ELECTROCHEMICAL THEORY | Kinetics”. In: *Encyclopedia of Electrochemical Power Sources* (Jan. 2009), pp. 14–22. DOI: 10.1016/B978-044452745-5.00034-4.

[62] J. S. Park, E. H. Hwang, and S. J. Kim. “Effect of thin films coated steel membrane on electrochemical hydrogen permeation measurement: Palladium vs. nickel”. In: *International Journal of Electrochemical Science* 18.1 (Jan. 2023), pp. 1–5. ISSN: 1452-3981. DOI: 10.1016/J.IJOES.2023.01.010.

[63] S. J. Park and M. K. Seo. “Solid-Liquid Interface”. In: *Interface Science and Technology* 18 (Jan. 2011), pp. 147–252. ISSN: 1573-4285. DOI: 10.1016/B978-0-12-375049-5.00003-7.

[64] D. R. Paul. “Fundamentals of Transport Phenomena in Polymer Membranes”. In: *Comprehensive Membrane Science and Technology* 1 (June 2010), pp. 75–90. DOI: 10.1016/B978-0-08-093250-7.00043-8.

[65] L. Péter et al. “Electrochemical hydrogen permeation on steel sheets with in situ electrodeposition of a Pd layer at the exit side”. In: *Journal of Applied Electrochemistry* 33.7 (July 2003), pp. 613–617. ISSN: 0021891X. DOI: 10.1023/A:1024990905361/METRICS. URL: https://link.springer.com/article/10.1023/A:1024990905361.

[66] L. Raffaelli. “Thermomechanics of Fibre Reinforced Epoxies for Cryogenic Pressurized Containment”. PhD thesis. Munich: Technische Universität München, 2005, pp. 1–138.

[67] L. M. Robeson et al. “Comparison of transport properties of rubbery and glassy polymers and the relevance to the upper bound relationship”. In: *Journal of Membrane Science* 476 (2015). ISSN: 18733123. DOI: 10.1016/j.memsci.2014.11.058.

[68] H. C. Rogers. “Hydrogen Embrittlement of Metals: Atomic hydrogen from a variety of sources reduces the ductility of many metals”. In: *Science (New York, N.Y.)* 159.3819 (1968), pp. 1057–1064. ISSN: 0036-8075. DOI: 10.1126/SCIENCE.159.3819.1057. URL: https://pubmed.ncbi.nlm.nih.gov/17775040/.

[69] D. Roilo. “Gas transport properties and free volume structure of polymer nanocomposite membranes”. PhD thesis. Trento: University of Trento, 2017.

[70] S. Samanta et al. “An alternative and comprehensive approach to estimate trapped hydrogen in steels using electrochemical permeation tests”. In: *International Journal of Hydrogen Energy* 45.51 (Oct. 2020), pp. 26666–26687. ISSN: 0360-3199. DOI: 10.1016/J.IJHYDENE.2020.07.131.

[71] D. Schultheiß. “Permeation Barrier for Lightweight Liquid Hydrogen Tanks”. PhD thesis. Universität Augsburg, 2007.

[72] R. Sen et al. “Electrocatalytic Water Oxidation: An Overview With an Example of Translation From Lab to Market”. In: *Frontiers in Chemistry* 10 (May 2022), p. 861604. ISSN: 22962646. DOI: 10.3389/FCHEM.2022.861604/BIBTEX.

[73] V. A. Sethuraman et al. “Measuring oxygen, carbon monoxide and hydrogen sulfide diffusion coefficient and solubility in Nafion membranes”. In: *Electrochimica Acta* 54.27 (Nov. 2009), pp. 6850–6860. ISSN: 0013-4686. DOI: 10.1016/J.ELECTACTA.2009.06.068.

[74] J. W. Sheffield, K. B. Martin, and R. Folkson. “Electricity and hydrogen as energy vectors for transportation vehicles”. In: *Alternative Fuels and Advanced Vehicle Technologies for Improved Environmental Performance: Towards Zero Carbon Transportation* (Jan. 2014), pp. 117–137. DOI: 10.1533/9780857097422.1.117.

[75] A. Silverstein, E. W. Hall, and W. I. Ngton. *Liquid hydrogen as a jet fuel for high-altitude aircraft*. Tech. rep. Washington DC: National Advisory Committee for Aeronautics, 1955.

[76] M. Sippel et al. “Final Results of Advanced Cryo-Tanks Research Project CHATT”. In: *Th European Conference for Aeronautics and Space Sciences* (2015).

[77] Z. P. Smith et al. “Hydrogen sorption in polymers for membrane applications”. In: *Polymer* 54.12 (May 2013), pp. 3026–3037. ISSN: 0032-3861. DOI: 10.1016/J.POLYMER.2013.04.006.

[78] E. M. Stuve. “Overpotentials in Electrochemical Cells”. In: *Encyclopedia of Applied Electrochemistry*. Ed. by Kreysa Gerhard. New York, NY: Springer New York, 2014, pp. 1445–1453. ISBN: 978-1-4419-6996-5. DOI: 10.1007/978-1-4419-6996-5{_}330. URL: https://doi.org/10.1007/978-1-4419-6996-5_330.

[79] Y. Su et al. “Review of the hydrogen permeability of the liner material of type iv on-board hydrogen storage tank”. In: *World Electric Vehicle Journal* 12.3 (2021). DOI: 10.3390/wevj12030130.

[80] *Taking to the skies, powered by hydrogen | Air Liquide*. URL: https://www.airliquide.com/stories/hydrogen/taking-skies-powered-hydrogen.

[81] E. Tarani et al. “Calculation of the degree of crystallinity of HDPE/GNPs nanocomposites by using various experimental techniques: a comparative study”. In: *Journal of Materials Science* 58.4 (Jan. 2023), pp. 1621–1639. ISSN: 15734803. DOI: 10.1007/S10853-022-08125-4/FIGURES/10. URL: https://link.springer.com/article/10.1007/s10853-022-08125-4.

[82] L. Tau and S. L. Chan. “Effects of ferrite/pearlite alignment on the hydrogen permeation in a AISI 4130 steel”. In: *Materials Letters* 29.1-3 (Nov. 1996), pp. 143–147. ISSN: 0167-577X. DOI: 10.1016/S0167-577X(96)00140-1.

[83] *The European Green Deal - European Commission*. URL: https://commission.europa.eu/strategy-and-policy/priorities-2019-2024/european-green-deal_en.

[84] G. J. Van Amerongen. “Influence of Structure of Elastomers on Their Permeability to Gases”. In: *Rubber Chemistry and Technology* 24.1 (1951). ISSN: 0035-9475. DOI: 10.5254/1.3543028.

[85] D. Van Krevelen and K. Te Nijenhuis. “Properties Determining Mass Transfer In Polymeric Systems”. In: *Properties of Polymers* (Jan. 2009), pp. 655–702. DOI: 10.1016/B978-0-08-054819-7.00018-2.

[86] L. Vecchi et al. “Modelling of hydrogen permeation experiments in iron alloys: Characterization of the accessible parameters – Part II – The exit side”. In: *Electrochimica Acta* 262 (Feb. 2018), pp. 153–161. ISSN: 0013-4686. DOI: 10.1016/J.ELECTACTA.2017.12.173.

[87] C. N. Velisaris and J. C. Seferis. “Crystallization kinetics of polyetheretherketone (peek) matrices”. In: *Polymer Engineering & Science* 26.22 (Dec. 1986), pp. 1574–1581. ISSN: 1548-2634. DOI: 10.1002/PEN.760262208. URL: https://onlinelibrary.wiley.com/doi/full/10.1002/pen.760262208%20https://onlinelibrary.wiley.com/doi/abs/10.1002/pen.760262208%20https://4spepublications.onlinelibrary.wiley.com/doi/10.1002/pen.760262208.

[88] D. Vijayshankar et al. “Hydrogen Permeation as a Tool for Quantitative Characterization of Oxygen Reduction Kinetics at Buried Metal-Coating Interfaces”. In: *Electrochimica Acta* 189 (Jan. 2016), pp. 111–117. ISSN: 0013-4686. DOI: 10.1016/J.ELECTACTA.2015.12.030.

[89] X. Xing et al. “Study of temperature effect on hydrogen embrittlement in X70 pipeline steel”. In: *Corrosion Science* 230 (Apr. 2024), p. 111939. ISSN: 0010-938X. DOI: 10.1016/J.CORSCI.2024.111939.

[90] O. Yépez and B. R. Scharifker. “Oxidation of formate on hydrogen-loaded palladium”. In: *International Journal of Hydrogen Energy* 27.1 (2002). ISSN: 03603199. DOI: 10.1016/S0360-3199(01)00086-6.

[91] S. Yun and S. Ted Oyama. “Correlations in palladium membranes for hydrogen separation: A review”. In: *Journal of Membrane Science* 375.1-2 (June 2011), pp. 28–45. ISSN: 0376-7388. DOI: 10.1016/J.MEMSCI.2011.03.057.

[92] *ZEROe - Low carbon aviation - Airbus*. URL: https://www.airbus.com/en/innovation/low-carbon-aviation/hydrogen/zeroe.

[93] D. Zhang et al. “Study on Hydrogen Permeation Behavior of Polyethylene Liner Material for Type IV Bottle”. Chinese. In: *New Energy Progress* 10.1 (2022), pp. 15–19. DOI: 10.3969/j.issn.2095-560X.2022.01.003.

[94] T.-Y. Zhang, Y.-P. Zheng, and Q.-Y. Wu. “On the Boundary Conditions of Electrochemical Hydrogen Permeation Through Iron”. In: *Journal of The Electrochemical Society* 146.5 (May 1999), pp. 1741–1750. ISSN: 0013-4651. DOI: 10.1149/1.1391836/XML. URL: https://iopscience.iop.org/article/10.1149/1.1391836%20https://iopscience.iop.org/article/10.1149/1.1391836/meta.

[95] Z. Zhang and Y. P. Handa. “An In Situ Study of Plasticization of Polymers by High-Pressure Gases”. In: *Journal of Polymer Science Part B: Polymer Physics* 36.6 (1998), pp. 931–1094. DOI: 10.1002/(SICI)1099-0488(19980430)36:6. URL: https://onlinelibrary.wiley.com/terms-and-conditions.

[96] G. Zheng, B. N. Popov, and R. E. White. “Hydrogen□Atom Direct□Entry Mechanism into Metal Membranes”. In: *Journal of The Electrochemical Society* 142.1 (Jan. 1995), pp. 154–156. ISSN: 0013-4651. DOI: 10.1149/1.2043855. URL: https://www.researchgate.net/publication/234919056_Hydrogen-Atom_Direct-Entry_Mechanism_into_Metal_Membranes.

A

Material Characterization and Surface Treatment Effects

A.1. Chemical Structure

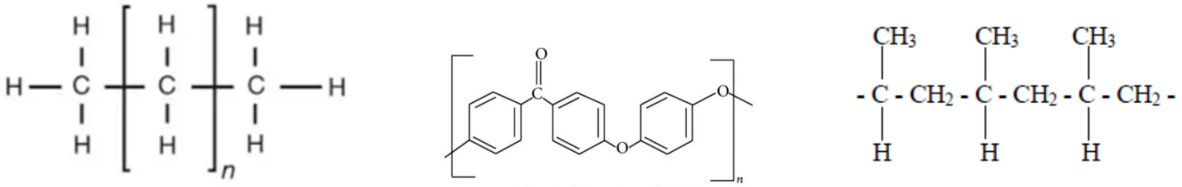

(a) HDPE **(b)** PEEK **(c)** Polypropylene

Figure A.1: Chemical structures of the tested polymer samples

A.2. DSC

The DSC curves for all three polymers are displayed below, and their melting enthalpy is specified as it was utilized to determine the crystallinity. The T_g of PEEK was also evaluated through DSC, while for PP and HDPE this was not possible.

A.2.1. PEEK

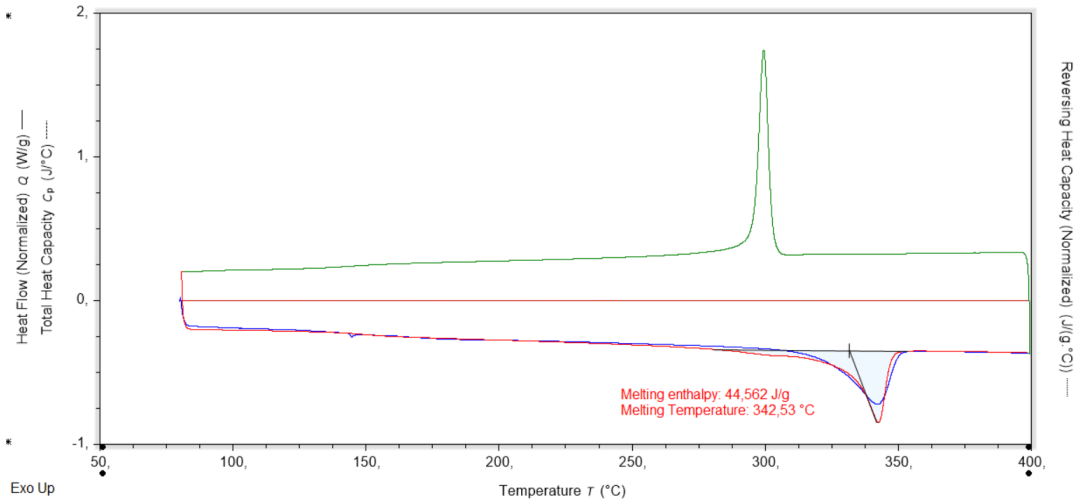

Figure A.2: DSC curve for PEEK and melting enthalpy used for crystallinity evaluation

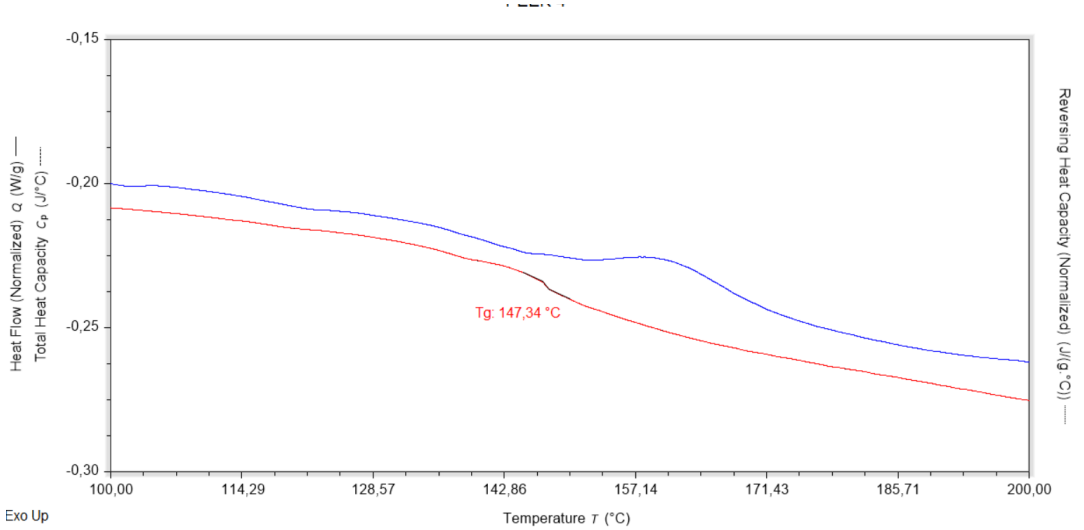

Figure A.3: Evaluation of glass transition temperature for PEEK

A.2.2. HDPE

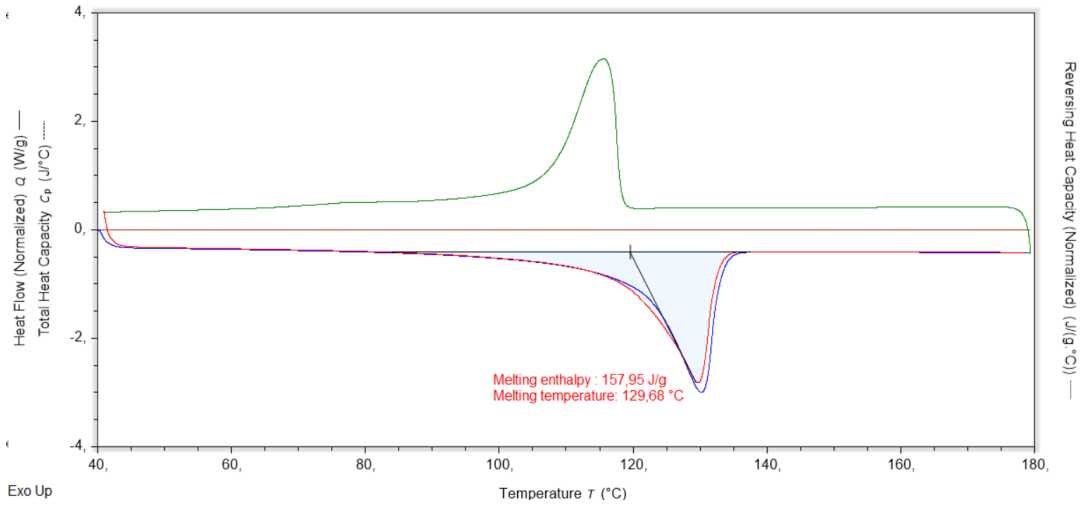

Figure A.4: DSC curve for PEEK and melting enthalpy used for crystallinity evaluation

A.2.3. PP

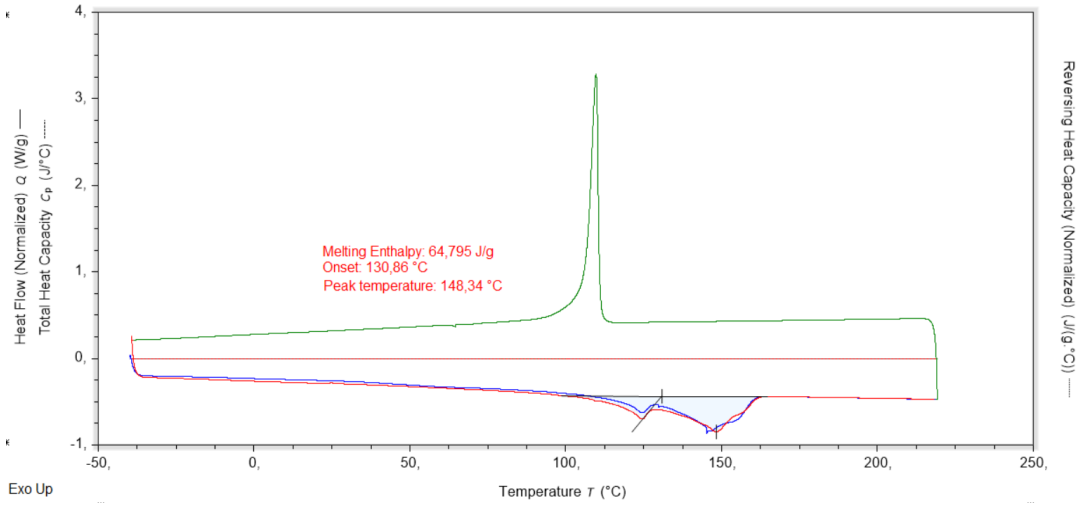

Figure A.5: DSC curve for PP and melting enthalpy used for crystallinity evaluation

A.3. Crystallinity

Cristallinity of the three polymers was evaluated both through the density method and the DSC method, using the equation detailed in section 2.1, and are reported here.

A.3.1. DSC Method

Table A.1 below provides the calculated melting enthalpy, evaluated from DSC, and literature data for the melting enthalpy of the fully crystalline polymer. These parameters were used to determine the crystallinity of each sample.

Table A.1: Crystallinity of polymers evaluated through DSC

Sample	ΔH_f (J/g)	ΔH_f^0 (J/g)	Ref	C (%)
HDPE-1	158	290	[11]	0.52887931
HDPE-2	155.9	290	[11]	0.537586207
HDPE-3(*)	134.2	290	[11]	0.462758621
PEEK-1	44.9	130	[10]	0.343076923
PEEK-2	42.6	130	[10]	0.327692308
PEEK-3	44.6	130	[10]	0.338717949
PP-1	64.7	170	[45]	0.380588235
PP-2	65.8	170	[45]	0.387058824
PP-3	65.6	170	[45]	0.385882353

A.3.2. Density Method

Table A.2 below provides the calculated density, using the water displacement method [4],as well as the literature data for the density of the fully amorphous and fully crystalline polymer. These parameters were used to determine the crystallinity of each sample.

Table A.2: Crystallinity of polymers evaluated through density method

Sample	$\rho_{amorphous}$	Ref	$\rho_{crystal}$	Ref	ρ_{sample}	C
PP-1	0.853	[58]	0.949	[48]	0.913164587	0.65130867
PP-2	0.853	[58]	0.949	[48]	0.912858806	0.64821551
HDPE-1	0.824	[81]	0.985	[81]	0.94733281	0.796501138
HDPE-2	0.824	[81]	0.985	[81]	0.94500058	0.783367826
PEEK-1	1.263	[43]	1.4	[87]	1.29406851	0.245341279
PEEK-2	1.263	[43]	1.4	[87]	1.294434631	0.248162243

A.4. Surface Adhesion - Water Contact Angle Measurements

A.4.1. PEEK

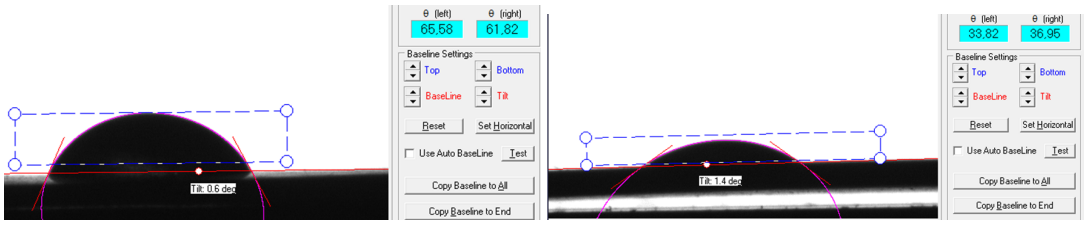

(a) Untreated PEEK **(b)** Treated PEEK

Figure A.6: Water contact angle variation on untreated and corona arc treated PEEK surfaces

A.4.2. HDPE

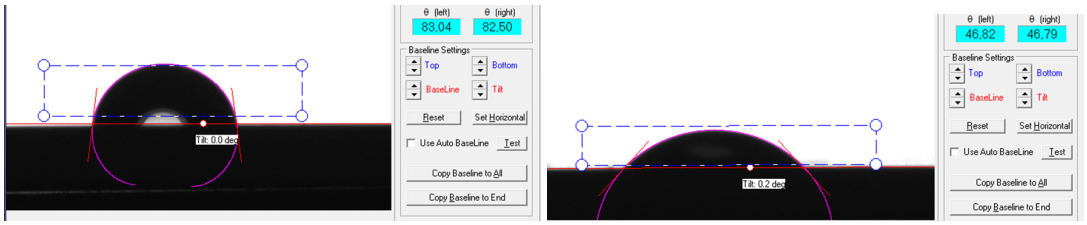

(a) Untreated HDPE **(b)** Treated HDPE

Figure A.7: Water contact angle variation on untreated and corona arc treated HDPE surfaces

B

Literature Surveys

B.1. Permeation Data

Table B.1: Literature values for diffusivities and permeabilities for PEEK, HDPE, and PP

Polymer	Cryst. (%)	D_{t_L} (cm^2/s)	P (mol/(cm s))	Reference
PEEK	15% (DSC)	5.32E-07	1.22E-12	[59]
	30% C #1 (DSC)	2.96E-07	6.14E-13	[59]
	30% C #2 (DSC)	5.16E-07	6.82E-13	[59]
	38% (DSC)	2.42E-07	3.94E-13	[59]
HDPE	92% (density)	3.30E-08	-	[35]
	78% (density)	1.35E-06	9.25E-11	[27]
	80% (density)	-	-	[27]
	58% (DSC)	2.20E-06	6.85E-13	[93]
	54% (DSC)	1.96E-06	7.89E-13	[93]
	57% (DSC)	1.54E-06	6.85E-13	[93]
	61% (DSC)	1.30E-06	5.95E-13	[93]
	-	1.90E-06	8.93E-13	[93]
PP	Amorphous	6.60E-06	1.83E-12	[42]
	Crystalline	3.00E-06	6.25E-13	[42]
	60% (DSC)	3.70E-07	2.86E-12	[60]
	50% (DSC)	-	2.03E-12	[50]

B.2. Detection Side Potential and Electrolyte Choice

Table B.2: Literature survey on the potential and electrolyte choice of different Devanathan Stachurski setup - hydrogen detection side

Specimen Material	Coating Material (Detection Side)	Electrolyte Detection Side	Anodic Oxidation Potential (mV vs SHE)	Reference
Iron	Palladium	0.1 M NaOH	204	[15]
Steel	Palladium	0.1 M NaOH	50	[55]
Iron	Nickel	0.1 M NaOH	108	[70]
Steel	Palladium	0.2 M NaOH	542	[46]
Steel	Palladium/Nickel	0.1 M NaOH	492	[3]
Steel	Palladium	0.1 M NaOH	450	[53]
Steel	Nickel	0.1 M NaOH	492	[96]
Iron	Palladium	0.2 M NaOH	542	[62]
Iron	Palladium	0.1 M NaOH	250-380	[51]
Palladium	-	0.1 M NaOH	-60	[82]
Palladium	-	0.1 M NaOH	204-254	[52]
PET	Palladium	0.05 M H_2SO_4	880-890	[65]
Steel	Palladium/Nickel	0.1 M NaOH	400	[94]

B.3. Charging Side Current and Electrolyte Choice

Table B.3: Literature survey on the current and electrolyte choice of different Devanathan Stachurski setup - hydrogen charging side

Specimen Material	Electrolyte Charging Side	Cathodic Charging Current (mA/cm^2)	Reference
Iron	0.1 M H_2SO_4	- 5	[55]
Steel	0.1 M NaOH + 5 · 10^{-3} M As_2O_3	- 1	[70]
Iron	0.5 M NaCl + 0-3 g/l NH_4SCN	- 0.1	[3]
Steel	Groundwater solution (pH ≈ 6.7 - 7.2)	- 0.9	[53]
Steel	0.6 M NaCl + 3 g/L NH_4SCN	- 1	[62]
Steel	0.1 M NaOH	- 5	[51]
Steel	0.1 M NaOH	- 2	[82]
Steel	0.1 M NaOH + 1 g/l $Na_2S_2 – 9\,H_2O$	- 10	[52]
Iron	0.2 M NaOH	- 2	[95]
Iron	0.1 - 1 M NaOH + $SC(NH_2)_2$ and 0.1 M H2SO4	- 10	[30]
Palladium	0.1 M NaOH	- 0.01	[19]
Palladium	0.1 M NaOH	- 0.05	[54]
Palladium	0.1 M H_2SO_4	0 to -5	[29]

C

Calculations for D and P

The following appendix starts by presenting the demonstrations and calculations for the values of D_{t_b} and D_{t_L} (C.1). These values are evaluated from the permeation transient according to two distinct methods, derived from solutions to Fick's laws and the boundary conditions defined by Devanathan and Bockris [12].

Following this, the calculation of the permeability value from the steady-state current is illustrated (C.1.3). Finally, the solution to Fick's laws and boundary conditions from Sethuraman [73] is presented (C.1.4). This solution results in an equation for the permeation current as a function of the normalized time τ, which was fitted to the experimental data to obtain values for D and P according to Sethuraman's approach.

Before detailing these demonstrations, Fick's second law and the associated boundary conditions for the electrochemical monitoring technique are provided below:

$$\frac{\partial c(x,t)}{\partial t} = D\frac{\partial^2 c(x,t)}{\partial x^2} \tag{C.1}$$

$$c(x,t) = 0 \quad \text{for} \quad 0 \leq x \leq L \quad \text{for} \quad t < 0 \tag{C.2}$$

$$c(x,t) = c \quad \text{for} \quad x = 0 \quad \text{for} \quad t \geq 0 \tag{C.3}$$

$$c(x,t) = 0 \quad \text{for} \quad x = L \quad \text{for} \quad t \geq 0 \tag{C.4}$$

C.1. Calculations for D_{t_b} and D_{t_L}

The extrapolations of the time lag and breakthrough time from the experimental data curves are obtained from a mathematical solution of the boundary conditions and Fick's law for diffusion, proposed by Bockris and Devanathan [12]. All the following reported equations can be found in that document. The equation is:

$$D\left(\frac{dc}{dx}\right)\Big|_t = \frac{D(C_2 - C_1)}{L} + \frac{2D}{L}\sum_{n=1}^{\infty}(C_2\cos n\pi - C_1)\cos\frac{n\pi x}{L}\, e^{-\frac{Dn^2\pi^2 t}{L^2}} \tag{C.5}$$

where:

- $D\left(\frac{dc}{dx}\right)\Big|_t = P_{xt}$ is the permeation rate at point x along the thickness of the sample at time t, according to Fick's first law (eq. 1.3
- C_1 is the hydrogen concentration at x=0 for t $\geq$ 0
- C_2 is the hydrogen concentration at x = L for t $\geq$ 0

C.1.1. Time Lag

The time lag is obtained by evaluating the amount of permeated hydrogen in steady state conditions. The total amount of permeated hydrogen at the charging side (Q_t)is the area under the permeation transient curve, therefore:

$$Q_t = \int_0^t P(x=0)\,dt \tag{C.6}$$

integration of equation C.5 yields:

$$Q_t = \frac{D(C_2 - C_1)t}{L} - \frac{2L}{\pi^2}\sum_{n=1}^{\infty}\frac{(C_2\cos n\pi - C_1)}{n^2}\left(1 - e^{-\frac{Dn^2\pi^2 t}{L^2}}\right) \tag{C.7}$$

in steady-state conditions, $t - - > \infty$ and by summating the second term, equation C.7 reduces to:

$$Q_t = \frac{D}{L}(C_2 - C_1)t\left[1 - \frac{L^2}{6D}\frac{(C_2 + 2C_1)}{(C_2 - C_1)}\right] \tag{C.8}$$

thus the intercept T_{lag} on the time axis of a Q_t vs t plot is given by:

$$T_{lag} = \frac{L^2}{6D}\frac{(C_2 + 2C_1)}{(C_2 - C_1)} \tag{C.9}$$

if $C_2 \gg C_1$ the final value of T_lag is obtained:

$$T_{lag} = \frac{L^2}{6D} \tag{C.10}$$

C.1.2. Breakthrough Time

From equation C.5 it is possible to obtain the normalized permeation rate at the charging side:

$$(\frac{P_t - P_\infty}{P_\infty})_{x=0} = \frac{2}{c_2 - c_1}\sum_{n=1}^{\infty}(c_2\cos n\pi - c_1)e^{-\frac{Dn^2\pi^2 t}{L^2}} \tag{C.11}$$

which, for $C_2 \gg C_1$ equals to:

$$(\frac{P_t - P_\infty}{P_\infty})_{x=0} = -2\sum_{n=1}^{\infty}(-1)^n e^{-\frac{Dn^2\pi^2 t}{L^2}} \tag{C.12}$$

substituting $\frac{1}{t_0}$ for $\frac{D\pi^2}{L^2}$, and expanding the series, it is possible to write:

$$\frac{P_t - P_\infty}{(P_\infty)_{x=0}} = 2\left[1 - e^{-\frac{3t}{t_0}} + e^{-\frac{8t}{t_0}} - \cdots\right]e^{-\frac{t}{t_0}} \tag{C.13}$$

as t increases, the term within the brackets rapidly goes to 1. The resulting equation for the permeation transient is a first order exponential. The authors argue that for a curve of this type the time constant corresponds to a permeation rate of .6299 the steady state value. Also, they claim that for a phenomenon descried by a first order exponential, the steady-state is achieved at a time equal the sum between the time at which the permeation rate begins to rise from zero (breakthrough time) and the time constant of the exponential equation. Therefore:

$$T_{lag} = t_b + t_0 \tag{C.14}$$

substituting the previously found values for T_{lag} and t_0:

$$t_1 = \frac{L^2}{D}\left(\frac{1}{6} - \frac{1}{\pi^2}\right) = \frac{L^2}{D \cdot 15.3} \tag{C.15}$$

C.1.3. Permeability

Permeability is defined as the flux of hydrogen under steady-state transport conditions normalized by both the thickness of the sample and the potential difference driving the diffusion process (see equation 1.8 in section1.1.3). In this setup, this potential difference corresponds to the concentration gradient between the charging and detection sides. In the Devanathan-Stachurski setup, the current (or electron flow) is directly proportional to the amount of oxidized hydrogen, in accordance with Faraday's first law of electrolysis [37]:

$$n_{molesH} = \frac{Q}{nF} \tag{C.16}$$

where:

- n_{molesH} is the number of moles of oxidized hydrogen atoms
- Q is the total charge passed (Q = i·t)
- F is the Faraday constant
- n is the number of electrons involved in the oxidation process

At the working electrode surface on the detection side, hydrogen oxidation follows the reaction shown in equation 3.8. Since each oxidized hydrogen atom releases one electron, then $n = 1$ in Farady's equation.

By definition, the flux of hydrogen atoms is the number of moles of hydrogen atoms flowing through the area of analysis A:

$$J_H = \frac{n_{molesH}}{A \cdot t} \tag{C.17}$$

Combining equations C.16 and C.17, the flux of hydrogen atoms can be expressed as a function of the oxidation current i:

$$J_H = \frac{i}{nFA} \tag{C.18}$$

In the Devanathan-Stachurski setup, hydrogen initially diffuses through the polymer sample in the form of H_2 molecules. When these molecules reach the Pd-polymer interface, they dissociate into hydrogen atoms before being oxidized. Therefore, after the oxidation process, each H_2 molecule produces two electrons, which are detected as the signal. Consequently, the flux of H_2 molecules under steady-state conditions is:

$$J_{H_2}^{stc} = \frac{J_H^{stc}}{2} = \frac{i_\infty}{2FA} \tag{C.19}$$

combining this equation C.19 with 1.8:

$$P = \frac{i_\infty L}{2FA} \tag{C.20}$$

C.1.4. Sethuraman's Equation for i(t)

The equation proposed by Sethuraman [73] is a combination between equation C.20 and the solution of Fan to Fick's second law and the boundary conditions for the Devanathan Stachurski experiment [23]. Fan solved the system of equations using the Laplace transform technique, yielding the following result:

$$\frac{i(t)}{i_\infty} = \frac{2}{\sqrt{\pi t}} \sum_{n=0}^{\infty} \exp\left[-\frac{(2n+1)^2}{4\tau}\right] \tag{C.21}$$

where:
$\tau = \frac{tD}{L^2}$
substituting C.20 into $i\infty$ and remembering that P =S·D:

$$i(t) = \frac{2FADS}{L}\left(\frac{2}{\sqrt{\pi t}} \sum_{j=0}^{\infty} \exp\left[-\frac{(2j+1)^2}{4\tau}\right]\right) \tag{C.22}$$

where:

- A is the area of exposure to the electrolyte
- D is the diffusion coefficient
- F is the Faraday constant
- S is the solubility coefficient
- L is the sample thicnkess

D

Experimental Data

D.1. PEEK

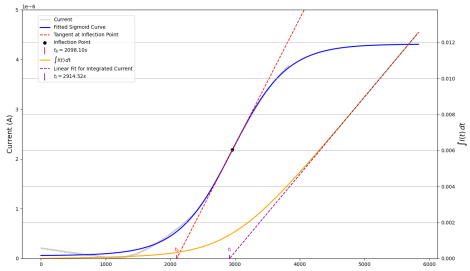

Figure D.1: Sigmoid fit, D_{t_b} and D_{t_L} for PEEK test 1

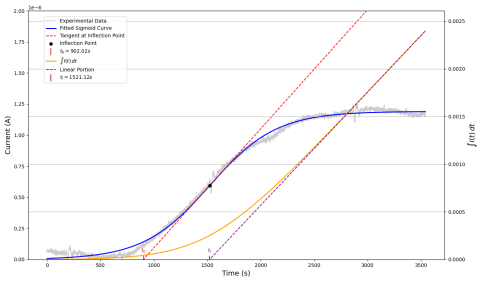

(a) Sigmoid fit, D_{t_b} and D_{t_L}

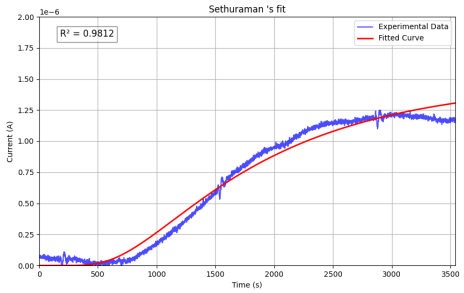

(b) Sethuraman's fit

Figure D.2: PEEK test 2

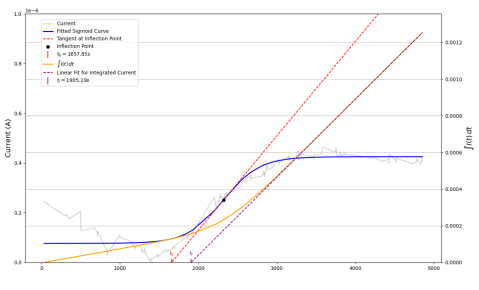

(a) Sigmoid fit, D_{t_b} and D_{t_L}

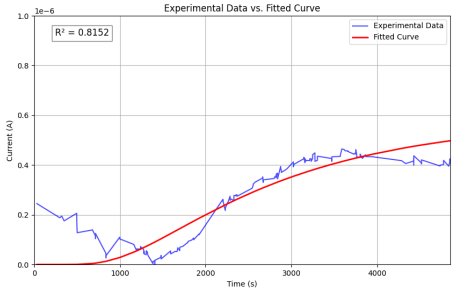

(b) Sethuraman's fit

Figure D.3: PEEK test 3

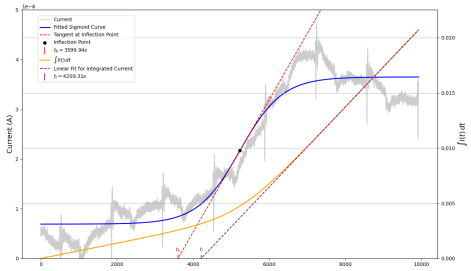

Figure D.4: Sigmoid fit, D_{t_b} and D_{t_L} for test PEEK 4

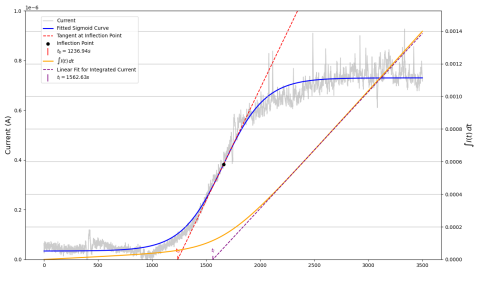

(a) Sigmoid fit, D_{t_b} and D_{t_L}

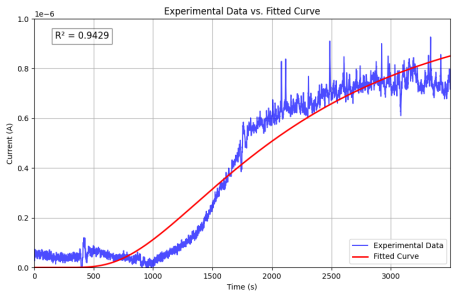

(b) Sethuraman's fit

Figure D.5: PEEK test 5

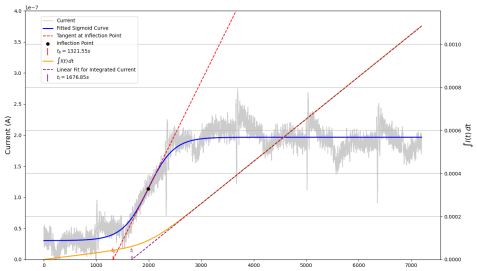

Figure D.6: Sigmoid fit, D_{t_b} and D_{t_L} for PEEK test 6/1

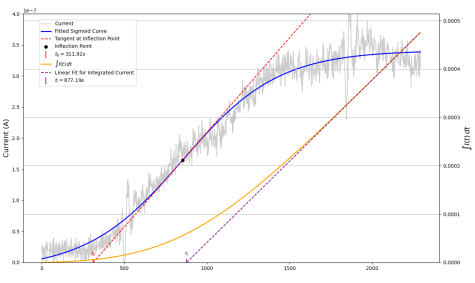

(a) Sigmoid fit, D_{t_b} and D_{t_L}

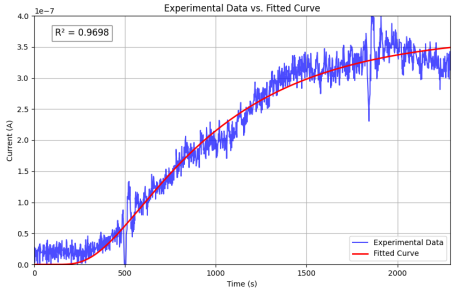

(b) Sethuraman's fit

Figure D.7: PEEK test 6/2

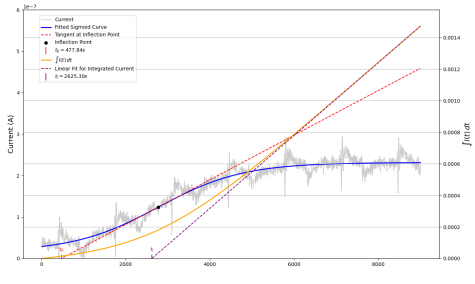

(a) Sigmoid fit, D_{t_b} and D_{t_L}

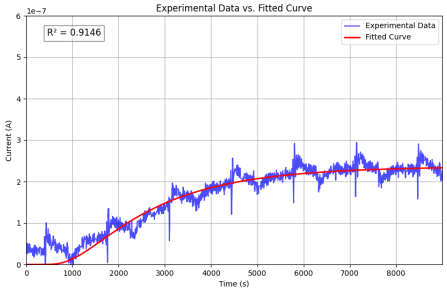

(b) Sethuraman's fit

Figure D.8: PEEK test 7

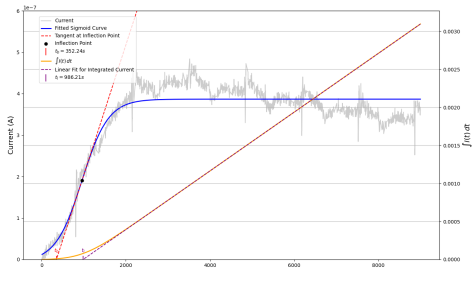

(a) Sigmoid fit, D_{t_b} and D_{t_L}

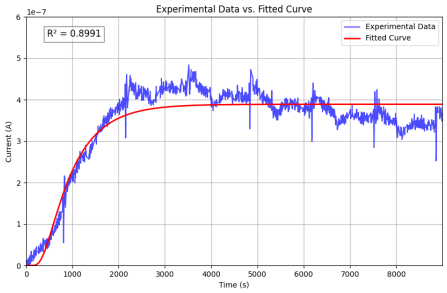

(b) Sethuraman's fit

Figure D.9: PEEK test 7

D.2. HDPE

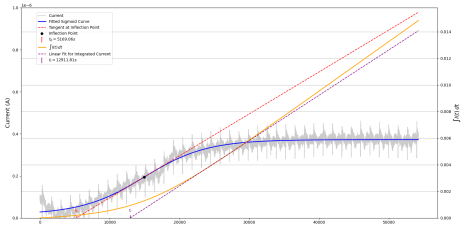

(a) Sigmoid fit, D_{t_b} and D_{t_L}

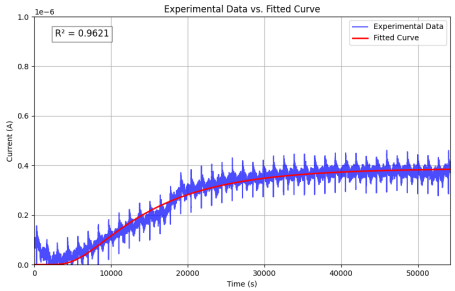

(b) Sethuraman's fit

Figure D.10: HDPE test 1

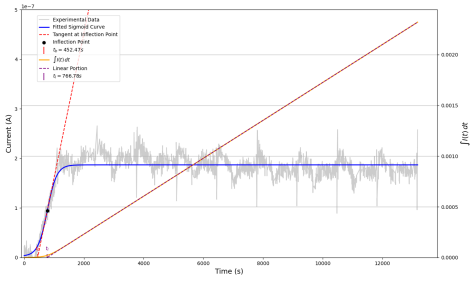

(a) Sigmoid fit, D_{t_b} and D_{t_L}

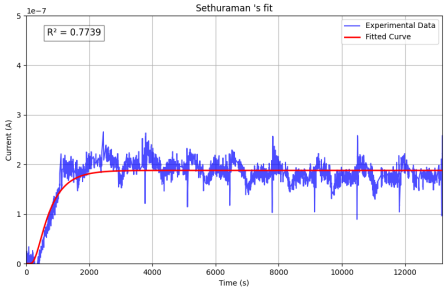

(b) Sethuraman's fit

Figure D.11: HDPE test 2/1

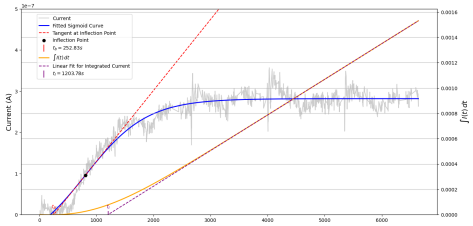

(a) Sigmoid fit, D_{t_b} and D_{t_L}

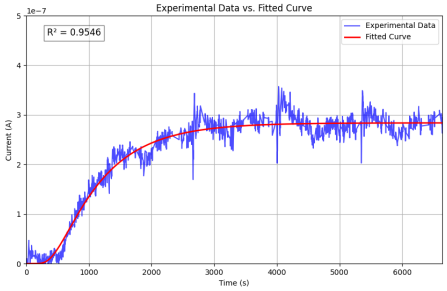

(b) Sethuraman's fit

Figure D.12: HDPE test 2/2

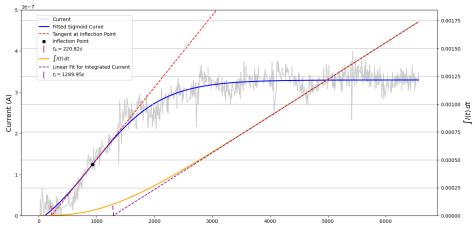

(a) Sigmoid fit, D_{t_b} and D_{t_L}

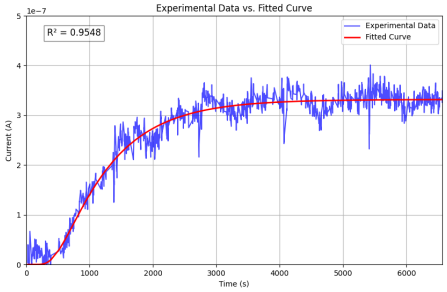

(b) Sethuraman's fit

Figure D.13: HDPE test 2/3

D.3. PP

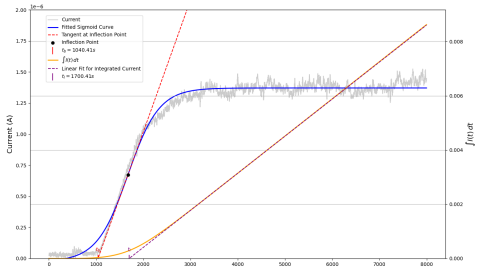

Figure D.14: Sigmoid fit, D_{t_b} and D_{t_L} for PP test 1

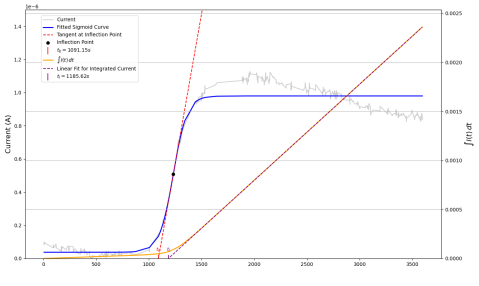

(a) Sigmoid fit, D_{t_b} and D_{t_L}

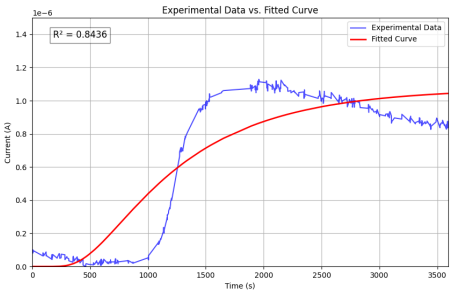

(b) Sethuraman's fit

Figure D.15: PP test 2/1

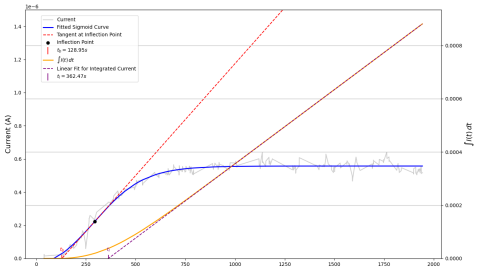

(a) Sigmoid fit, D_{t_b} and D_{t_L}

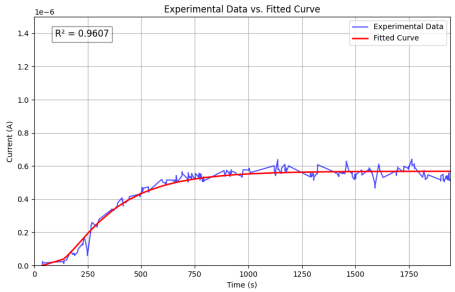

(b) Sethuraman's fit

Figure D.16: PP test 2/2

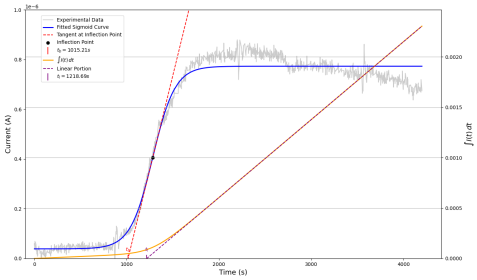

(a) Sigmoid fit, D_{t_b} and D_{t_L}

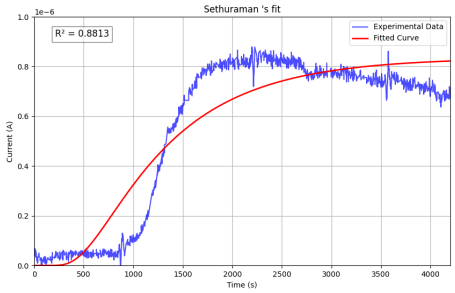

(b) Sethuraman's fit

Figure D.17: PP test 3/1

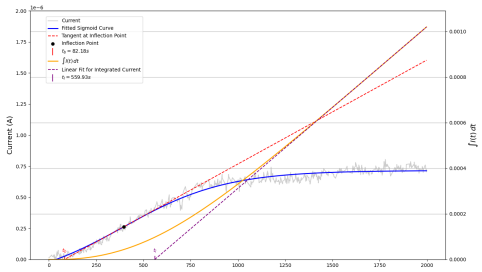

Figure D.18: Sigmoid fit, D_{t_b} and D_{t_L} for PP test 3/2

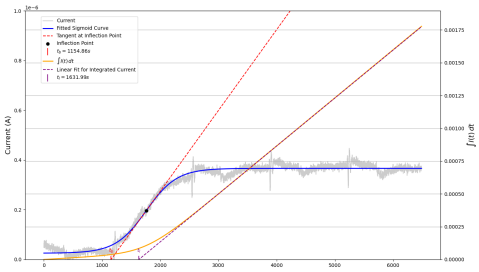

Figure D.19: Sigmoid fit, D_{t_b} and D_{t_L} for PP test 4/1

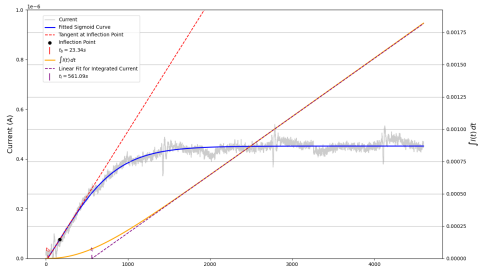

Figure D.20: Sigmoid fit, D_{t_b} and D_{t_L} for PP test 4/2

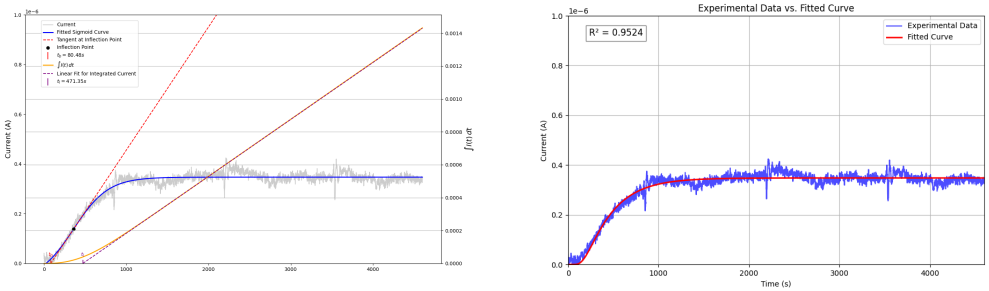

(a) Sigmoid fit, D_{t_b} and D_{t_L}

(b) Sethuraman's fit

Figure D.21: PP test 4/3

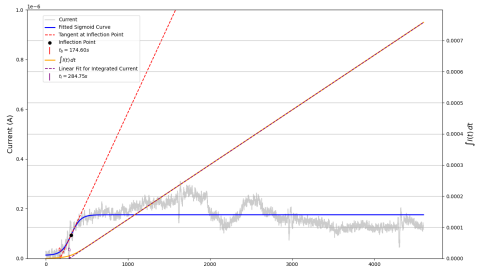

Figure D.22: Sigmoid fit, D_{t_b} and D_{t_L} for PP test 4/4